# DEVELOPING A CERAMIC COMPOSITE FOR APPLICATIONS IN POWER ELECTRONIC SUBSTRATES

BY

**LEMBOYE KAREEM TAIWO**

A Thesis Presented to the
DEANSHIP OF GRADUATE STUDIES

**KING FAHD UNIVERSITY OF PETROLEUM & MINERALS**

DHAHRAN, SAUDI ARABIA

In Partial Fulfillment of the
Requirements for the Degree of

# MASTER OF SCIENCE

**In**

**MECHANICAL ENGINEERING**

**APRIL 2016**

KING FAHD UNIVERSITY OF PETROLEUM & MINERALS

DHAHRAN- 31261, SAUDI ARABIA

**DEANSHIP OF GRADUATE STUDIES**

This thesis, written by LEMBOYE KAREEM TAIWO under the direction his thesis advisor and approved by his thesis committee, has been presented and accepted by the Dean of Graduate Studies, in partial fulfillment of the requirements for the degree of **MASTER OF SCIENCE IN MECHANICAL ENGINEERING.**

Dr. Sohail S. Akhtar
(Advisor)

Dr. Zuhair M. Gasem
Department Chairman

Dr. Abul Fazal M. Arif
(Member)

Dr. Salam A. Zummo
Dean of Graduate Studies

Dr. Tahar Laoui
(Member)

26/5/16
Date

This MSc Thesis work is dedicated to Almighty Allah, the Lord of the worlds

# ACKNOWLEDGMENTS

My sincere gratitude goes to Almighty Allah, the Lord of the worlds, the most gracious, the most merciful, for giving me the opportunity and strength to start and complete my master's program here in KFUPM in good sound metal health. I know the road hasn't been that smooth but still Alhamdulillah.

My deepest gratitude goes to my family, the LEMBOYE family at large, especially my parents; Mr. and Mrs. S.A. Lemboye, my brothers; Idris, Akorede, Abidemi, and Kehinde (my twin brother), and the special one Omobola, for believing so much in me over the years, your persistent prayers, support, love and care for me always do and still keep me on the move, I love you all.

Acknowledgements are due to the Kingdom of Saudi Arabia for granting me this wonderful opportunity to study outside my home country Nigeria. Also are also due the Department of Mechanical Engineering, King Fahd University of Petroleum and Minerals for providing the enabling environment for us to boast our academic career.

Acknowledgements are due to my thesis advisor Dr. Sohail S. Akhtar; he has been so supportive, cooperative and understanding towards my research goals and even with my personal life. To Dr. Abul Fazal M. Arif, who has always been like a father to us all within our research group right from my day 1 in the department, his patience and encouragement has always been my driving force, and I glad I met because he taught me so much. And also of Dr. Tahar Laoui and Dr. Abbas Hakeem who taught me so much, their support and assistance with my experimental works while trying to make it better was worthwhile.

Also, acknowledgements are due to my research group (Applied Computational Mechanics) members; Dr. Khaled, Abba, Usama, Abdul-Majeed, Abdullah and Ibrahim, your support directly or indirectly is so much appreciated. To Mr. Idris and Mr. Lateef, your support with my experimental works was so much worthwhile. And to my friends in Nigeria and Saudi Arabia, and the Nigerian community in KFUPM (NCUPM), your advice, concerns and supports has been so helpful.

I know I can not mention everybody's name in here, and I know words alone cannot express my gratitude and thankfulness to everybody at large, but I do pray Almighty Allah grant us all paradise and reward us all abundantly in all our endeavors.

Thank you all.

# TABLE OF CONTENTS

# LIST OF TABLES

# LIST OF FIGURES

# LIST OF ABBREVIATIONS

| | | |
|---|---|---|
| **AIN** | : | Aluminum Nitride |
| **$Al_2O_3$** | : | Aluminum Oxide/ Alumina |
| **AMB** | : | Active Metal Brazed |
| **CNT** | : | Carbon Nano Tube |
| **CTE** | : | Coefficient of Thermal Expansion |
| **Cu-$Al_2O$** | : | Copper Aluminum Oxide |
| **$Cu_2O$** | : | Cuprous Oxide |
| **Cu-O** | : | Copper Oxide |
| **DBA** | : | Direct Bonded Aluminum |
| **DBC** | : | Direct Bonded Copper |
| **DBS** | : | Direct Bonded Silver |
| **DCB** | : | Direct Copper Bonded |
| **ELCF** | : | Extremely Low Cycle Fatigue |
| **Fe** | : | Iron |
| **FE** | : | Finite Element |
| **FEA** | : | Finite Element Analysis |
| **FEM** | : | Finite Element Method |

| | | |
|---|---|---|
| **IGBT** | : | Insulated Gate Bipolar Transistor |
| **IMS** | : | Insulated Metal Substrate |
| **LCF** | : | Low Cycle Fatigue |
| **NSTIP** | : | National Science, Technology and Innovation Plan |
| **OFHC** | : | Oxygen Free High Thermal Conductivity |
| **SiC** | : | Silicon Carbide |
| **SPS** | : | Spark Plasma Sintering |
| **ZTA** | : | Zirconia Toughened Alumina |

# ABSTRACT

Full Name : Lemboye Kareem Taiwo

Thesis Title : Developing a Ceramic Composite for Applications In Power Electronic Substrates

Major Field : Mechanical Engineering

Date of Degree : April, 2016

The performance of components in power electronics depends on the effective dissipation of the heat generated within them to the environment in a short period of time. In this present work a new ceramic material to replace alumina in power electronic substrate is to be designed, developed and tested. The new ceramic material must possess higher thermal conductivity and lower coefficient of thermal expansion values to alumina, but should retain the environmental and economic benefits of alumina. In order to achieve these, the material was designed to be an alumina composite with either of silicon carbide, chromium or diamond as fillers. Analytical models for predicting composite's effective properties were used to select the appropriate filler volume fraction and particle sizes (chapter 3). With a volume fraction of 20%SiC and particle size of 31µm, spark plasma sintering (SPS) was used for consolidating the composite. The newly developed composite exhibited higher thermal conductivity (from 33 to 38W/$m^2$ K) and lower CTE (from 5.6 to 4.7µm/m-°C) values as compared to pure alumina (chapter 4). Furthermore, the performance of this newly developed material on the thermal-structural and fatigue life of the direct bonded copper (DBC) substrate revealed that, the newly proposed ceramic (alumina composite) has better thermal-mechanical performance and enhanced fatigue life (about 100% higher) as compared to an alumina DBC substrate (chapter 5).

# ملخص الرسالة

**الاسم الكامل**: ليمبوي كريم تايو

**عنوان الرسالة:** تطوير مواد مركبة من السيراميك لقواعد الأجهزة الالكترونية

**التخصص:** الهندسة الميكانيكية

**تاريخ الدرجة العلمية**: أبريل 2016 م

معظم مكونات الاجهزة الالكترونية تولد الكثير من الحرارة التي يجب تُبدّد عبر القواعد الإلكترونية بشكل فعال للبيئة المحيطة في غضون فترة قصيرة من الزمن. العمل الحالي معني بتصميم، تصنيع، و إختبار مادة جديدة مركبة من السيراميك لتحل محل قواعد الألومينا في الأجهزة الإلكترونية. يجب أن تمتلك هذه المادة الجديدة موصلية حرارية عالية و معامل تمدد حراري منخفض مقارنة بمادة الألومينا, كما يجب ان تحافظ هذه المادة الجديدة على الفوائد البيئية والاقتصادية للألومينا. للتحصل علي ذلك، تم تصميم المادة علي ان تكون مركب يحتوي علي الألومينا نفسها مع إضافة أي من كربيد السيليكون ، الكروم أوالماس. تم إستخدام نماذج تحليلية للتنبوء بالخواص الفعالة للمواد المركبة لتحديد الحجم الجزئي المناسب للمواد المضافة و أيضا لتحديد أحجام الجسيمات التي يتكون منها المضاف (الفصل 3). بإضافة 20٪ حجم جزئي من جسيمات كربيد السيليكون ذات حجم 31 ميكرون، تم إستخدام عملية التلبيد عن طريق البلازما لتلبيد المركب الجديد. أظهر هذا المركب المكون من الألومينا وكربيد السيليكون موصلية حرارية أعلى (من 33 إلى 38 واط\متر مربع لكل درجه حرارة مئوية) و معامل تمدد حراري أقل (من 5.58 إلى 4.7 مايكروميتر\متر لكل درجه حرارة مئوية) مقارنة مع الألومينا النقي (الفصل 4). أيضا، أظهر أداء هذا المركب الجديد من السيراميك على العمر التشغيلي لقاعدة النحاس الإلكترونية مباشرة الالتصاق (DBC) عندما تكون معرضة لإحمال دورية حرارية-هيكلية، أنه يمتلك قوة تحمل أعلي للأحمال الحرارية-الميكانيكية، كما أن العمر التشغيلي للقاعدة الإلكترونية عندما تكون معرضة لأحمال دورية يتحسن مع استخدام المركب الجديد (100٪) مقارنة مع مع مركب الألومينا النقي (الفصل 5).

# CHAPTER 1

# INTRODUCTION

## 1.1 Power Electronic Substrate

Power electronic substrates are used in providing interconnection pathway for power electric circuits. They are commonly found in power electronic modules where they provide electrical and thermal contacts for power components and semiconductors mounted upon them. They also provide electrical insulation where needed within the power module. A brief schematic of the substrate is shown in figure 1.1 below.

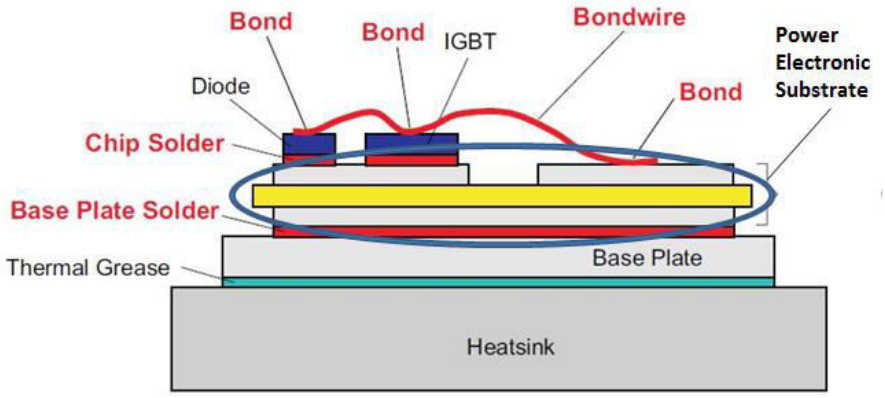


**Figure 1.1** Structural details of a power electronic module [1]

Power electronic modules (as shown in figure 1.2) are commonly found in inverters, solar panels, electric vehicles, automotive systems, power plants and other power industrial machines. They provide physical containment for several power components and semiconductors (as shown in figure 1.3), these components and semiconductors may carry voltage and currents up to 1200V and 75A respectively [2].

**Figure 1.2** High-Power 1/3 phase power module [3]

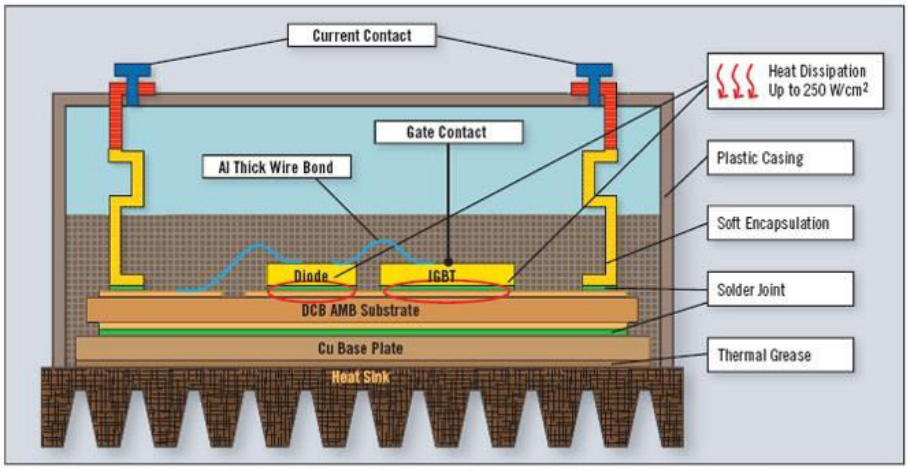


**Figure 1.3** General design of a power module with silicon soldered to a ceramic substrate [5]

## 1.2 Types of Power Electronic Substrates

These power electronic substrates are usually of different types, and include;

- **Direct bonded copper substrate (DBC) or direct copper bonded (DCB):** This substrate type is composed of a ceramic tile bonded and embedded between two copper sheets (as shown in figure 1.4 and 1.5). This substrate is most suited for mounting large power semiconductors [4].
- **Direct bonded aluminum substrate (DBA):** It's similar to the DBC, just that the ceramic tile is embedded between aluminum sheets and not copper sheets. It has a better temperature capability than DBC substrates [4].
- **Direct bonded silver substrate (DBS):** It's still similar in design to the DBC, but instead of copper sheets it uses silver sheets. Also its preferred ceramic is alumina which is embedded between the two silver foils or sheets. Its main advantage over DBC is its simplicity to manufacture at a lower temperature than DBC [6].
- **Active metal brazed substrate (AMB):** In its design, thick metal layers are attached to ceramic plates. The AMB is electrically similar to similar to DBC but it's only suited for small production lots.
- **Insulated metal substrate (IMS):** It consists of a metal baseplate which is usually aluminum covered by thin layer of an epoxy dielectric material and a layer of copper (as shown in figure 1.6). When compared to classical printed circuit boards, they provide better heat dissipation.

Common ceramics used in DBC and DBA are silicon nitride, aluminum nitride, alumina, and beryllium oxide. DBS uses only alumina.

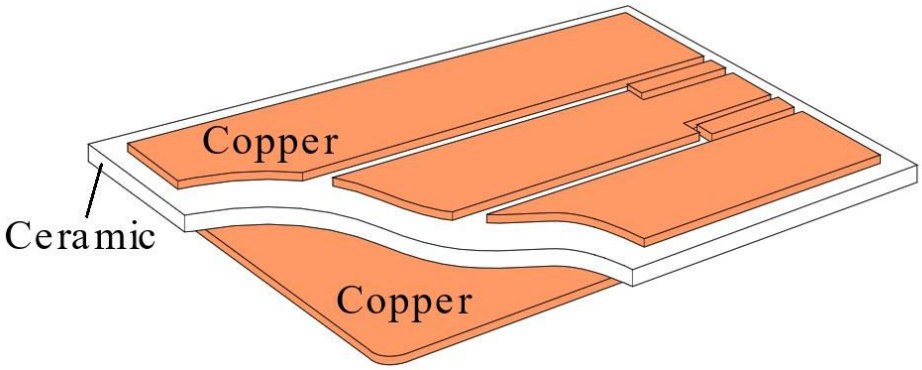


**Figure 1.4** Structure of a "Direct Bond Copper" (DBC) Substrate [2]

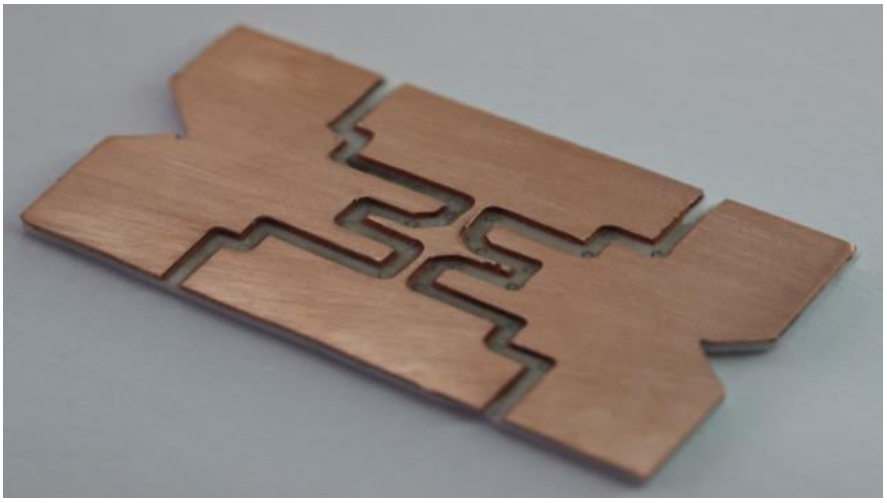

**Figure 1.5** DBC substrate for power LED [7]

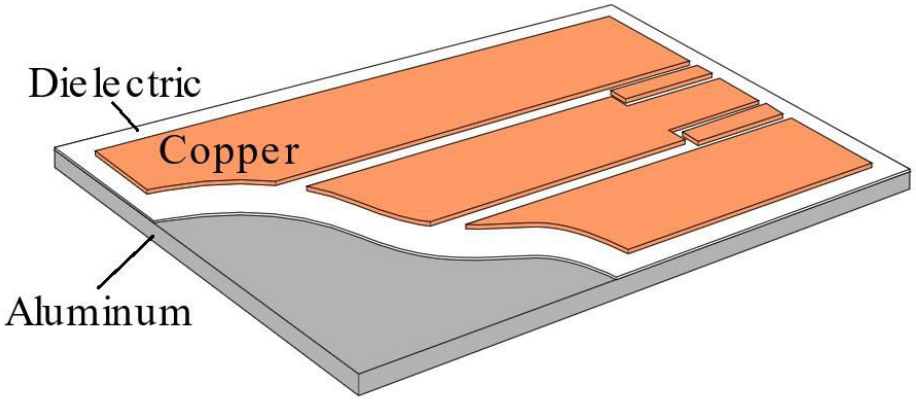


**Figure 1.6** Structure of an "Insulated Metal Substrate" (IMS) [2]

## 1.3 Direct bonded copper substrate (DBC)

Out of all substrate type discussed above the direct bonded copper substrate (DBC) (as first developed by Sun and Burgess [8], [9] in 1975) is the most efficient power electronic substrate. It is widely used in power modules because of its excellent thermal conductivity, high electric conductor current carrying capability across the top surface of the substrate, very high electrical insulation along the thickness of the substrate, low capacitance and controlled thermal expansion properties [10], [11]. The low coefficient of thermal expansion of the substrate makes it possible to solder silicon semiconductors with large-area directly unto the substrate surface without causing thermal fatigue failure[10]. Its high electrical insulation capabilities grantees the safety of all persons within the vicinity of a work power module [12]. The substrate has proven to be an excellent solution to thermal and electrical management of high power semiconductor modules [13].

The DBC substrate has a super-thin base and eliminates the need for heavy, thick copper bases that were used in the past. DBC encourages close packaging of power chips which implies more power chips per unit volume. This close packing of chips has resulted in an improvement of the efficiency and performance of power modules.

In the DBC substrates, the copper is bonded to the ceramic by a high-temperature oxidation process. In this process, the copper and ceramic are heated to a carefully controlled temperature in the presence of oxygen and pressed against each other, at this temperature, a copper-oxygen eutectic is formed which bonds the copper to the ceramic. The top layer copper of the substrate could be chemically etched (same technology used in printed circuit board) to form an electrical circuit or pathway, while the bottom layer is usually kept plain. Due to the high bonding strength between the copper and the ceramic, the coefficient of thermal expansion (CTE) of the substrate is always controlled by the properties of the ceramic [10]. The ceramic has the capabilities of reducing the overall CTE of the substrate to matching it with the CTE silicon semiconductors [10]. By varying the thickness of copper and ceramic or changing ceramic type, one could influence the overall resulting CTE value of the DBC substrate in order to avoid CTE mismatch with different semiconductors.

The top copper layer in the DBC substrate provides an electric pathway for the power components and semiconductors mounted on the substrate. The bottom copper layer effectively discharges the heat from the power components and semiconductor to the environment or heat sinks. The ceramic layer provides a rigid support for the top copper layer (electric pathway) and ensures electrical insulation between the electric circuit and the heat sink as seen in figure 1.7.

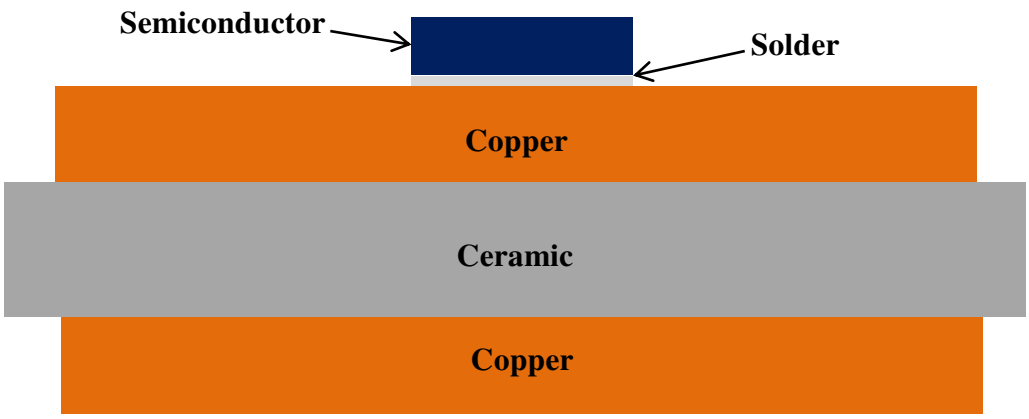


**Figure 1.7** Profile of a "Direct Bonded Copper" (DBC) Substrate

## 1.4 DBC Ceramics

Most ceramics materials have good mechanical and favorable thermal properties [14], as a result of these two desirable properties, ceramics are mostly used in variety of applications such as cryogenic applications [15], [16], structural applications, thermal barrier coatings [17]–[19], burners [19], heat sinks [20], electronic packaging (substrate for power devices) [17], [18], [21], cutting tools [22] and insulating layers/materials [19], [23]. Ceramics with high porosity fraction are used as thermal insulators due to the high thermal resistance provide by the pores [23]. Thus, the material used for DBC or DBC applications must possess the following properties:

1. Good thermal conductivity value for easy of heat dissipation and good heat spread capabilities
2. Coefficient of thermal expansion value close to that of silicon in order to avoid interface layers

3. Appreciable mechanical strength with a mechanically stable shape
4. Good thermal shock resistant
5. Good thermal cycling stability
6. Very good electrical insulator
7. Good adhesion and corrosion resistant
8. Environmentally friendly

Only few ceramic materials possess the above properties as discussed below:

1. **Alumina**: This is among the ceramic materials widely used for electronic applications. It is economical, popular and readily available as compared to other ceramic materials [24],. It exhibits an excellent structure as well as some desirable properties like high thermal conductivity, excellent compressive strength, lower dielectric characteristics, electrical insulation, good thermal and chemical stability. However, its use for certain applications is limited by its poor fracture toughness and mechanical properties [20], [25], [26] which can be improved by adding certain filler materials (e.g. carbon nanotubes, metallic particles (with the exception of silicon and manganese particles [25]), etc.) into alumina matrix. Alumina finds extensive applications in the electronic industries [20], [27], [28], biomedical [29], cryogenic engineering [15], [16], [21], wear and corrosion applications, cutting tools, thermal barrier coatings, etc.
2. **Aluminum nitride:** This is an electrically insulating ceramic material which has very high thermal conductivity, non-toxic nature [30] and stability at high temperatures. Aluminum nitride has a coefficient of thermal expansion close to that of silicon and a very good thermal shock resistance [31]. Aluminum nitride is commonly used for

surface acoustic wave sensors, radio frequency (RF) filter, ultrasound transducers, light emitting diodes, electronic substrates and other military applications. Although it has the most of the desired properties for DCB applications, it is very difficult to successfully bond metals to its surface due to its poor metal wetting property [32].

3. **Beryllium oxide**: This is an amorphous solid which also exhibits good electrical insulation and excellent thermal conductivity properties. Its thermal conductivity is even higher than that of some metals.

Out of all DBC ceramic materials, alumina and aluminum nitride are the only two environmental friendly ceramics. Even though, the two ceramics have gained lot of popularity in the electronic industry as electronic substrates, alumina is mostly used because of it low cost and availability. Beryllium oxide (which is relatively cheap as compared to alumina) and silicon nitride are not used because they emit toxic fumes when exposed to the environment. In DBC applications, alumina ceramic provide better bonding strength to copper surfaces as compared to other DBC ceramics, and this has singled out alumina as the most suitable ceramic for DBC substrate applications.

Table 1.1 summarizes the critical properties of all DBC ceramic materials ever used.

**Table 1.1** Properties of commonly available DBC ceramics [11], [33]

| | Purity | Density ($g/cm^3$) | Electrical resistivity (ohm-cm) | Dielectric strength (kV/mm) | Thermal conductivity ($W/m^2$-K) | CTE (µm/m°C) | Young's modulus (GPa) | Tensile strength (MPa) | Compressive strength (MPa) | Flexural strength (MPa) |
|---|---|---|---|---|---|---|---|---|---|---|
| Alumina | ≥96% | 3.96 | 1.0E+14 | 10 | 24-28 | 7.4 | 370 | 300 | 3000 | 400 |
| Aluminum nitride | ≥97% | 3.26 | 1.0E+10 | 14 | ≥150 | 4.5 | 330 | - | 2100 | 320 |
| Silicon nitride | - | 3.29 | 1.0E+12 | - | 30 | 3.2 | 300 | 350 | 3000 | 750 |
| Beryllium oxide | - | 3.02 | 1.0E+3 | - | ≥248 | 8 | 345 | - | - | - |

## 1.5 Problem description

Alumina has a lower thermal conductivity value as compared to aluminum nitride; this hinders its capability to efficiently dissipate heat across the DBC substrate when used as a DBC ceramic. In the present work, a new material which could replace alumina in DBC substrates is to be developed. The material is expected to have enhanced properties (such as thermal conductivity) as compared to alumina, but it must also be able to sustain the adhesive strength, economic and safety benefits of alumina. Thus, this new ceramic material will have more efficient heat dissipation capability than alumina when used for DBC application. Since no other material matches these desired characteristics, an alumina composite was selected. The composite should have better higher thermal conductivity and lower CTE properties as compared to commercial alumina.

## 1.6 Thesis Objectives

The objectives of this work are:

1. To design an alumina composite for use as DCB substrate material with enhanced properties(improved thermal conductivity and reduced coefficient of thermal expansion)
2. To develop and characterize the composite material
3. To evaluate the performance of DBC substrates.

# CHAPTER 2

# LITERATURE REVIEW

## 2.1 Electronic Substrate

New generation electronics use integrated or microelectronic circuits which are usually comprised of millions of interconnected resistors, transistors or other components built as a single assembly on a tiny chip of silicon. Maintaining the reliability and durability of these microelectronic circuits depends largely on the electrical and thermal properties of the materials which serve as the base on which these microscopic electronic components are mounted upon [34]. The materials which serve as the base upon which these microscopic electronic components are mounted on are known as electronic substrates.

Ceramics has become the most common electronic substrate materials due to their extra-low electrical and thermal conductive abilities; this enables them to be used as perfect heat dissipating electrical insulators. Out of all ceramic materials employed as electronic substrates, alumina is the most dominate material. The advantages of alumina over other ceramics include excellent thermal stability, high resistivity to electricity, good dielectric strength, excellent corrosion stability and mechanical strength, but it has a relatively low thermal conductivity and high dielectric constant.

The ceramic substrate is usually made as either thin or thick films. These films are commonly fabricated using the tape casting process. In tape casting, the ceramic

particles, fillers, and other additive materials are dissolved/dispersed in a solvent to form a slurry. The slurry is then layered onto a moving carrier and allowed to dry [35].

## 2.2 Earlier works on DBC substrates

Over the years, the core work into DBC substrates has mainly been either improving the bonding strength between the copper and ceramic surfaces or optimizing the DBC structural design to reduce failure. Recent research works so far on DBC ceramics were done to improve the thermal performance of DBC alumina ceramics.

Manufacturing of DBC substrates has solely been with $Al_2O_3$ and AlN ceramics. The manufacturing process uses a special fusing technique at a temperature range of 1065°C and 1085°C. At this temperature range, the copper reacts with oxygen on the surface of the ceramic to form a eutectic liquid of Cu-O and when cooled down the eutectic liquid consolidates with the copper plate and the ceramic to form a good bond [36], [37]. Surface treatment of the copper and ceramic surfaces is necessary before the consolidation process [7]. In another fusing technique, a thin layer of copper oxide applied at the interface between the copper and ceramic just before or during the bonding process, after which it is heated up to a temperature range between 1065 and 1083 °C. The copper oxide melts at its eutectic and meets the ceramic while the copper retains it solidity thereby creating a tight bond [38]–[40].

In a direct bonding routine, the copper and ceramic sheets are placed on top of each other ensuring a good contact over the entire area. The materials are placed in a muffle furnace

whose temperature is controlled by a defined temperature profile which is between the eutectic copper-copper oxide melting point (1065 °C) and that of copper (1083 °C). This temperature range is important for a proper connection between the copper and ceramic surfaces. The copper is only allowed to melt at its surface and not its entire volume and a low oxygen concentration must be maintained inside the furnace during the process. This developed technique would make it possible to produce DBC substrates with maximum copper thickness layer of about 0.7 mm which has been difficult to achieve by other previous methods [7].

Hot pressed AlN ceramic and oxygen-free high conductivity copper (OFHC) foil was used for the copper bonding experiments. The copper foils after cutting into the desired shape and degreased ultrasonically were bonded to the AlN ceramic substrate by heating the assembly at of 30 °C/min to a temperature range of 1065-1075°C for 5-60 minutes in a nitrogen atmosphere. It was concluded that modifying the surface of AlN or altering the chemical composition of the copper foil, a bond could be achieved. It was also concluded that a stronger bond exists between alumina and copper than aluminum nitride and copper which is due to the formation of an intermediate phase ($CuAlO_2$) between the interface of alumina and copper [11], [41]. In order to perform DBC process with aluminum nitride, before any bonding could be achieved, the surface of aluminum nitride has to me converted into alumina via the heat and oxygen [38].

Hong (2007) confirmed the formation of an intermediate phase ($CuAlO_2$) between the interface of the alumina substrate and copper sheet. He proposed a new method of bonding copper to ceramic; by applying a thin layer of cuprous oxide ($Cu_2O$) in-between the copper and alumina interface and heating to eutectic temperature in a nitrogen

atmosphere a firm bond was obtained. The bond showed no sign of de-bonding after 50 cycles of thermal fatigue which implied a very good thermal shock performance [36].

Over the years, there have been few research efforts as regards the reliability of DBC substrates. A relationship was found to exist between the partial pressure of oxygen during the manufacturing process and the interface bonding strength between copper and the ceramic [42]. In a research to study the relationship between thermal fatigue life and thermal (temperature) cyclic load, it was discovered that the thermal fatigue life of DBC substrates decreases as the peak temperature in thermal cycling was increased [11], [43].

In the decohesion of metal-ceramic interfaces, it was observed that plastic deformation occurring in the metal significantly influences the interface cohesion strength [44]. So it is important to pay more attention to the plasticity of the copper layers in DBC substrates and finite element analysis could be used to achieve this.

Pietranico [45], [46] in his works studied the mode of fracture mechanisms in DBC substrates. He observed and concluded that the fatigue life of DBC substrate corresponds to a fatigue crack growth in the copper region near the copper/ceramic interface when the critical temperature and cyclic conditions were reached. At these conditions the crack expands and breaks the ceramic, and also a natural defect in the ceramic could be a possible failure mechanism [45]. In summary, the fatigue life of a DBC substrate can easily determine the overall lifetime of the whole power electronic device [47], [48]. As the copper layer suffers from periodic plastic loading caused by thermal cycling load, the plastic strain will accumulate and finally causes the copper to fail.

An experimental setup was used to simulate the thermal cycling effects of DBC substrates. The samples were removed after every ten cycles at room temperature for observations under an optical microscope. The samples were observed for fatigue cracks at the interface between copper and the ceramic. After observations, the samples were kept back into the heating chamber and the thermal cycling continues. The fatigue crack in alumina DBC substrates do stop propagating in the alumina ceramic after some thermal cycling time. The copper layer does not split completely away from the ceramic [11].

The capacitance between the upper and bottom plates of a DBC substrate can be used as an aging indicator [46]. The DBC substrate can be regarded as a plate capacitor because an electrically insulating ceramic has been placed between two copper plates. Its capacitance is directly related to the copper layer area and the distance between the two copper plates. If a failure in the form of copper-alumina delamination or cracks in the ceramic occurs, the gap between the two copper plates increases thereby causing a reduction in capacitance value [49]. In other words, a drop in the capacitance value of a DBC substrate means the start of its failure.

Ductile materials like copper are susceptible to plastic failure whenever they come under several cycles of periodic plastic loads. In order to describe the cyclic failure mechanisms of ductile materials whose cycles are below $10^4$ cycles (low cycle fatigue (LCF)) and to predict the cyclic life of these materials under cyclic loads, the Manson-Coffin's law [50] as given in Eq. (2.1) is usually used. The equation is based on the plastic strain amplitude of the material under the cyclic load.

$$(N_f)^{\beta}\Delta\gamma^p = C^p \tag{2.1}$$

Where $\beta$ and $C^p$ represents fatigue ductility exponent and fatigue ductility coefficient respectively are material constants, $\Delta\gamma^p$ is the applied plastic strain rate and $N_f$ is the fatigue life.

In other situations where the number of cycles is very small, way below 100 cycles (extremely low cycle fatigue (ELCF)), Manson-Coffin law can't predict the cyclic life. Thus Xue's [51] model as shown Eq. (2.2) which is an improved version of Manson-Coffin law fits well for the prediction.

$$N = \frac{1}{2}\frac{e^{\lambda}-1}{e^{\lambda(\varepsilon_d/\varepsilon_f)^c}-1} \tag{2.2}$$

Where N is the fatigue life, c and $\lambda$ are material constants, $\varepsilon_d$ is a function of the plastic principle strains ($\varepsilon_1$, $\varepsilon_2$, $\varepsilon_3$) as seen in Eq. (2.3) and $\varepsilon_f$ is the total plastic failure strain.

$$\varepsilon_d = \sqrt{\frac{2}{3}} * \sqrt{{\varepsilon_1}^2 + {\varepsilon_2}^2 + {\varepsilon_3}^2} \tag{2.3}$$

In order to improve the reliability of alumina DBC substrates, a ladder-shaped DBC structure was proposed, the ladder shaped DBC when investigated proven to be stronger under thermal cycling loads [49]. Some researcher says that the fatigue life-cycle of alumina DBC substrates could be improved by increasing the copper yield strength or reducing the copper layer thickness because ductile copper has the tendency of alleviating stress concentration [11].

Zirconia toughened alumina (ZTA) ceramics has excellent bending strength and fracture toughness as compared to alumina and aluminum nitride. Its high performance-price-ratio

and heat dissipation capabilities close to that of alumina make it a good substitute in place of alumina for use as a DBC ceramic material. The ZTA for DBC was developed via tape casting at a sintering temperature of 1600 °C. By manipulating the structure of ZTA ceramic and the properties of copper, the lifetime of DBC substrate in thermal cycling could be extended by a factor of about two without a significant change in the bill of material [40].

## 2.3 Effective Thermal Conductivity

The effective thermal conductivity of a ceramic and its composites (especially alumina [22]) is always of general interest as it may influence the thermal performance and other properties like thermal shock resistance, modulus of elasticity or electrical conductivity directly or indirectly [19], [52]–[56]. Effective thermal conductivity is predominantly determined by the level of porosity in the ceramic material [23], [24], [57], the pore size distribution and microstructure organization [23]. Commercial alumina with a purity of about 96-97% has a thermal conductivity between 20-24 W/m$^2$-K [20], some 35 W/m$^2$-K [24], 28 W/m$^2$-K [27], but pure alumina is about 40 W/m$^2$-K [20] which is higher than those of most oxides and glasses [20].

The effective thermal conductivity ($K_e$) of composites were evaluated using the flash laser method [20], [22], [23], [57]–[62], this method measures the thermal diffusivity of the composite in question. A standard formula ($K_e = k\ \rho\ C_P$) relates these measured thermal diffusivity coefficient value ($k$) to thermal conductivity, where bulk density ($\rho$) of the composite and specific heat capacity ($C_P$) of the composite are calculated or

derived from literature. The laser flash technique involves heating up the front surface of the sample by an optical pulse, the temperature-time behavior of the rear surface is then monitored and analyzed to determine the characteristic times necessary for the calculation of thermal diffusivity using Degiovanni's equations.

Passing heat flux ($q$) through a test specimen material under steady state heating conditions, measuring the temperature difference ($\Delta T$) across the specimen's thickness ($l$) and evaluating the effective thermal conductivity ($K_e$) using $K_e = q\ l/\Delta T$ is another method used in evaluating the effective thermal conductivity of a material. This known as the steady-state laser heat flux test method [63].

It was demonstrated that temperature dependence of the thermal conductivity of a composite is not determined by simple summation of the thermal conductivity of its components, but it's being affected by new phases formed in reactions between the components while sintering. The composition dependence of the thermal conductivity of a composite can be determined by simple summation of the thermal conductivity of its components in the absence of a reaction between its components [64].

## 2.4 Earlier Works in Enhancing the Properties of Alumina

Earlier efforts in the past have been made to improve the thermal conductivity, fracture toughness and other properties of alumina by adding certain percentages of other material having the desired property to be enhanced. By adding certain percentages of copper powder, thermal conductivity and other electrical properties were slightly varied, which

was later traced back to the instability of copper in the presence of oxides at 900°C [27]. It was observed that metallic filler materials increase the fracture toughness of alumina.

The thermal conductivity of atmospheric sprayed plasma coatings of alumina mixed with carbon nanotubes (CNTs) was studied, but it was difficult to explain those factors that contributed to a decrease in thermal conductivity value as the percentage of CNTs in the matrix increased [65].

Zhan and Mukherjee also recorded a decrease in thermal conductivity values of CNT/$Al_2O_3$ composites synthesized using spark plasma sintering (SPS) [66], but in contrast, higher thermal conductivity values were recorded when the weight percent of CNTs in $Al_2O_3$ matrix was increased. The increased value of thermal conductivity was associated with the large density of the sample, the CNTs were synthesized on alumina powder by direct growth after which it was spark plasma sintered [67]. Multiwall carbon nanotubes (MWCNTs) synthesized by the decomposition of propylene in a Fe/$Al_2O_3$ catalyst was mixed with an alumina matrix using an ultrasonic mixer initially and later mixed in a ball miller for 24hr, the mixture was later sintered at 1400°C in vacuum for 3min using spark plasma sintering. The effective thermal conductivity and density of the resulting composite was found to be decreasing with an increase in MWCNTs fillers [58], which was associated with the presence of CNT agglomerates at higher volume fractions and in turn caused an increase in phonon-interface scattering by the nanotubes in the alumina matrix [58], [68]. Furthermore alumina powder added into dispersed and stabilized MWCNTs was ball milled for 24 hours while adding a temporary dispersant and binder, the obtained mixture was lyophilized in order to obtain a dry granulate form, the granulates were later then either hot pressed or rapid press at 1550℃ for densification

under an argon atmosphere [68]. Higher thermal conductivity values were observed from the hot pressed pure alumina samples than the rapidly pressed samples, but as CNTs were introduced into the alumina matrix, the high thermal conductivity values observed for the rapid press samples was declining as the percentage of CNTs in the alumina matrix increased, an improvement in electrical conductivity was also observed [68]. Also high-performance graphene/alumina nanocomposite with improved electrical and dielectric properties was synthesized by the reduction of graphene oxide at 1000℃ to give graphene; the resulting graphene dispersed in isopropyl alcohol was then ultrasonically and mechanically mixed with alumina also dispersed in isopropyl alcohol and dried in a hot water bath. The powder was spark plasma sintered at 1550℃ under a pressure of 50MPa in a vacuum [26].

Nickel/Alumina composites were produced by hot pressing blends of nickel and alumina in a graphite die in order to determine the phase morphology, electrical resistivity was seen to increase rapidly and tendering towards the resistivity value of pure nickel at a nickel volume fraction of 25% and above [69]. Liu [62] identified three methods for the synthesis of a nickel/alumina composite; the first method was to mix alumina powder with the desired amount of nickel-oxide powder, the mixture ball milled for 24h and reduced in a hydrogen atmosphere at 800℃ for 50h, then sintered at 1600℃ in a hydrogen atmosphere for 10h. The second method was similar to the first but just for the fact that the sintering temperature was at 1650℃ in a carbon monoxide atmosphere for an hour. The last method was to mix fine alumina powder with nickel nitrate, the mixture heat treated at 500℃ in a hydrogen atmosphere for 50h followed by hot pressing at 1400℃ in a vacuum for an hour under a load of 30MPa. The major differences of the

three composites produced were the particle size of the nickel component embedded in the alumina matrix, which was 1, 2.2 and 1 μm for the first, second and third respectively. Thermal properties of the composite deceased with a decrease in the filler particle size which was associated with the increase in interfacial area between alumina and nickel particles. It was suggested that in order to improve the thermal conductivity of alumina using nickel fillers, the particle sizes of the nickel has to be at least 1.4μm [62].

There is a strong dependence of matrix type, as well as silicon carbide (SiC) filler shape and size on the thermal behavior of the resulting composite. The addition of SiC platelets in the range of 0 – 30 vol% into alumina matrix increased its thermal conductivity and diffusivity when the samples were sintered via hot pressing at 1500℃ and 50MPa uniaxial pressure in an argon environment. It was also reported that thermal conductivity value increased with the improved SiC dispersion in alumina [22], but only a small increase in thermal conductivity values have so far been achieved when about 30% volume fraction of SiC was added to alumina matrix [70]–[72].

Powdered mixture of alumina and silver oxide ball milled in an ethanol solution for 24h, the resulting slurry mixture dried in a rotary evaporator followed by die-pressing at 100MPa and sintered in air at a temperature range between 1500 and 1700℃ for 1h, the Alumina/silver composite formed exhibited an increase in thermal conductivity as the volume content of silver in the alumina matrix increased [60].

According to Itoh [59], an alumina-mullite composite was developed by mixing both particles of alumina and mullite in an aqueous solution to form a fluid suspension, the suspension was dried at room temperature for 7 days. The dried powder was hot pressed

at a temperature range between 1723 and 1923K for 2h under a pressure of 39MPa in an argon atmosphere. Thermal conductivity was found to decline as the volume percent of mullite increases in the alumina-mullite composite [59].

In an alumina/chromium-carbide composite developed by a powdered mixture of alumina and chromium-carbide which was ball milled in deionized water for the 24h, dried and sintered by hot pressing at 1400℃ for 1h in an argon atmosphere under a pressure of 30MPa. The thermal conductivity value of the resulting composite decreased when 10 vol% of chromium-carbide was first introduced into the alumina matrix, but as the chromium-carbide content starts to increase so does the thermal conductivity value increased, this was associated with the formation of composite grain where the fine of chromium-carbide is being trapped inside the alumina grain which may scatter phonons more effectively [61].

In other cases alumina is been used as filler materials so as to improve the thermal conductivity of other materials, an example is adding alumina to zirconia matrix [73]. Nano-sized alumina was used successfully to improve the thermal conductivity and mechanical properties of silicon rubber (vinyl-end-blocked polymethylsiloxane) [74]. Nano and micro-alumina particles were also successfully used to improve the thermal conductivity of high-density polyethylene (HDPE) blends, the polymer composite was prepared by a two-roll mill at temperatures 140 and 130℃ for the front and back roll respectively, and then extruded by injection molding at 200℃ [75].

## 2.5 Effective Thermal Conductivity Analytical Model

From literature Maxwell [76] and Rayleigh [77] were one of the first to propose models in predicting the effective thermal conductivity for low dispersion particles. Later years Hadley [78] alongside Cunningham and Peddicord [79] developed an analytical model used in determining the thermal conductivity of materials with spherical fillers. Expressions for predicting the effective thermal conductivity of a composite with homogeneous matrix phase was derived by Hasselman and Johnson [80]. The expressions were derived by modifying the theories of Maxwell and Rayleigh [77]. The thermal conductivity mixing rule for composite materials was summarized by Wang and Pan [81]. Using Maxwell's, Hamilton's, reciprocity and the parallel models, the thermal conductivity of two-phase systems was analyzed [81]. In a more recent study, a thermal conductivity model developed by using alumina-mullite as a case study, the model shows the influence of pores and mullite particle size on the measured thermal conductivity value, but the model is effective only for composites with at least 25% porosity [59].

## 2.6 Chapter Summary

This chapter has provided:

- An exhaustive review of research works on various aspects power electronic substrates
- The knowledge gap in earlier investigations
- The objectives of the present work

- Also an extensive review of research works on various aspects of alumina and alumina composites

The next chapter would present the design and development of a new material to replace alumina as a DBC ceramic.

# CHAPTER 3

# MATERIAL DESIGN

## 3.1 Material Design

In this chapter, a methodology for the selection of an appropriate material configuration that best fits our target application is presented. In the case of a DBC ceramic, the designed material should exhibit better thermal conductivity and coefficient of thermal expansion than alumina while maintaining alumina properties like high elastic modulus, low electrical conductivity and good bonding to copper. Table 3.1 below shows the properties of alumina and the desired properties of our proposed material.

**Table 3.1** Properties of alumina and target properties of proposed material

| | Thermal Conductivity ($W/m^2$-K) | CTE (µm/m-°C) | Young's Modulus (GPa) | Electrical Conductivity (mho/cm) | Density ($g/cm^3$) |
|---|---|---|---|---|---|
| Alumina | 24 | 8 | 370 | < 1.0 E -10 | 3.92 |
| Proposed Material | 24 - 250 | 3 - 8 | 350 - 400 | < 1.0 E -10 | < 4 |

### 3.1.1 Matrix Selection

Based on the problem description, the new material should be able to maintain the adhesive strength, economic and environment benefits of alumina, but should have increased thermal conductivity and reduced coefficient of thermal expansion (CTE). The only viable way to achieve these objectives is by using an alumina matrix composite.

### 3.1.2 Filler Selection

Having decided alumina as the matrix material, the next task is the selection of the filler material for the composite. Candidate filler materials as shown in the table 3.2 below were chosen at random based on literature and certain properties that these materials possess. For the proposed material, its thermal conductivity and coefficient of thermal expansion values have to be higher and lower than that of alumina respectively and while trying as much as possible to maintain electrical conductivity values. The intending filler material has to possess high thermal conductivity and lower coefficient of thermal expansion values than that of alumina, alongside minimal electrical conductivity. Based on these criteria, some of the candidate filler materials were eliminated. Nickel, cobalt, and zirconium oxide were eliminated from the list of candidate filler materials because their coefficient of thermal expansion values are higher than that of alumina, adding them into alumina matrix would only further increase its CTE further. Fused silica, on the other hand, has a low thermal conductivity value and these would only reduce the thermal conductivity of alumina. Silicon and graphite have a low modulus of elasticity values, and these would only further reduce alumina's modulus of elasticity. The finalized list of candidate fillers is shown in Table 3.3

**Table 3.2** Properties of candidate filler materials, where alumina is used as benchmark for properties [2], [33]

| Candidate Filler Materials | Thermal Conductivity ($W/m^2$-K) | CTE (μm/m°C) | Young's Modulus (GPa) | Poisson Ratio | Electrical Resistivity (mho/cm) | Density ($g/cm^3$) | Melting Temp. (°C) |
|---|---|---|---|---|---|---|---|
| Alumina | 24 | 8 | 370 | 0.22 | <1.0E -14 | 3.96 | 2072 |
| Nickel | 60.1 | 13.1 | 207 | 0.31 | 14.3062E+6 | 8.89 | 1450 |
| Cobalt | 69.21 | 12.5 | 211 | 0.32 | 17.8574E+6 | 8.9 | 1495 |
| Chromium | 69.1 | 6.2 | 248 | 0.21 | 15.1515E+6 | 7.19 | 1950 |
| Silicon | 124 | 2.49 | 150 | 0.28 | 4.3478E-4 | 3.21 | 1414 |
| Silicon Carbide | 120 | 4 | 410 | 0.14 | 1.0E-4 | 3.1 | 2730 |
| Fused Silica | 1.38 | 0.55 | 73 | 0.17 | <1.0E-10 | 2.2 | 1715 |
| Diamond | 1200 | 1.18 | 950 | 0.18 | 1.0E-16 | 3.51 | 3550 |
| Graphite | 24 | 2.6 | 4.8 | 0.18 | 10.2040E+4 | 2.26 | 5530 |
| Zirconium oxide | 2 | 10.3 | 210 | 0.18 | <1.0E-10 | 5.5 | 2715 |

**Table 3.3** Selected filler materials and their properties

| Candidate Filler Materials | Thermal Conductivity ($W/m^2$-K) | CTE (μm/m°C) | Young's Modulus (GPa) | Poisson Ratio | Electrical Resistivity (mho/cm) | Density ($g/cm^3$) | Melting Temp. (°C) |
|---|---|---|---|---|---|---|---|
| Chromium | 69.1 | 6.2 | 248 | 0.21 | 15.1515E+6 | 7.19 | 1950 |
| Silicon Carbide | 120 | 4 | 410 | 0.14 | 1.0E-4 | 3.1 | 2730 |
| Diamond | 1200 | 1.18 | 950 | 0.18 | 1.0E-16 | 3.51 | 3550 |

### 3.1.3 Filler Volume Fraction and Particle Size Selection

The volume fraction of filler materials in a particulate filled composite has a direct effect on the properties of the composite formed; the filler volume fraction may improve or reduce some certain properties of the composite. It is necessary to investigate the effects of this filler volume fraction and particle size on our properties of interest which include thermal conductivity, coefficient of thermal expansion, modulus of elasticity and electrical conductivity.

In addition, the particle sizes of the filler particles in a particulate filled composite has a direct effect on the thermal conductivity of the composite. Below a certain filler particle size (known as the critical diameter or particle size), effective thermal conductivity values of particulate composites would only reduce upon filler addition. This is due to

the increase in the surface area of the inclusion particles as their size reduces. This has a direct effect on thermal interfacial resistance between the particles of the filler and the matrix materials. In selecting the appropriate filler particle size and volume fraction, the flow chart in figure 3.1 below would be considered as a guild line for the selections.

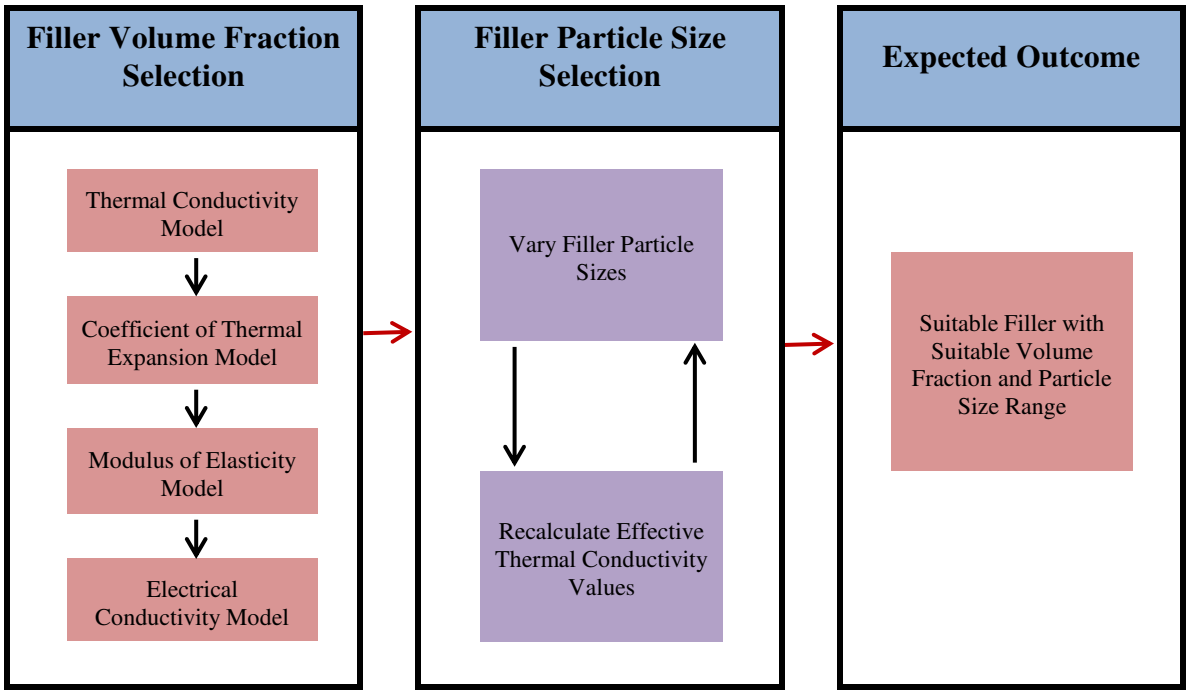


**Figure 3.1** Flow chart for the filler volume fraction and particle size selection

The thermal conductivity model used in predicting the effective thermal conductivity values of a particulate filler composite was the product of an NSTIP project [82]. The model is based on the multi-inclusion effective medium theory. The model can take into account effects like the size, shape, orientation and volume fraction of all inclusions and porosity. The model also takes into consideration the interfacial thermal resistance between the matrix and inclusion particles. The thermal resistance arises due to material

mismatch and imperfect interface conditions between the matrix and filler materials.. Table 3.4 shows the thermal interface resistance values used in the model for the three finalized candidate filler materials. The model is shown in Eq. (3.1) and (3.2).

**Table 3.4** Thermal interfacial resistant values and packing factors of filler materials [2], [83], [84]

| Filler Material | Thermal Interfacial Resistant Value with Alumina ($m^2$-K/W) | Packing Factor | Density ($g/cm^3$) |
|---|---|---|---|
| Chromium | 2.439 x$10^{-9}$ | 0.682 | 7.19 |
| Silicon Carbide | 5.556 x$10^{-9}$ | 0.6046 | 3.1 |
| Diamond | 6 x$10^{-8}$ – 7 x$10^{-8}$ | 0.34 | 3.51 |

$$K_{eff,11} = K_{eff,22} = K_m \frac{2+\sum_{i=1}^{N} \varphi_i \left[ \beta_{11}^i (1-L_{11}^i)\left(1+(cos^2\theta)^i\right)+\beta_{33}^i (1-L_{33}^i)\left(1-(cos^2\theta)^i\right)\right]}{2-\sum_{i=1}^{N} \varphi_i \left[ \beta_{11}^i L_{11}^i (1+(cos^2\theta)^i)+\beta_{33}^i L_{33}^i (1-(cos^2\theta)^i)\right]} \quad (3.1)$$

$$K_{eff,33} = K_m \frac{1+\sum_{i=1}^{N} \varphi_i \left[ \beta_{11}^i (1-L_{11}^i)\left(1-(cos^2\theta)^i\right)+\beta_{33}^i (1-L_{33}^i)\left((cos^2\theta)^i\right)\right]}{1-\sum_{i=1}^{N} \varphi_i \left[ \beta_{11}^i L_{11}^i (1-(cos^2\theta)^i)+\beta_{33}^i L_{33}^i ((cos^2\theta)^i)\right]} \quad (3.2)$$

Where;

$$\beta_{ii} = \frac{K_{ii}^c - K_m}{K_m + L_{ii}(K_{ii}^c - K_m)} \quad (3.3)$$

$$(cos^2\theta) = \frac{\int \rho(\theta) cos^2\theta \sin\theta d\theta}{\int \rho(\theta) sin\,\theta d\theta} \quad (3.4)$$

Where $K_{eff,11}$, $K_{eff,22}$ and $K_{eff,33}$ are the effective thermal conductivity values of the composite in all three components, $K_m$ is the thermal conductivity value of the composite matrix, $\varphi_i$ is the volume fraction of all inclusion, $\theta$ is the orientation of inclusions, $\rho(\theta)$ is a distribution function describing an ellipsoidal particle orientation and $L_{ii}$ are geometrical factors which is dependent of the particle shape [84].

The effective coefficient of thermal expansion model is based on the mean-field homogenization theory and the works of Benveniste [85]; the model as seen in Eq. (3.5) is capable of predicting the effective coefficient of thermal expansion of a particulate filled composite.

$$\alpha_{eff} = \alpha_i I_2 + c_i(C_i^{-1} - C_M^{-1})W\big((1-c_i)I_4 + c_i W\big)^{-1}(C_i^{-1} - C_M^{-1})^{-1}(\alpha_i I_2 - \alpha_M I_2) \tag{3.5}$$

$$W = C_i A_i C_M^{-1} \tag{3.6}$$

Where $\alpha_{eff}$ is the effective coefficient of thermal expansion of the particulate composite, $\alpha_m$ is the coefficient of thermal expansion of the matrix, $\alpha_i$ is the coefficient of thermal expansion of all inclusions, $C_m$ is the stiffness tensors of the matrix, $C_i$ is the stillness tensors of all inclusions, $c_i$ is the volume fractions of all inclusions, and lastly, $I_2$ and $I_4$ are the second and fourth order identities respectively.

The modulus of elasticity model is a mean-field homogenization based model developed by Doghri et al. [86] and is based on Eshelby's 1965 seminal work. The strain distribution at the micro-scale was related to the macro-scale strains using Eq. (3.7).

$$E\,(x) = A\,(x)\,\bar{E}_M \tag{3.7}$$

The homogenized elasticity tensor can be calculated using Eq. (3.8)

$$\bar{C_M} = \sum_i c_i C_i A_i \tag{3.8}$$

And from Mori-Tanaka scheme

$$A_i = \left[ I + S_M C_M^{-1} \left( C_{I,i} - C_M \right) \right]^{-1} \tag{3.9}$$

$$A_{(MT),i} = \left[ c_i I + c_m ( A_i )^{-1} + \sum_j c_i A_j ( A_i )^{-1} \right]^{-1} \tag{3.10}$$

$$\bar{C}_{(MT)} = C_M + \sum_i c_i \left( C_i - C_M \right) A_{(MT),i} \tag{3.11}$$

Where $C_i$ the elastic strain tensor of inclusions, $c_i$ is the volume fraction of inclusions present, $A_{(MT),i}$ is the localized strain tensor of all inclusions and $I$ is the fourth order identity.

The electrical conductivity model by Pal R. 2007 [87] was used in predicting the effective electrical conductivity property of a particulate filler composite. The equation as seen in Eq. (3.12) is a general equation can be used to effectively predict the effective electrical conductivity of composites.

$$(\sigma_r)^{1/3} \left( \frac{\lambda - 1}{\lambda - \sigma_r} \right) = \left( 1 - \frac{\phi}{\phi_m} \right)^{-\alpha \phi_m} \tag{3.12}$$

$\sigma_r$ The relative electrical conductivity defined as $\sigma / \sigma_m$ , $\lambda$ is the electrical conductivity ratio defined by $\sigma_d / \sigma_m$, and where $\sigma$ is the effective electrical conductivity value of the composite, $\sigma_m$ is the electrical conductivity value of the matrix phase, $\sigma_d$ is the electrical conductivity value of the filler, $\phi$ is the filler volume fraction, $\phi_m$ is the maximum packing factor of filler particles and $\alpha$ is a correction factor of the order unity which

accounts for the deviations from the assumptions made by Maxwell in his electrical conductivity model derivation.

For conducting particles dispersed in non-conducting matrix such that $\lambda \rightarrow \infty$, the general equation becomes Eq. (3.13);

$$\sigma_r = \left(1 - \frac{\phi}{\phi_m}\right)^{-3\alpha\phi_m} \tag{3.13}$$

And for insulating particles dispersed in conducting matrix such that $\lambda \rightarrow 0$, the general equation becomes Eq. (3.14);

$$\sigma_r = \left(1 - \frac{\phi}{\phi_m}\right)^{3\alpha\phi_m/2} \tag{3.14}$$

These models would be used to determine the resulting properties of the composites formed when any of the three selected individual filler materials in table 3.5 at varying volume fraction is combined with an alumina matrix. The results from the models would be analyzed in order to select the appropriate suitable filler volume fraction and filler particle sizes.

In the models used, all inclusions were assumed to be a perfect spheroid with even sizes, shape, orientation and uniform dispersion across the matrix. Interfacial interactions between the particles of the matrix and filler material is been taken care of within the thermal conductivity model by introducing a thermal interfacial resistant value, but this interfacial interaction effect is not considered in the other models used as they consider a perfect bond between the matrix and filler phases.

The modulus of elasticity, coefficient of thermal conductivity and electricity conductivity model do not consider the effects of the filler particle size. Only the thermal conductivity model considers this effect.

The three fillers would now be studied individually, and the property estimation models would be used to evaluate the properties of the resulting composites.

**Table 3.5** Properties of alumina and target properties of proposed composite material

| Proposed Material | | Thermal Conductivity ($W/m^2$-K) | CTE (µm/m°C) | Young's Modulus (GPa) | Electrical Conductivity (mho/cm) | Density ($g/cm^3$) |
|---|---|---|---|---|---|---|
| Matrix | Filler | | | | | |
| Alumina | Nil | 24 | 8 | 370 | < 1.0 E -14 | 3.92 |
| | • Chromium<br>• Silicon Carbide<br>• Diamond | 24 - 250 | 3 - 8 | 350-400 | < 1.0 E -10 | < 4 |

### 1. Chromium Filler

Figure 3.2 below was generated using the effective thermal conductivity model discussed earlier. If a large enough particle size is used, it can be seen that the effective thermal

conductivity value of an alumina/chromium composite will increase as the volume fraction of chromium in alumina increases. This is due to the fact that chromium has a higher thermal conductivity value than alumina and the surface area of the particles is large enough to overcome the thermal interfacial resistance value between the two materials.

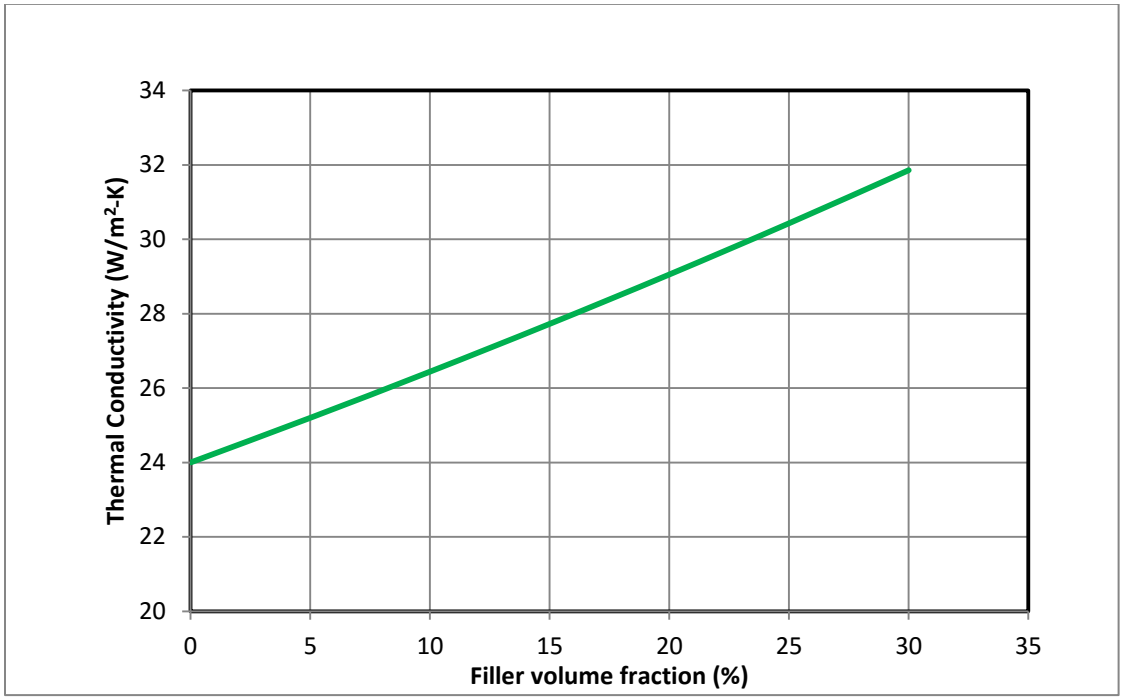


**Figure 3.2** Effective thermal conductivity of alumina composites against chromium filler volume

Figure 3.3 shows the variation of the numerically derived effective CTE values of the alumina/chromium composite as it varies with volume fraction of chromium fillers. If the composite were to be developed, the property value is expected to behave as shown in the figure because the filler material has a lower CTE than the matrix material, and the

combination of the two materials would result in a CTE mismatch and thereby reducing the overall CTE value of the composite.

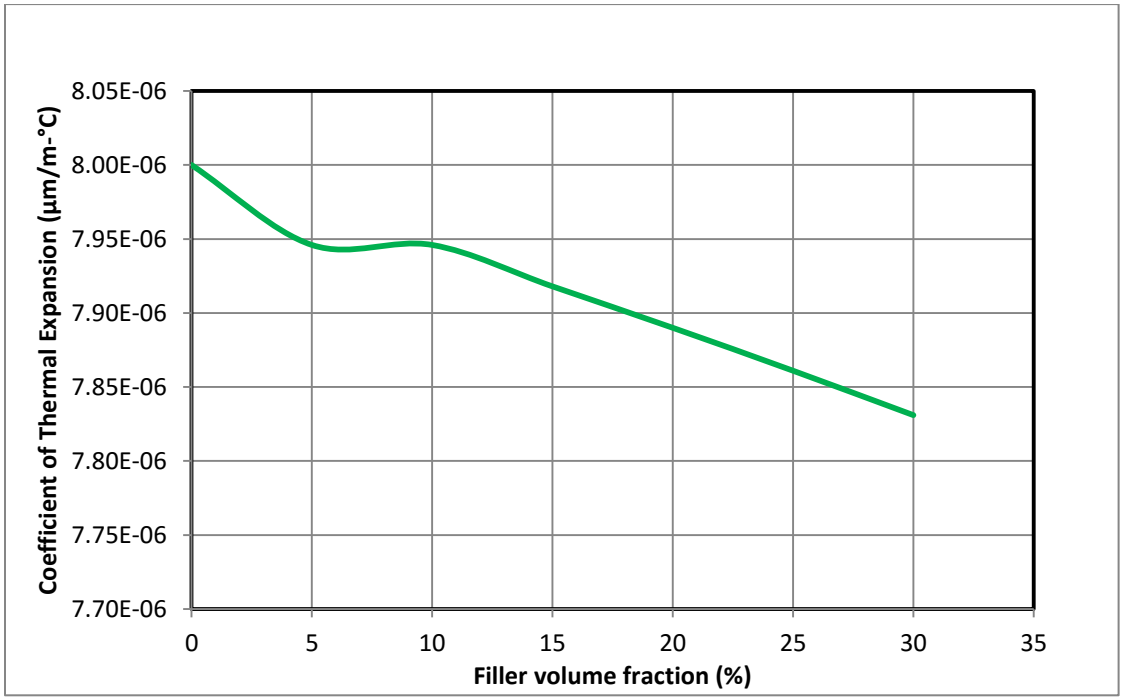


**Figure 3.3** Effective coefficient of thermal expansion of alumina composite against chromium filler volume

The behavior of figure 3.4 which shows the variation of the effective modulus of elasticity of the composite with filler volume fraction is similar to the behavior the effective CTE as shown in figure 3.3.

Figure 3.5 is a plot of the effective electrical conductivity of the alumina/chromium composite as it varies with the volume fraction of chromium in alumina. The values from the plot which was derived analytically shows the increase in the electrical conductivity

of the composite as the volume fraction of chromium fillers increases in the alumina matrix. The plot is justifiable as chromium is an electrical conducting material while alumina is an electrical insulating material.

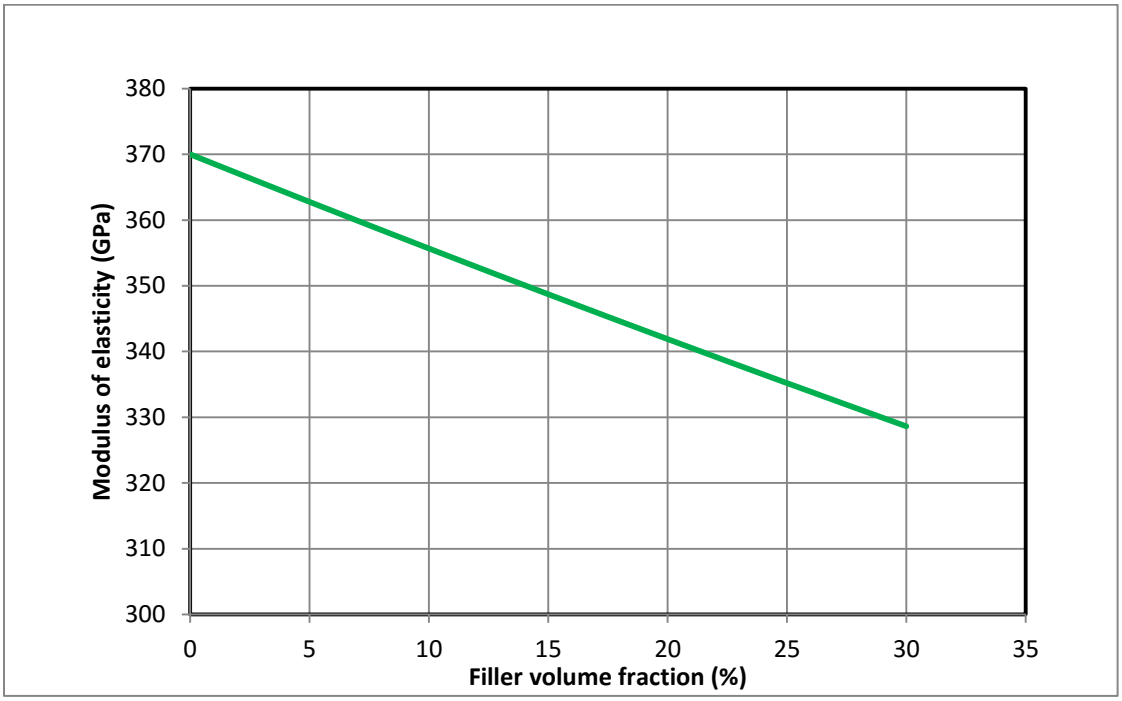


**Figure 3.4** Effective modulus of elasticity of alumina composite against chromium filler volume

Figure 3.6 which show the density variation of the alumina composite as the volume fraction of filler increases. The values from the plot were derived using the rule of mixtures in order to calculate the density of the resulting composite material as it the volume fraction of fillers increases. It could be seen from the plot that the density of the composite increases as the volume fraction of the filler increases, and this could simply be associated with the fact that chromium has a far more high density value than alumina.

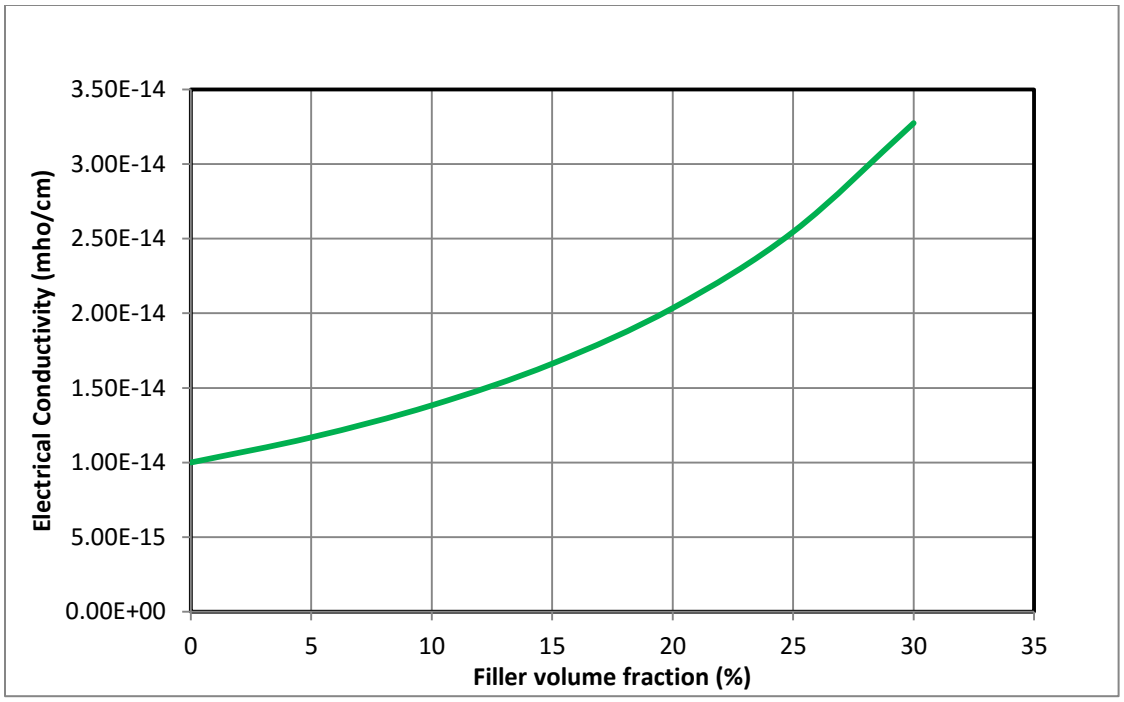


**Figure 3.5** Effective electrical conductivity of alumina composite against chromium filler volume

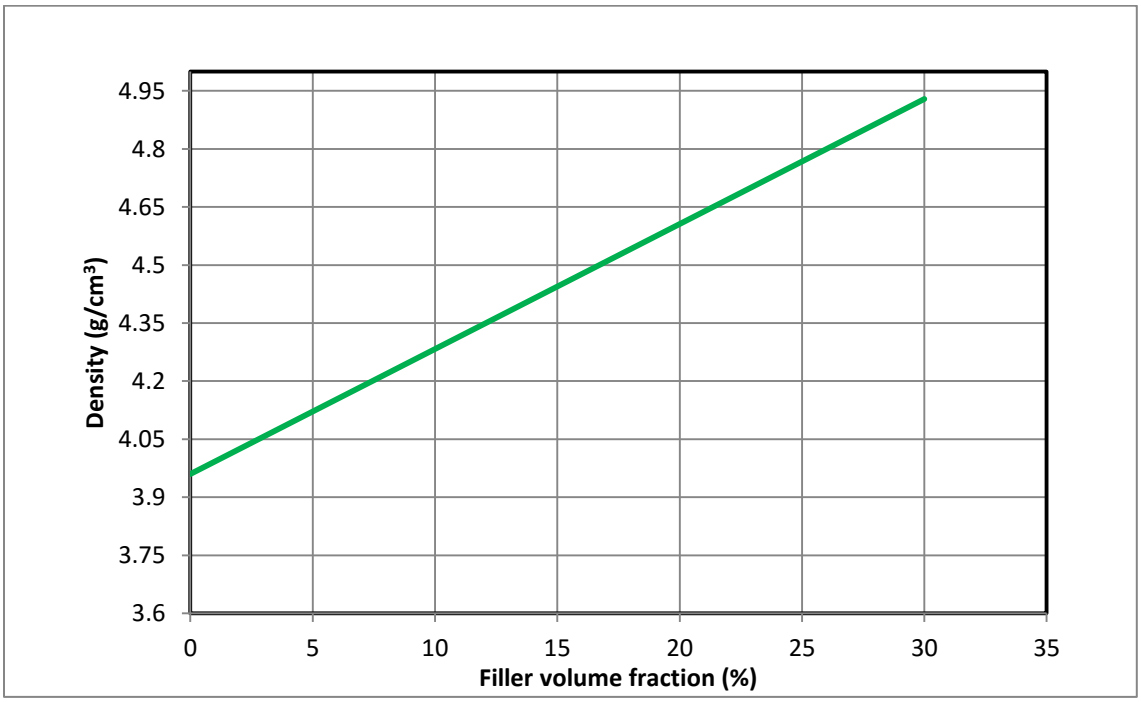


**Figure 3.6** Density of alumina composite against chromium filler volume

From figure 3.4 it can be seen that the modulus of elasticity of alumina reduces with increase in the volume fraction of chromium. Beyond 15% volume fraction of chromium, the modulus of elasticity value of alumina falls below our target property value of 350GPa. Therefore, the maximum allowable volume fraction of alumina is fixed at 15%.Likewise, a minimum benchmark was fixed at 5% volume fraction of chromium because at 5% one could observe a tangible improvement in the thermal conductivity and CTE properties of alumina composite.

The effective thermal conductivity value of particulate composites is a direct function of the filler particle size. Below a certain filler particle size, thermal conductivity value would only decrease upon an increase in the filler volume fraction. Above this critical size, effective thermal conductivity of the composite will increase with increase in filler volume fraction which is clearly shown in figure 3.7. Below the critical filler particle size, the surface area of the filler particle is too small to overcome the interfacial thermal resistant value between matrix and filler.

Figure 3.7 shows the variation of the effective thermal conductivity value of the alumina composite with chromium filler particle sizes for the two limiting volume fractions that were decided from figures 3.2 to 3.6. From figure 3.7, the minimum particle size which could enhance the thermal conductivity value of alumina is around 0.5µm. Below 0.5µm, thermal conductivity would only decrease and not increase. An average particle size of 5µm could be selected because at this value the effective thermal conductivity value of the resulting alumina composite would not improve significantly.

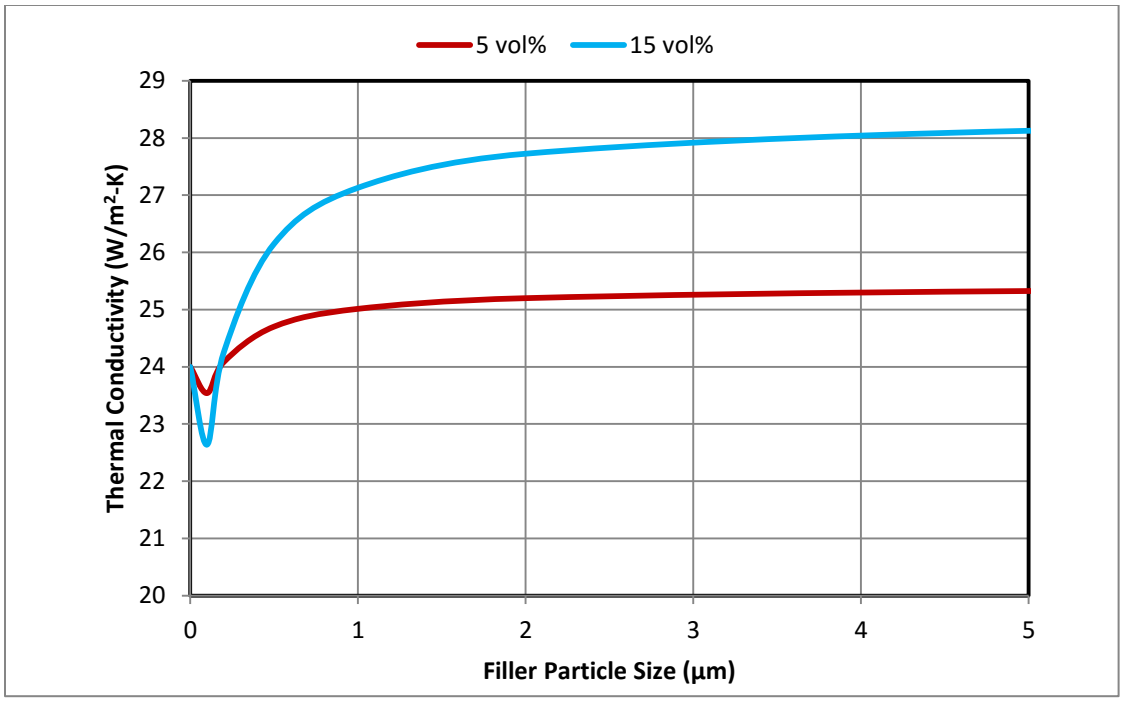


**Figure 3.7** Effective thermal conductivity of alumina composite against chromium filler particle sizes

## 2. Silicon Carbide Filler

Figure 3.8 below was also generated using the effective thermal conductivity model discussed earlier. If a large enough particle size is used, it can be seen that the effective thermal conductivity value of an alumina/silicon carbide composite will increase as the volume fraction of silicon carbide (SiC) in alumina increases. This is due to the fact that SiC has a higher thermal conductivity value than alumina and the surface area of the particles is large enough to overcome the thermal interfacial resistance value between the two materials.

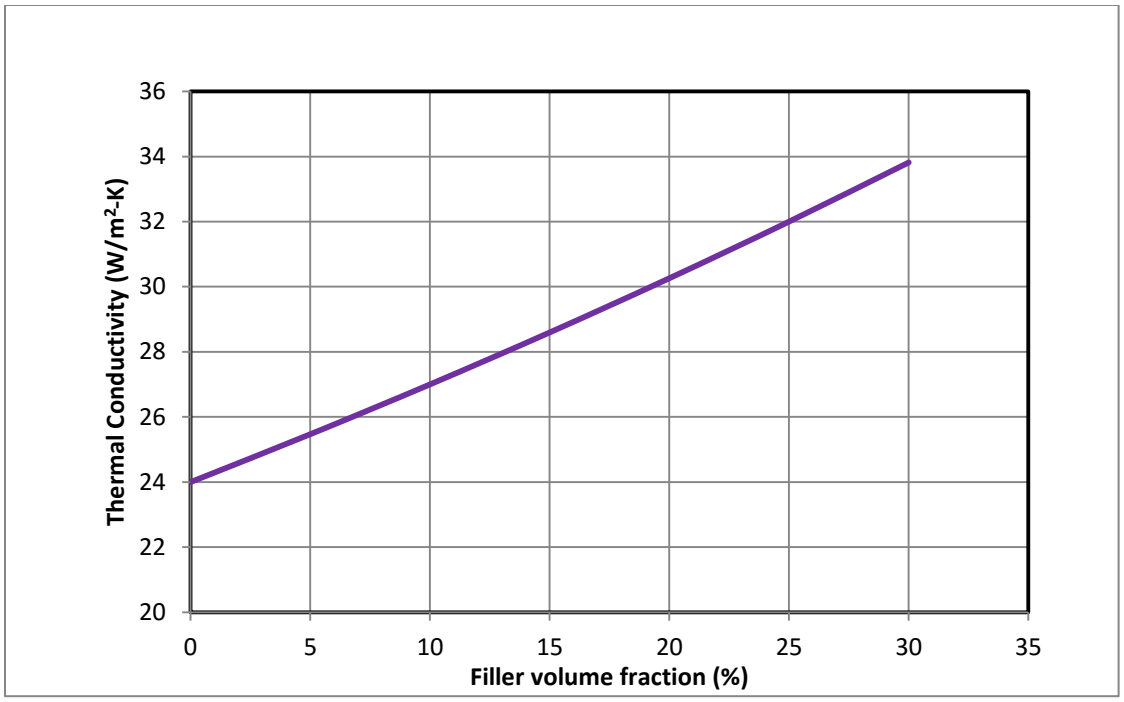


**Figure 3.8** Effective thermal conductivity of alumina composite against silicon carbide filler volume

Figure 3.9 shows the variation of the numerically derived effective CTE values of the alumina/ silicon carbide composite as it varies with volume fraction of SiC fillers. If the composite were to be developed, the property value is expected to behave as shown in the figure because the filler material has a lower CTE than the matrix material, and the combination of the two materials would result in a CTE mismatch and thereby reducing the overall CTE value of the composite.

The behavior of figure 3.10 which shows the variation of the effective modulus of elasticity of the composite with filler volume fraction is similar to the behavior the effective thermal conductivity as shown in figure 3.8. As the volume fraction of silicon carbide increases in the matrix, the effective modulus of elasticity of the composite increases because SiC has a higher

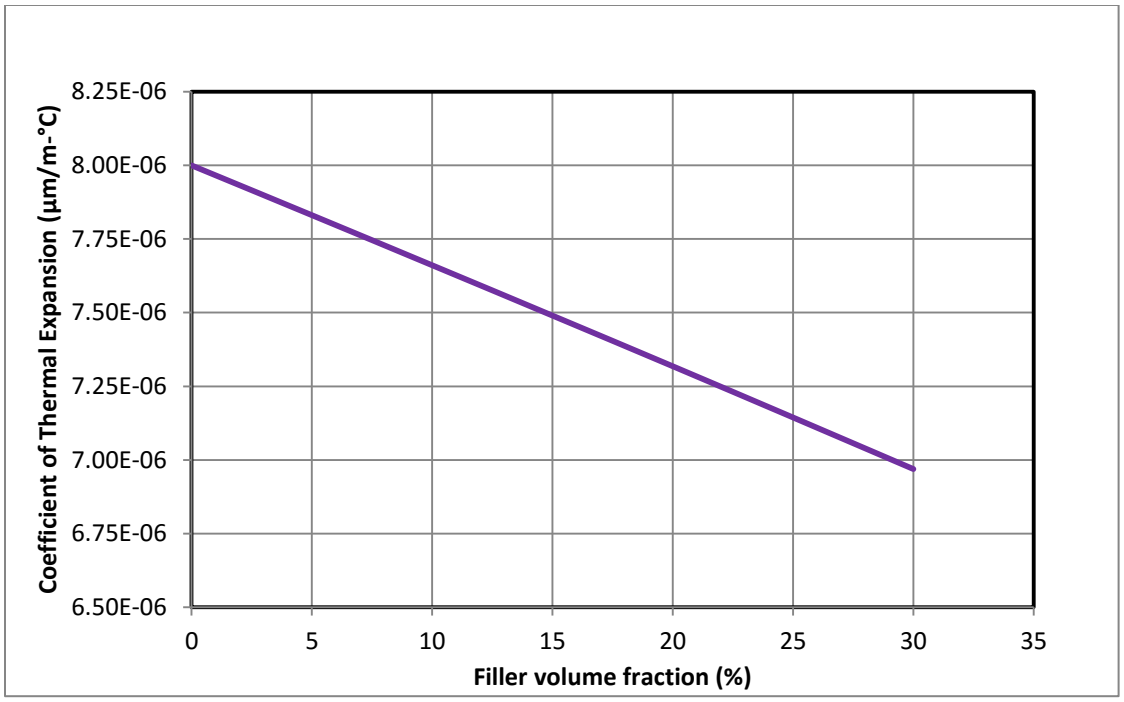


**Figure 3.9** Effective coefficient of thermal expansion of alumina composite against silicon carbide filler volume

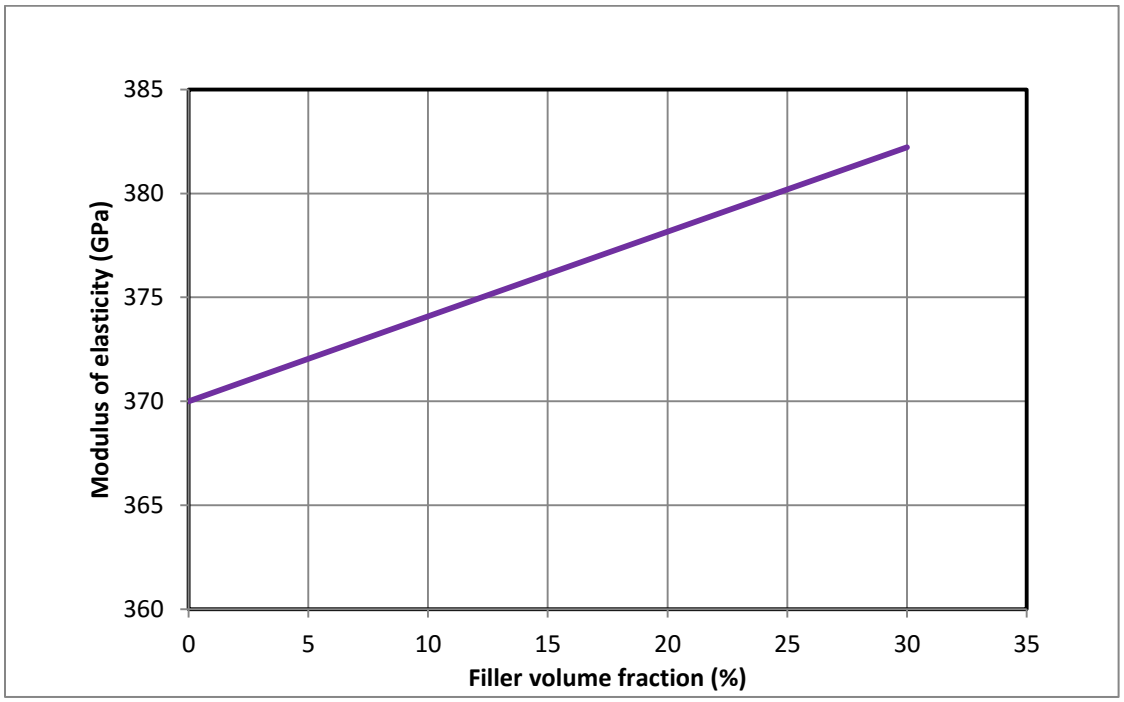


**Figure 3.10** Effective modulus of elasticity of alumina composites against silicon carbide filler volume

Figure 3.11 is a plot of the effective electrical conductivity of the alumina/silicon carbide composite as it varies with the volume fraction of SiC in alumina. The values from the plot which was derived analytically shows the increase in the electrical conductivity of the composite as the volume fraction of SiC fillers increases in the alumina matrix. Even as the electrical conductivity of the material increases, the resulting composite would still remain an electrical insulating material. The plot is justifiable as SiC has less electrical resisting capability than alumina.

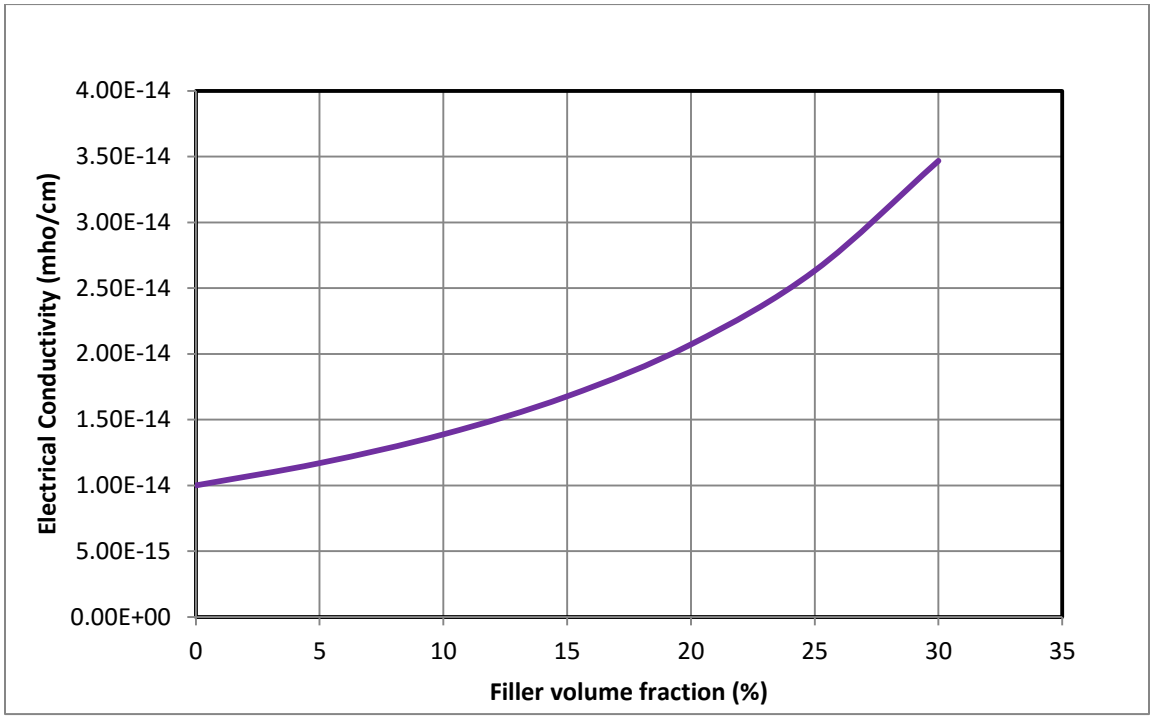


**Figure 3.11** Effective electrical conductivity of alumina composite against silicon carbide filler volume

Figure 3.12 show the density variation of the alumina composite as the volume fraction of filler increases. The values from the plot were also derived using the rule of mixtures.

It could be seen from the plot that the density of the composite decreases as the volume fraction of the filler increases, and this could simply be associated with the fact that SiC is lower density value as compared to alumina.

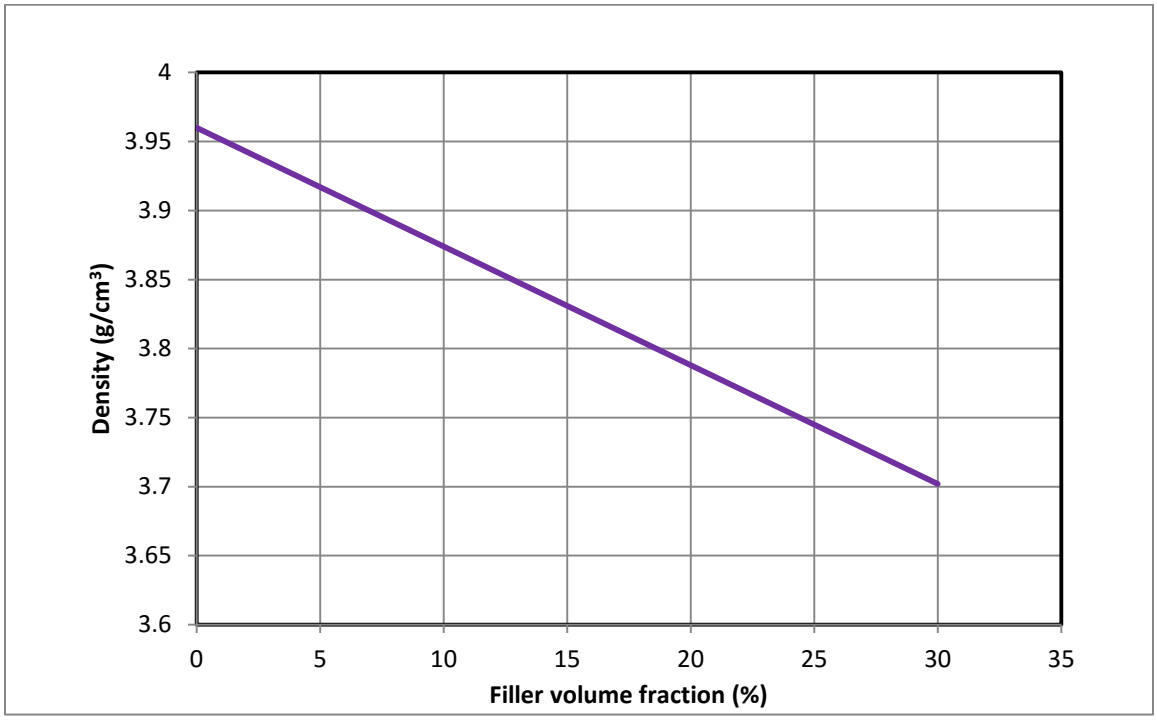


**Figure 3.12** Density of alumina composite against silicon carbide filler volume

From figures 3.8 to 3.12 all properties seemed to be in the range of our stipulated target properties, but it's still necessary we fix a benchmark to the SiC filler volume fraction. 20% SiC filler volume fraction in alumina matrix was fixed as the maximum benchmark; it's not advisable to go beyond 20% as other properties attributed with alumina might be lost. A minimum benchmark was fixed at 5% SiC filler volume fraction because at that

volume fraction one could observe a tangible improvement in the thermal conductivity and CTE properties of alumina composite.

The effective thermal conductivity value of particulate composites is a direct function of the filler particle size. Below a certain filler particle size, thermal conductivity value would only decrease upon an increase in the filler volume fraction. Above this critical size, effective thermal conductivity of the composite will increase with increase in filler volume fraction which is clearly shown in figure 3.13. Below the critical filler particle size, the surface area of the filler particle is too small to overcome the interfacial thermal resistant value between matrix and filler.

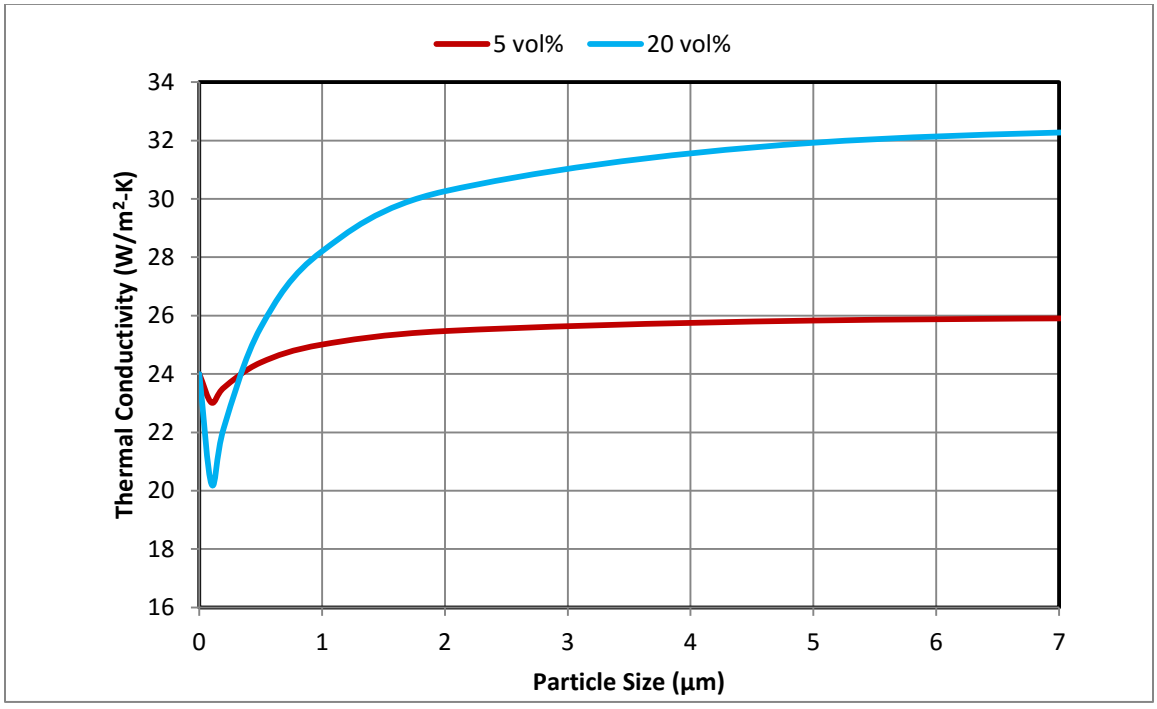


**Figure 3.13** Effective thermal conductivity of alumina composite against silicon carbide filler particle sizes

Figure 3.13 shows the variation of the effective thermal conductivity value of the alumina composite with SiC filler particle sizes for the two limiting volume fractions that were decided from figures 3.8 to 3.12. From figure 3.13, the minimum particle size which could enhance the thermal conductivity value of alumina is around 0.75µm. Below 0.75µm, thermal conductivity would only decrease and not increase. An average particle size of 7µm could be selected because at this value the effective thermal conductivity value of the resulting alumina composite would not improve significantly.

### 3. Diamond Filler

Figure 3.14 was generated using the effective thermal conductivity model discussed earlier. If a large enough particle size is used, it can be seen that the effective thermal conductivity value of an alumina/diamond composite will increase as the volume fraction of diamond in alumina increases. This is due to the fact that diamond has a higher thermal conductivity value than alumina and the surface area of the particles is large enough to overcome the thermal interfacial resistance value between the two materials.

Figure 3.15 shows the variation of the numerically derived effective CTE values of the alumina/diamond composite as it varies with volume fraction of diamond fillers. If the composite were to be developed, the property value is expected to behave as shown in the figure because the filler material has a lower CTE than the matrix material, and the combination of the two materials would result in a CTE mismatch and thereby reducing the overall CTE value of the composite.

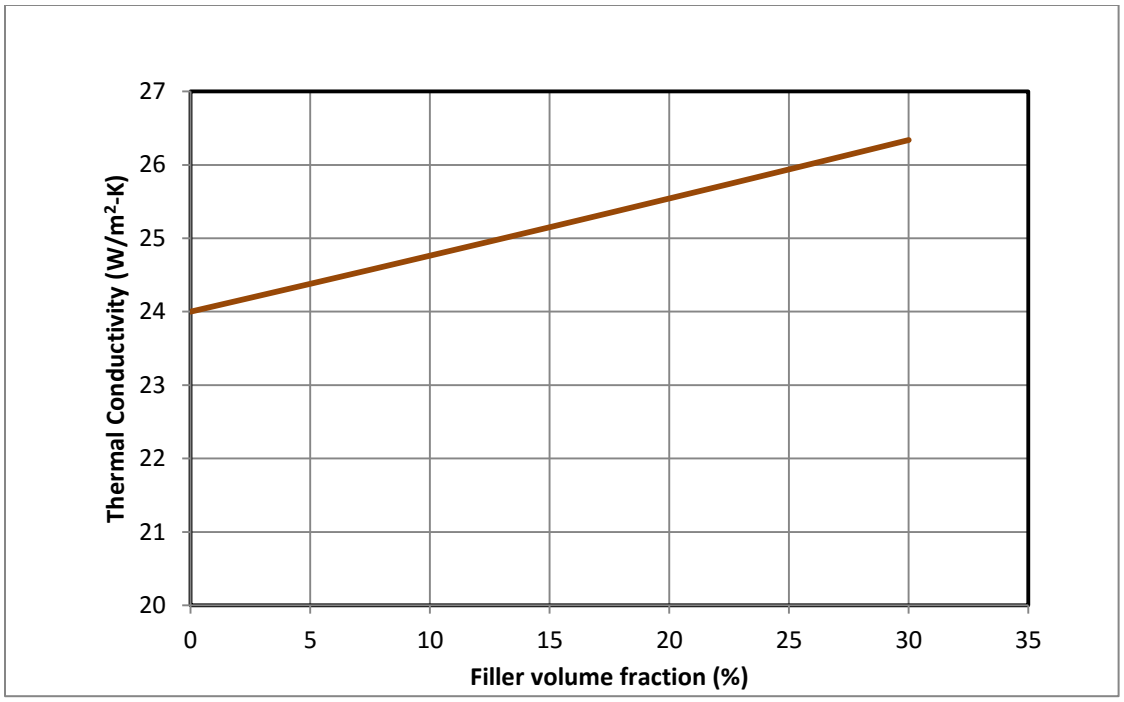


**Figure 3.14** Effective thermal conductivity of alumina composite against diamond filler volume

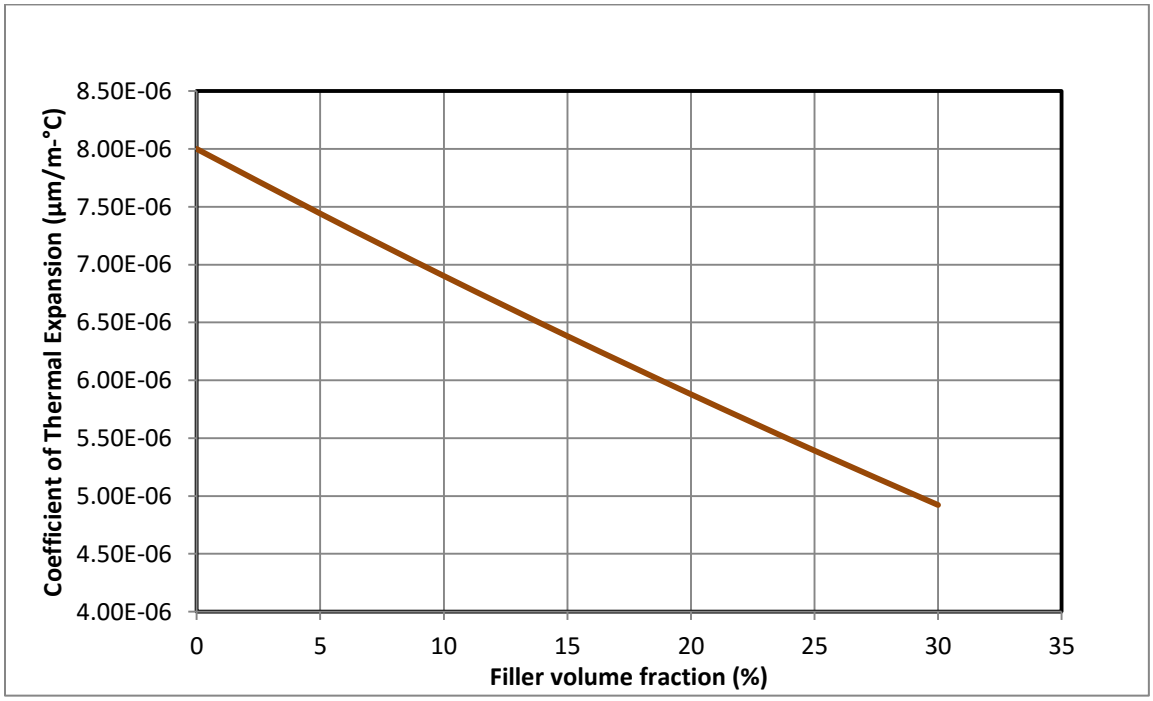


**Figure 3.15** Effective coefficient of thermal expansion of alumina composite against diamond filler volume

The behavior of figure 3.16 which shows the variation of the effective modulus of elasticity of the composite with filler volume fraction is similar to the behavior the effective thermal conductivity as shown in figure 3.14. The increase is expected because diamond has a much higher modulus of elasticity value than alumina.

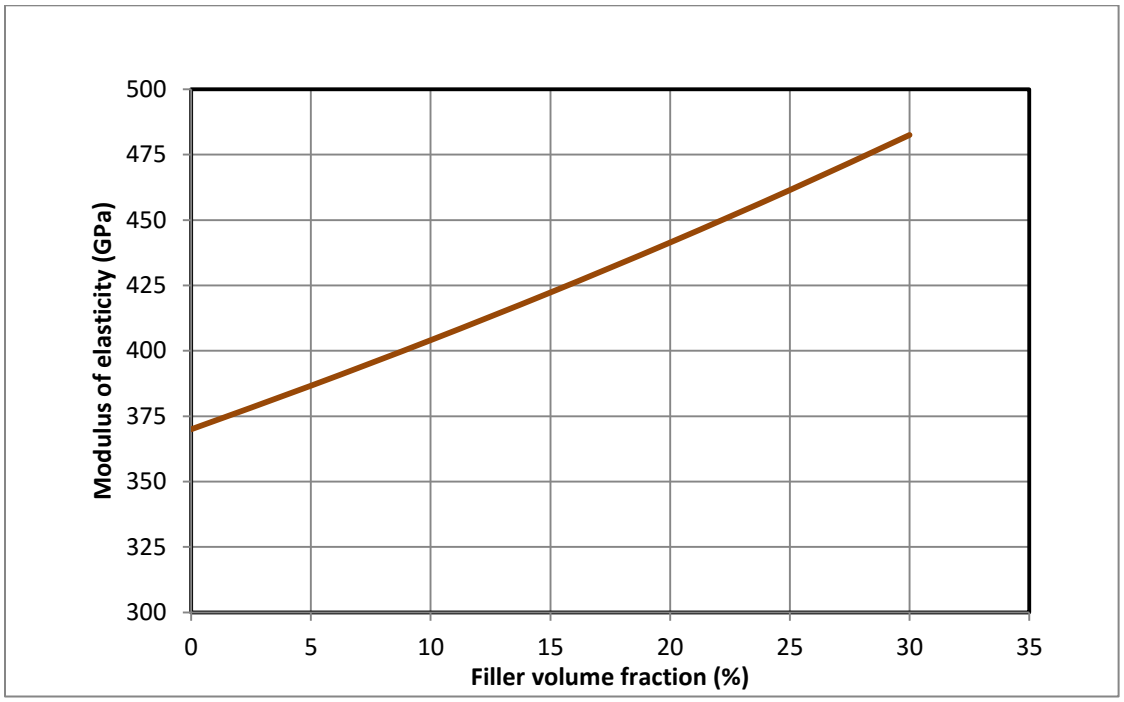


**Figure 3.16** Effective modulus of elasticity of alumina composite against diamond filler volume

Figure 3.17 is a plot of the effective electrical conductivity of the alumina/diamond composite as it varies with the volume fraction of diamond in alumina. The values from the plot which was also derived analytically shows a reduction in the electrical conductivity of the composite as the volume fraction of diamond increases inside the matrix. The plot is justifiable because diamond is a more electrical resistive material than alumina.

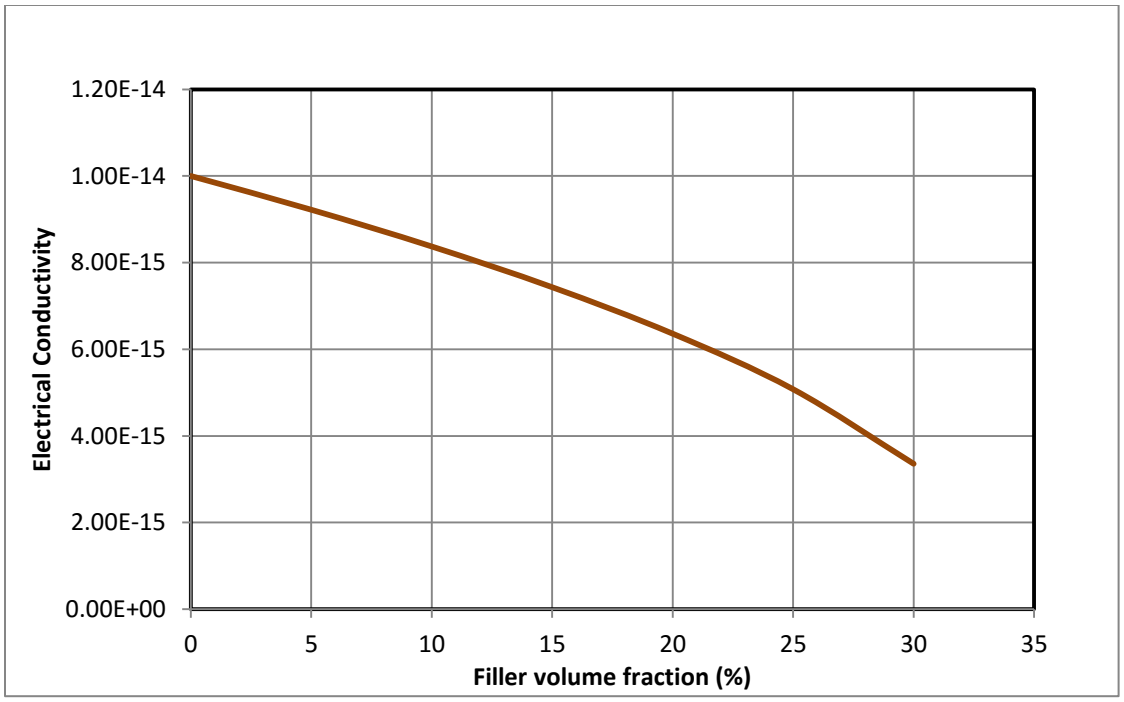


**Figure 3.17** Effective electrical conductivity of alumina composites against diamond filler volume

Figure 3.18 which show the density variation of the alumina composite as the volume fraction of filler increases. The values from the plot were derived using the rule of mixtures. It could be seen from the plot that the density of the composite decreased as the volume fraction of the filler increases, which could simply be associated with the fact that diamond has a lower density value than alumina.

From figure 3.16 it could be seen that the modulus of elasticity of alumina increases with increase in the volume fraction of diamond, but just at 10% volume fraction of diamond, the modulus of elasticity value of alumina was already at the limit of our target proposed property which is 400GPa. Also, at 10% volume fraction, we noticed a tangible improvement in our desired alumina properties and these gives a minimum benchmark for alumina property improvement. Beyond 10% all desired properties improved and

were within the target property range except the modulus of elasticity value which was out of range. A maximum benchmark was fixed at 15% volume fraction; at this filler volume fraction, all properties were within range except again modulus of elasticity which was a little bit of range at a value of 420GPa.

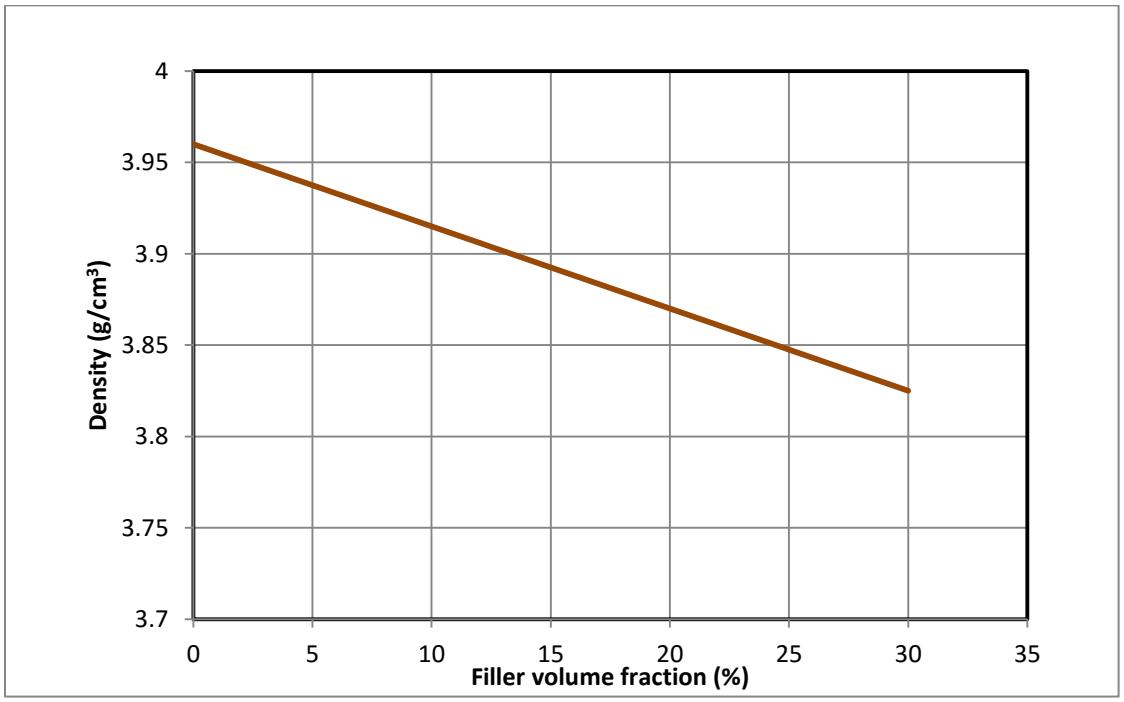


**Figure 3.18** Density of alumina composites against diamond filler volume

The effective thermal conductivity value of particulate composites is a direct function of the filler particle size. Below a certain filler particle size, thermal conductivity value would only decrease upon an increase in the filler volume fraction. Above this critical size, effective thermal conductivity of the composite will increase with increase in filler volume fraction which is clearly shown in figure 3.19. Below the critical filler particle

size, the surface area of the filler particle is too small to overcome the interfacial thermal resistant value between matrix and filler.

Figure 3.19 shows the variation of the effective thermal conductivity value of the alumina composite with diamond filler particle sizes for the two limiting volume fractions that were decided from figures 3.14 to 3.18. From figure 3.19, the minimum particle size which could enhance the thermal conductivity value of alumina is around 10µm. Below the 10µm particle size, thermal conductivity would only decrease and not increase. An average particle size of 80µm could be selected because at this value the effective thermal conductivity value of the resulting alumina composite would not improve significantly.

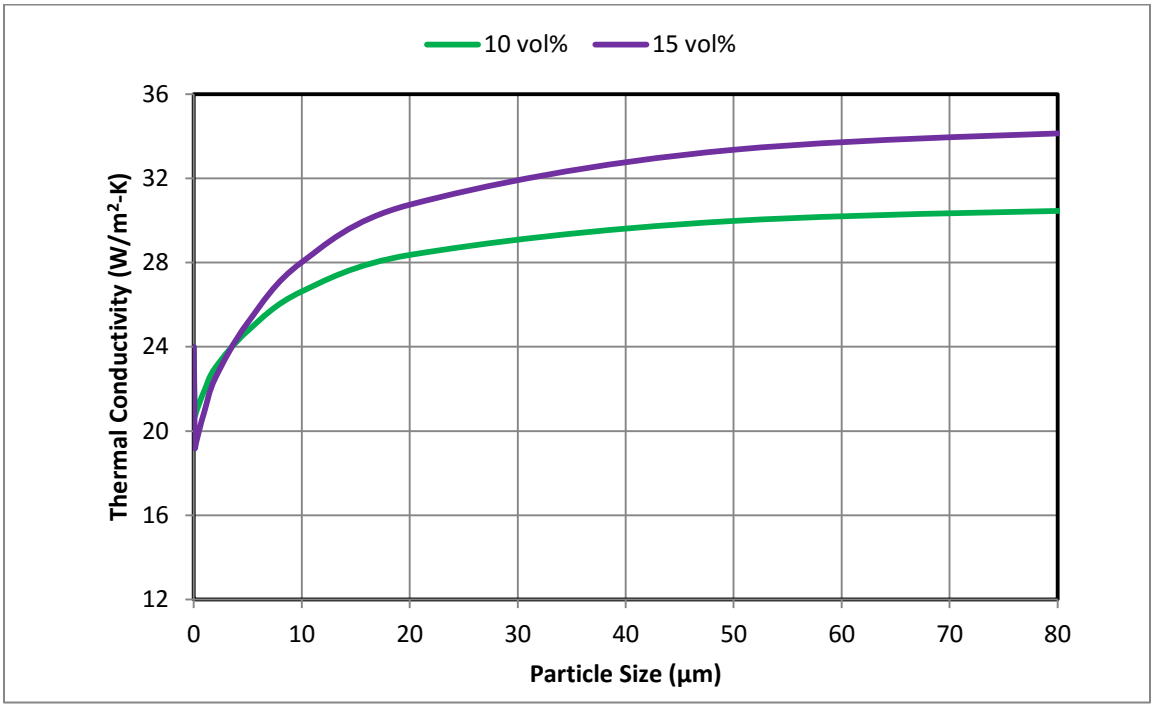


**Figure 3.19** Effective thermal conductivity of alumina composites against diamond filler particle sizes

The large diamond particle size is simply because alumina and diamond have a very large thermal interfacial resistance value between them as compared to alumina and the other two previously discussed filler materials (Chromium and Silicon carbide).

### 3.1.4 Summary of Selections

Tables 3.6 and 3.7 shows the summary of predicted properties values of an alumina composite with the three selected fillers which could improve the desirable properties of alumina. The two tables also show the suitable filler particle size and the range of filler volume fractions applicable for the application in DBC substrate. It was shown earlier that with these filler particle sizes and filler volume fractions, desirable properties of alumina like thermal conductivity and coefficient of thermal conductivity could be improved while retaining its core attributes like cost, positive environment impact and its ability to bond with copper. Table 3.6 shows the predicted property values of alumina when any the three fillers are added as reinforcement at selected volume fractions respectively while table 3.7 shows a comparison ratio of the predicted properties of the alumina composites with the properties of pure alumina.

**Table 3.6** Predicted properties of an alumina composite with suitable recommended fillers and filler attributes

| Proposed Filler Material | Volume Fraction (%) | Particle Size (µm) | | Effect on Thermal Conductivity ($W/m^2K$) | | Effect on CTE (µm/m-°C) | Effect on Modulus of Elasticity (GPa) | Effect on Electrical Conductivity (mho/cm) | Effect on Density ($g/cm^3$) |
|---|---|---|---|---|---|---|---|---|---|
| | | Min | Max | @ Min Particle size | @ Max Particle size | | | | |
| Chromium | 5 | 0.5 | 5 | 24.703 | 25.325 | 7.95 | 362.766 | 1.17E-14 | 4.122 |
| | 15 | 0.5 | 5 | 26.152 | 28.126 | 7.92 | 348.713 | 1.66E-14 | 4.445 |
| Silicon Carbide | 5 | 0.75 | 7 | 24.766 | 25.907 | 7.83 | 372.045 | 1.17E-14 | 3.917 |
| | 20 | 0.75 | 7 | 27.165 | 32.288 | 7.32 | 378.16 | 2.07E-14 | 3.788 |
| Diamond | 10 | 10 | 80 | 26.629 | 30.495 | 6.90 | 404.064 | 8.37E-15 | 3.915 |
| | 15 | 10 | 80 | 28.017 | 34.203 | 6.38 | 422.293 | 7.43E-15 | 3.893 |

**Table 3.7** Comparison of the predicted properties of an alumina composite with the properties of pure alumina

| Proposed Filler Material | Volume Fraction (%) | Particle Size (µm) | | $K_{eff}/K_{mat}$ | | $\alpha_{eff}/\alpha_{mat}$ | $E_{eff}/E_{mat}$ | $S_{eff}/S_{mat}$ | $\rho_{eff}/\rho_{mat}$ |
|---|---|---|---|---|---|---|---|---|---|
| | | Min | Max | @ Min Particle size | @ Max Particle size | | | | |
| Chromium | 5 | 0.5 | 5 | 1.03 | 1.06 | 0.99 | 0.98 | 1.17 | 1.05 |
| | 15 | 0.5 | 5 | 1.09 | 1,17 | 0.99 | 0.94 | 1.66 | 1.13 |
| Silicon Carbide | 5 | 0.75 | 7 | 1.03 | 1.08 | 0.97 | 1.00 | 1.17 | 0.99 |
| | 20 | 0.75 | 7 | 1.13 | 1.35 | 0.92 | 1.02 | 2.07 | 0.97 |
| Diamond | 10 | 10 | 80 | 1.11 | 1.27 | 0.86 | 1.09 | 0.84 | 0.99 |
| | 15 | 10 | 80 | 1.17 | 1.43 | 0.80 | 1.14 | 0.74 | 0.99 |

## 3.2 Chapter Summary

This chapter has provided:

- An approach to design material for certain applications
- The descriptions of numerical models used in estimating the effective properties of a particulate composite
- The results from the numerical models used in estimating the effective properties of a particulate filled composite

The next chapter would present the experimental route in developing the composite samples. Also the test procedures and results related the physical, mechanical and thermal properties of the developed material.

# CHAPTER 4

# MATERIAL DEVELOPMENT, TESTING AND CHARACTERIZATION

This chapter presents the experimental route in developing an alumina composite. It also presents measured property and tests results of the developed alumina composites reinforced with 20% volume fraction of silicon carbide filler from two different sources. The relative effects of the silicon carbide fillers in alumina have been discussed and compared with pure alumina. In addition, this chapter also presents scanning electron micrographs and XRD patterns which show some microstructural features and crystalline peaks of the materials under study.

## 4.1 Material Development

This section describes the method used in the processing and characterization of the composites under study. It also presents the details of the details of the test related to the physical, mechanical, microstructural and thermal characterization of the prepared particulate ceramic composites. For the composite development, silicon carbide fillers was selected based on its relative cost to alumina and it availability.

### 4.1.1 Composite Fabrication

The starting materials for the composite were alumina powder (matrix) and silicon carbide powder (fillers) with the silicon carbide sourced from two different supplies. The alpha alumina powder was supplied by Buehler while the silicon carbide powders were supplied by Buehler (Type I) and Alfa Aesar (Type II). Their average particle sizes are of 0.3 µm, 31 µm and 46µm respectively as summarized in table 4.1 below.

Figure 4.1 shows a schematic which summaries the flow of the material development route.

**Table 4.1** Alumina composite filled with 20% silicon carbide

| Matrix | Filler Type | Filler Average Particle Size (µm) |
|---|---|---|
| Alumina (0.3µm) | Silicon Carbide | NA |
| | | 31 |
| | | 46 |

The filler volume fraction of silicon carbide was selected at 20%. The filler was effectively dispersed into the alumina matrix via a mechanical planetary ball milling machine (as seen in figure 4.2) operating at a low speed of 150rpm for 1hr 30min. The ball miller was operated without the milling balls with the intentions of just mixing the two powders together and not crushing or reducing the size of the powder particles.

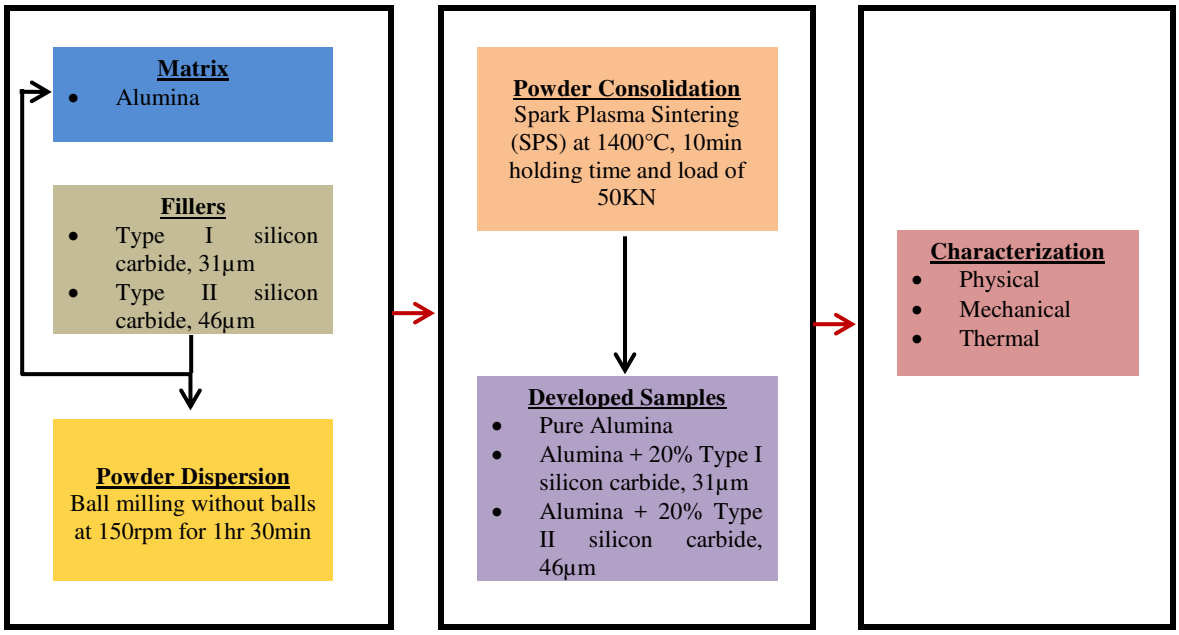


**Figure 4.1** Schematic showing the flow of the experimental material development

**Figure 4.2** Planetary ball milling machine, Pulverisette 5 from Fritsch

The powder mixture was later wrapped in a graphite sheet and placed tightly inside a 30mm cylindrical graphite die. The die was placed inside the chamber of an automatic Spark Plasma Sintering (SPS) equipment from FCT, Germany (as seen in figure 4.3). The sintering temperature was set to 1400°C, heat rate of 100°C/min, a holding time of 10min and a pressure of 50MPa.

**Figure 4.3** Spark Plasma Sintering (SPS) equipment from FCT, Germany

While the powder mixture charged into the graphite die is placed inside the chamber of the SPS, current is passed, heating is performed and a mechanical axial load is applied at the same time. The graphite dies were used to prepare cylindrically shaped samples while the graphite sheets are meant to minimize friction between the die walls and the powder mixture, and also for easy ejection of samples after sintering. The sintering temperature was measured and monitored using a pyrometer placed at the bottom of a central hole in

the upper punch. The pulse duration and pause time, as well as the heating rate, were fixed throughout all phases of the experiment.

### 4.1.2 Physical and Mechanical Characterization

#### A. Density and Porosity

The density of the composite depends greatly on the relative proportion of the matrix and filler materials; it is one of the important factors for the determination of some other properties of the composite. The theoretical density ($\rho_{th}$) of the composite in terms of the density and volume fraction of the matrix and filler constituent materials can easily be determined by using the rule of mixtures as shown in Eq. (4.1).

$$\rho_{th} = (\rho_m * v_m) + (\rho_f * v_f) \tag{4.1}$$

Where

$$v_m + v_f = 1 \tag{4.2}$$

Also, where $\rho$ and $v$ represent density and volume fraction respectively, and where the scripts $m$ and $f$ signifies matrix and filler materials respectively. The formula above is only applicable to composites with single fillers and not composites with multiple fillers. The actual or measured density ($\rho_{ac}$) of the composite can be determined experimentally by applying the Archimedes principle or water displacement method (ASTM D792-91). This method takes into consideration the weight of the composite samples in air and in water.

Percentage porosity ($\%P$) or the volume fraction of voids ($v_v$) of the composite is calculated by using either of the following Eq. (4.3) and (4.4).

$$\%P = \left(\frac{\rho_{th}-\rho_{ac}}{\rho_{th}}\right) * 100 \tag{4.3}$$

$$v_v = (\rho_{th} - \rho_{ac})/\rho_{th} \tag{4.4}$$

**B. Scanning Electron Microscopy**

The microstructural analysis and features of the particulate composites were examined by a scanning electron microscope. The specimens were mounted onto a sample mounting polymer where the surface of the specimen was well polished with no scratches. In order to improve electron penetration and better micrographs, the specimens were coated with a thin film of gold which was achieved by a vacuum evaporation process. The scanning electronic microscope is as seen in figure 4.4.

**C. X -ray Diffractometer**

The XRD analysis of the resulting composites at the cross-section of the samples was carried out on the samples using a Rigaku desktop x-ray diffractometer model "Miniflex II" (as seen in figure 4.5) with copper radiation having wavelength of 1.5418A.

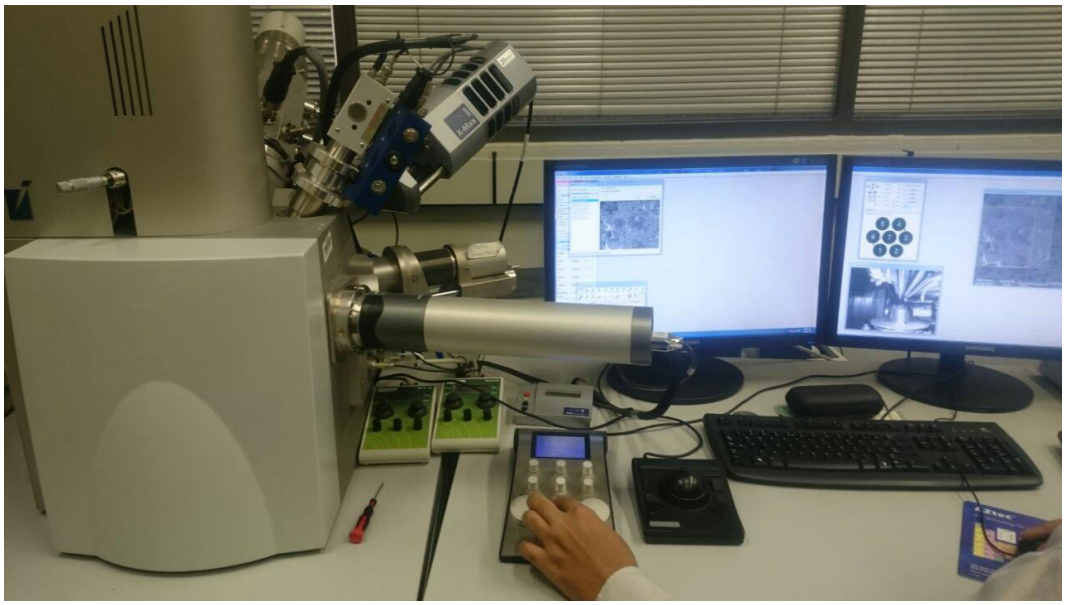

**Figure 4.4** Scanning Electron Microscope

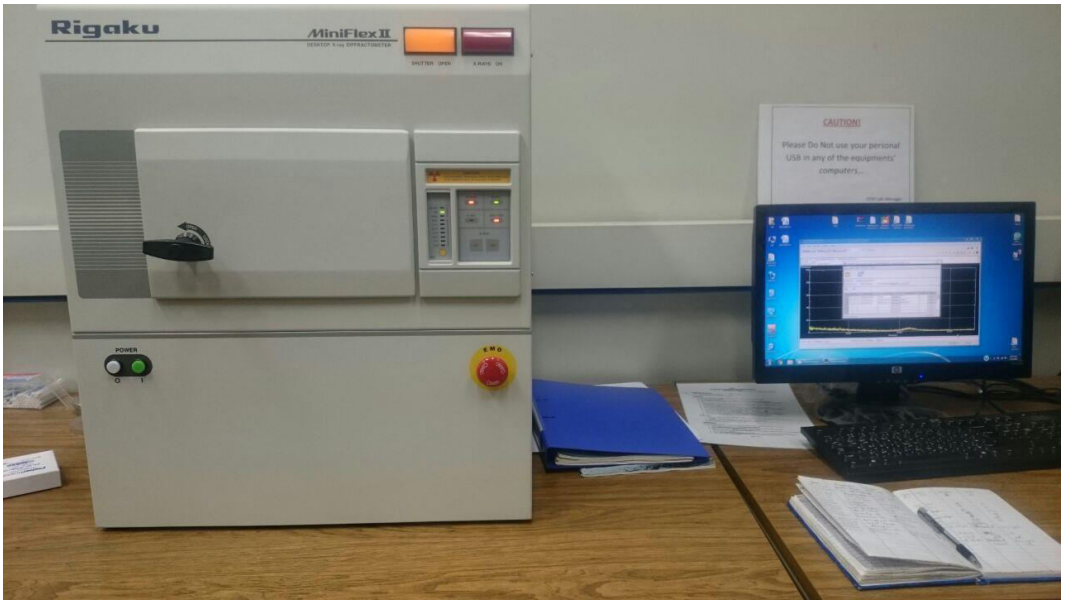


**Figure 4.5** Rigaku - Miniflex II Desktop X-ray diffractometer

### D. Micro-Hardness and Modulus of Elasticity

The micro-hardness and modulus of elasticity of the sample materials were measured simultaneously using a CSM instruments Micro Combi Tester as seen in figure 4.6.

A diamond indenter in the form of a pyramid normal to the sample surface is driven down into the sample by applying an increasing load to a preset value, after which the load is then gradually decreased until partial or complete relaxation of the material occurs. The indentation hardness is then defined as the mean contact pressure of the indenter on the sample given by Eq. (4.5).

$$H_{IT} = \frac{F_{max}}{A_r} \tag{4.5}$$

Where $H_{IT}$ is the indentation hardness, $F_{max}$ is the maximum load applied on the surface of the sample, and $A_r$ is the projected contact area at that load.

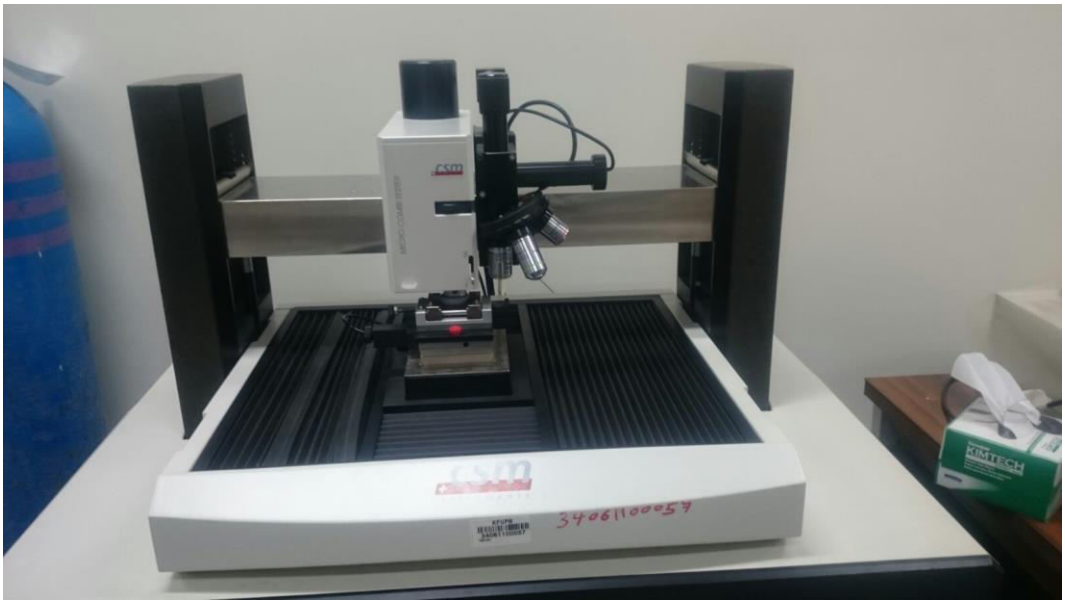


**Figure 4.6** Micro Combi Tester from CSM Instruments

The modulus of elasticity of the material or indentation modulus is usually calculated automatically by the equipment using Eq. (4.6). It uses the slope of the tangent of the unloading curve either by using a linear fit to the initial loading data or a power law fit.

$$E_{IT} = \frac{1-{v_s}^2}{\frac{1}{E_r}-\frac{{v_i}^2}{E_i}} \tag{4.6}$$

The indentation modulus of the material is given by $E_{IT}$. $v_s$ is the poison's ratio of the sample. $E_i$ and $v_i$ are the elastic modulus (1141GPa) and poison's ratio (0.07) of the diamond indenter respectively, and $E_r$ the reduced modulus which can be calculated using data from the indentation using Eq. (4.7).

$$E_r = \frac{\sqrt{\pi}\cdot S}{2\cdot b\cdot\sqrt{A_P(h_c)}} \tag{4.7}$$

Where $S$ is the stiffness or the slope of the unloading curve is, $b$ is the compliance constant, $h_c$ is the contact depth and $A_P$ is the project area contact.

### 4.1.3 Thermal and Electrical Characterization

#### A. Thermal Conductivity

The C-Therm TCI Thermal Conductivity Analyzer as seen in figure 4.7 can be used to measure the thermal conductivity of various types of materials which include but not limited to polymers, glasses, rubber, ceramics and metals. This material could exist as either solid, powder or liquid states. In this present work, the instrument was used to analyze and measure the thermal conductivity of our resulting composites at room temperature.

The equipment operates based on the Modified Transient Plane Source (MTPS) technique which uses a one-sided interfacial heat reflectance sensor that applies a momentary constant heat source to samples, and thus the thermal conductivity and effusivity of the sample are measured directly.

In its operation, a known current is applied to the sensor's spiral heating element which results in the rise of the interfacial temperature between the sensor and the sample. This raise in temperature induces a change in the voltage drop of the sensor's element, and the rate increase in the sensor voltage is used to determine the thermos-physical properties of the sample. Thermos-physical properties are usually proportional to the rate of increase in the sensor's voltage.


**Figure 4.7** C-Therm TCI Thermal Conductivity Analyzer

## B. Coefficient of Thermal Expansion

The coefficient of thermal expansion (CTE) of a material can be described as the strain induced in the material per unit rise in temperature. In this present work, the CTE of the resulting composites were measured using a METTLE TOLEDO Thermal mechanical analyzer (TMA/SDTA 1 LF/1100) as seen in figure 4.8. A thermal mechanical analyzer (TMA) is used to measure the dimensional changes of a material as a function of temperature. TMA can be used to evaluate the coefficient of thermal expansion of the material as well as softening, crystallization and solid-solid transitions.

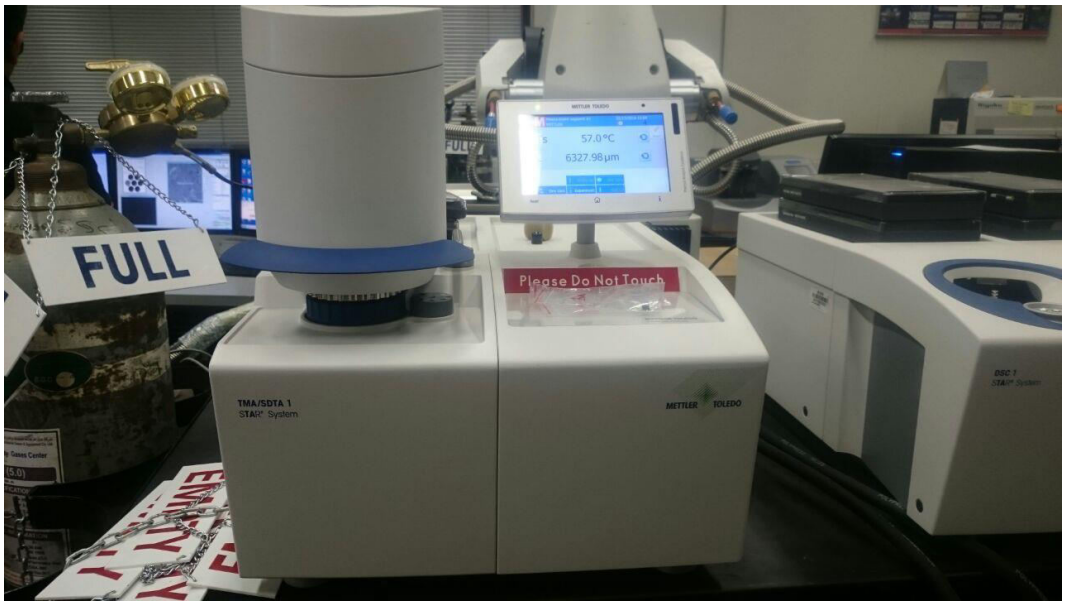


**Figure 4.8** METTLE TOLEDO, Thermal mechanical analyzer TMA/SDTA 1 LF/1100

## 4.2 Results and Discussion; Physical and Mechanical Characteristics

### 4.2.1 Density and Porosity

The density of a composite depends on the relative proportion of the matrix and filler materials and the amount of porosity in the composite. The volume fraction, theoretical density, measured densities and porosity in the sintered pure alumina and alumina composite samples are presented in table 4.2 below. It can be seen that the theoretically calculated density values of the composites are not equal but very close to the experimentally measured values. This shows that good densification was achieved during the sintering process and the porosity fraction is less than 1% for all sintered samples.

**Table 4.2** Measure and theoretical densities of the developed materials

| Matrix | Filler Type | Filler Volume Fraction (%) | Measured Density ($g/cm^3$) | Theoretical Density ($g/cm^3$) | Porosity (%) |
|---|---|---|---|---|---|
| Alumina | Silicon Carbide | 0 | 3.979 | 3.990 | 0.284 |
| | | 20 (31µm, Type I) | 3.814 | 3.834 | 0.519 |
| | | 20 (46µm Type II) | 3.816 | 3.834 | 0.465 |

### 4.2.2 Micro-Structural Characterization

It is a known fact that the properties of composites are strongly dependent on the interaction of the matrix and filler materials. To evaluate the interaction between the matrix and filler materials, the microstructure of the composite as well as the dispersion of the fillers within the matrix of the sintered composite samples were observed under a scanning electron microscope (SEM).

Figure 4.9 shows the scanning electron microscopy images of pure alumina sample taken along the cross-section of the sample. Due to the SPS sintering parameters and the particle size of the alumina powder, the individual grains were not visible in the micrographs of the sample. The images also reconfirm the low porosity fraction as no pores are visible across the surface of the sample.

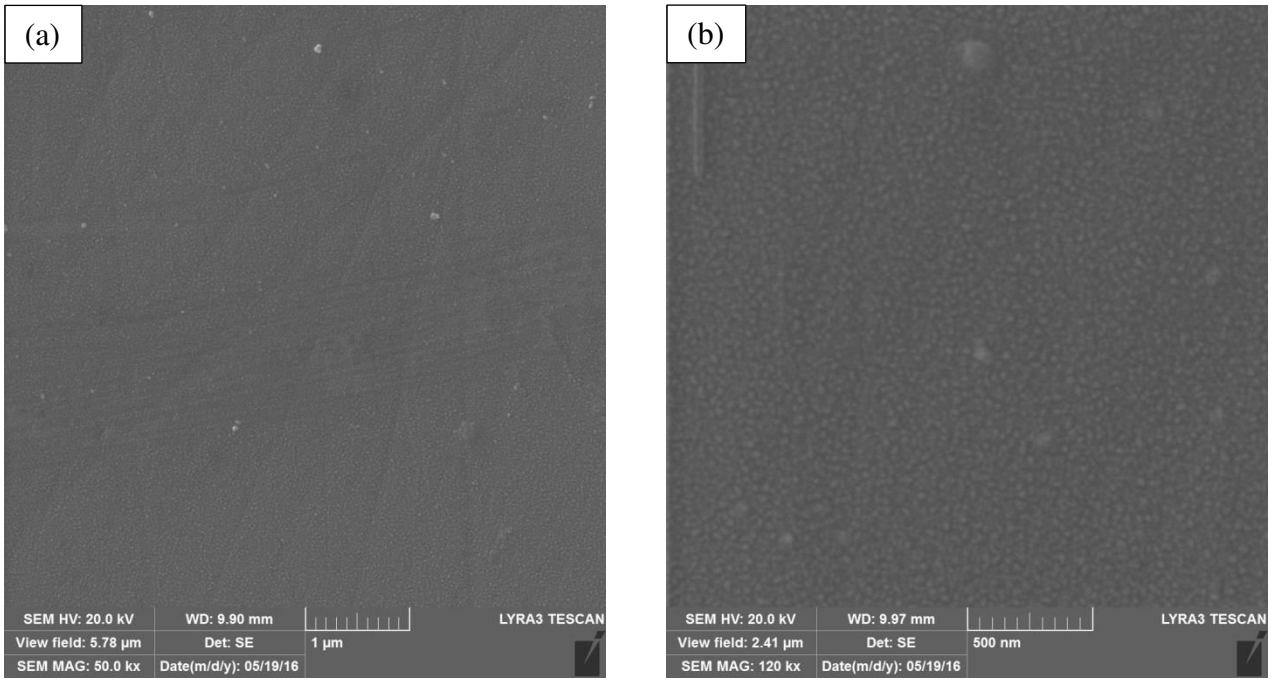


**Figure 4.9** SEM images of pure sintered 0.3µm alumina at different magnifications

Figures 4.10 and 4.11 show the SEM images of the two composite materials. As seen in figure 4.9, alumina appeared blackish in color which means the blackish parts of figures 4.10 and 4.11 is alumina while the whitish gray parts are silicon carbide. An area proportionality of the image with different color codes shows that the SiC fraction is about 20% which is the volume fraction of alumina used.

To further confirm the presence of silicon carbide and alumina in the developed materials, an energy-dispersive X-ray spectroscopy (EDX) analysis was carried out. The results further confirmed the presence of the constitutive elements that makes up the matrix and filler materials. Figure 4.12 and 4.13 shows the results from the EDX analysis.

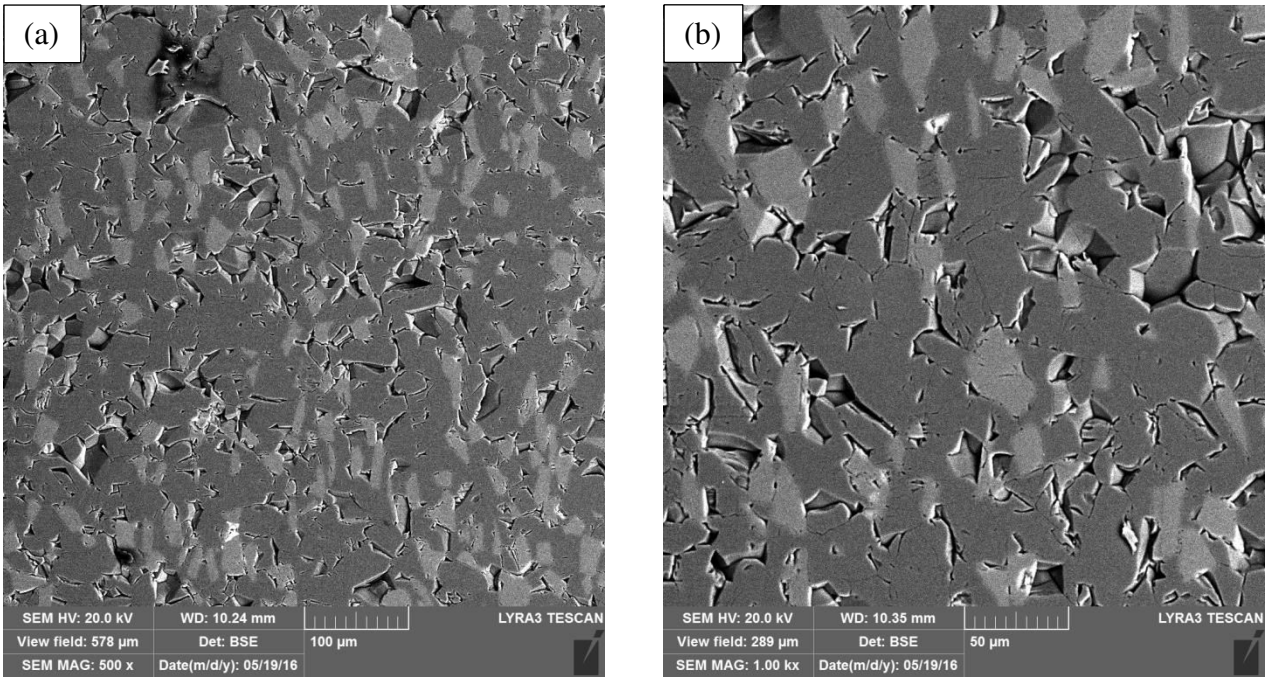


**Figure 4.10** SEM images of alumina composite with 20% silicon carbide (Type I) at different locations

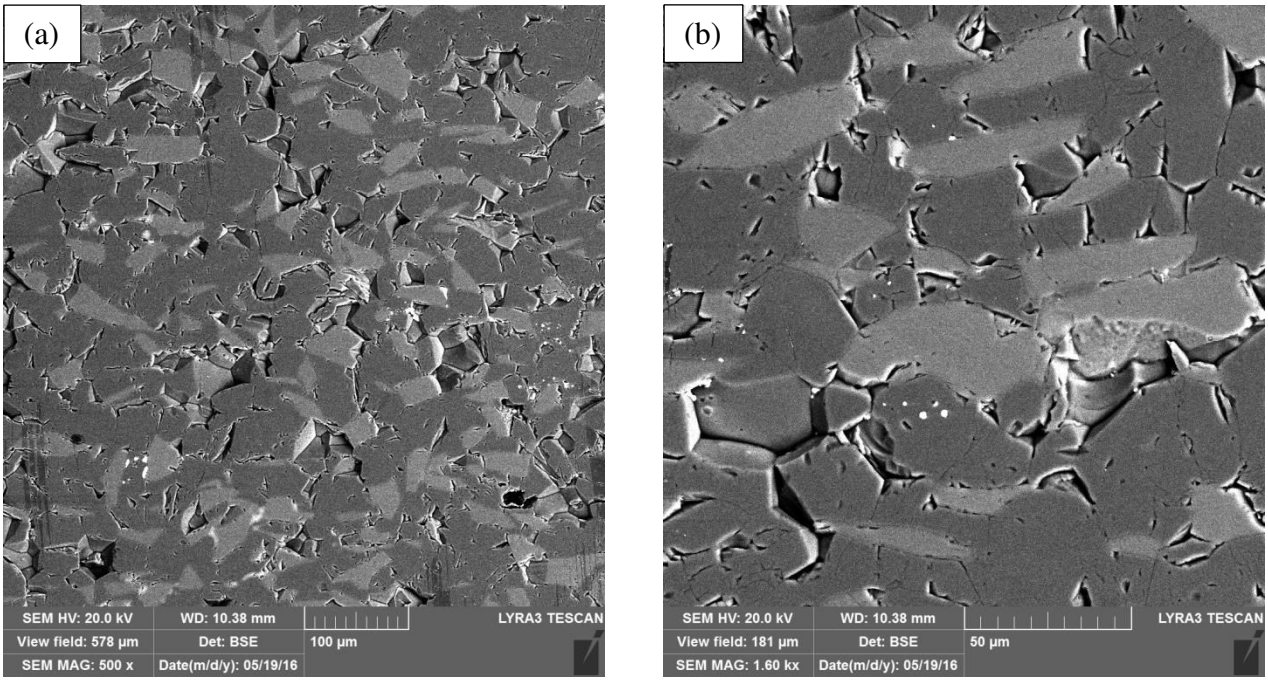


**Figure 4.11** SEM images of alumina composite with 20% silicon carbide (Type II) at different magnifications

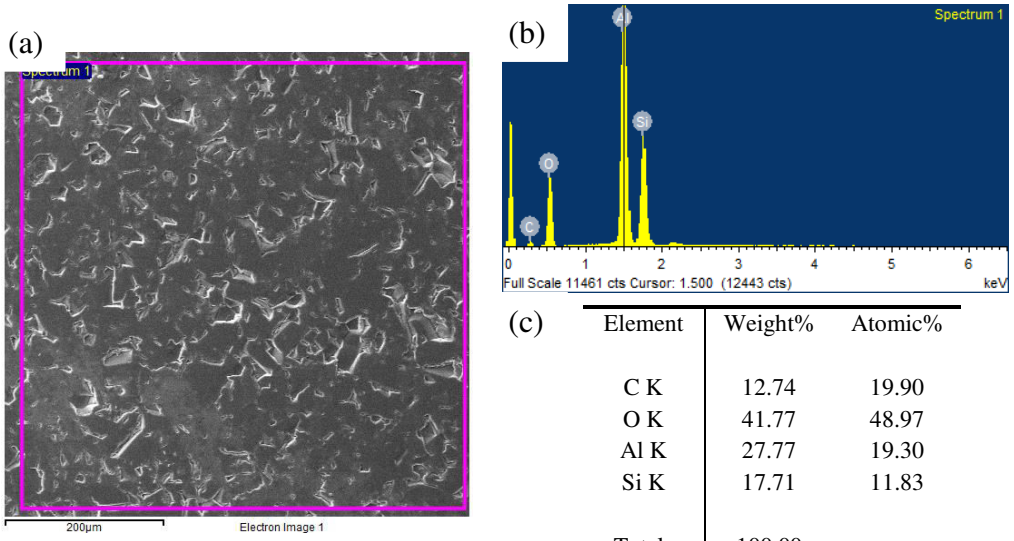


(c)

| Element | Weight% | Atomic% |
|---|---|---|
| C K | 12.74 | 19.90 |
| O K | 41.77 | 48.97 |
| Al K | 27.77 | 19.30 |
| Si K | 17.71 | 11.83 |
| Totals | 100.00 | |

**Figure 4.12** EDX analysis for alumina composite with 20% silicon carbide (Type I)

(a)

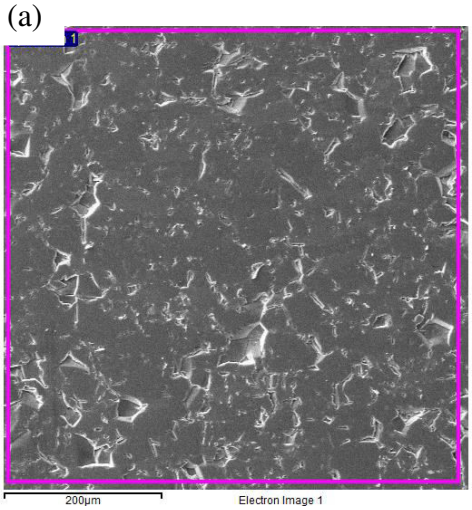


(b)

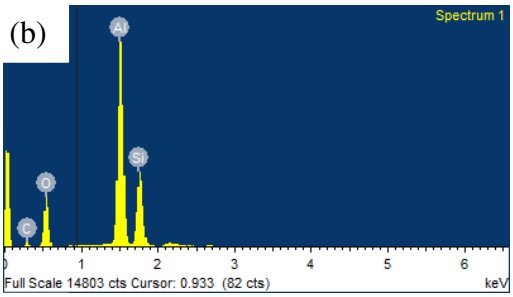


(c)

| Element | Weight% | Atomic% |
|---|---|---|
| C K | 12.88 | 20.12 |
| O K | 41.31 | 48.46 |
| Al K | 29.34 | 20.41 |
| Si K | 16.48 | 11.01 |
| Totals | 100.00 | |

**Figure 4.13** EDX analysis for alumina composite with 20% silicon carbide (Type II)

### 4.2.3 XRD Patterns

The XRD patterns in figures 4.14, 4.15 and 4.16 shows the peaks of the developed pure alumna and the alumina/silicon carbide composite samples. The XRD patterns of all developed samples when matched with the XRD patterns available in the database. The obtained lattice spacing (d-spacing) and diffraction angle (2θ) values were also compared with the standard values for $Al_2O_3$, SiC and any other possible phases between $Al_2O_3$ and SiC in the database. However, the only phases identified were $Al_2O_3$ and SiC. This further confirms the presence of the constituent materials used in developing the composites. It also shows that $Al_2O_3$ and SiC have not chemically reacted with each other.

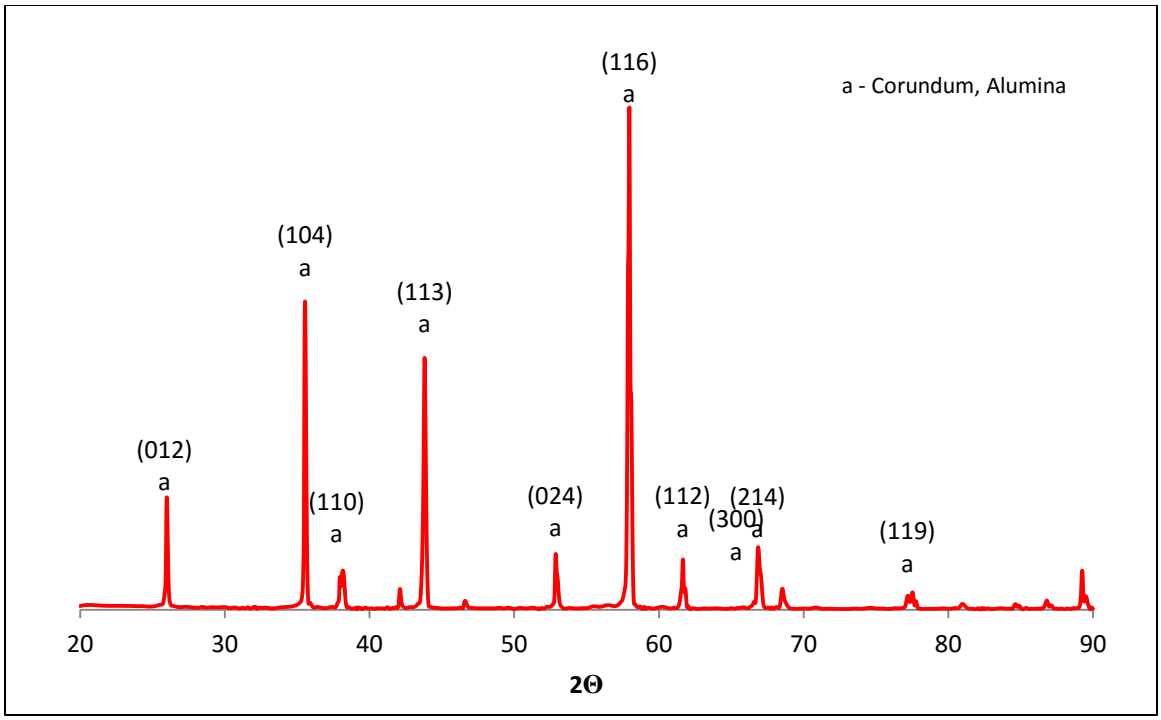


**Figure 4.14** XRD pattern of pure sintered alumina

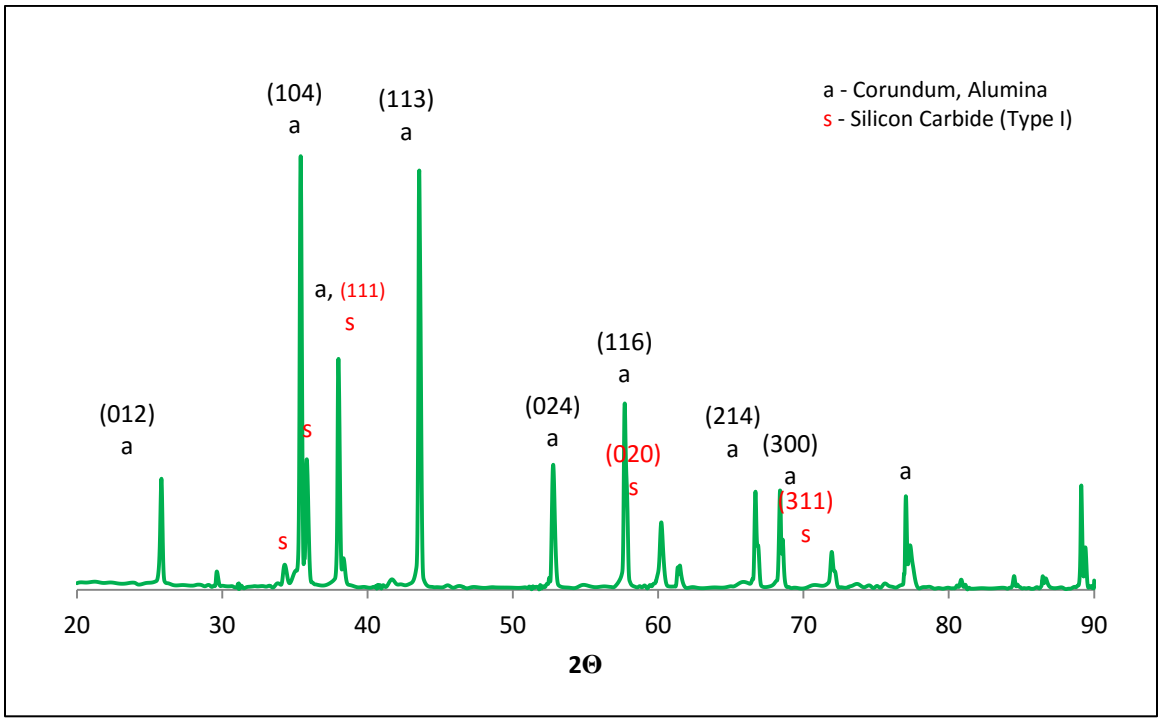


**Figure 4.15** XRD pattern of alumina composite with 20% silicon carbide (Type I)

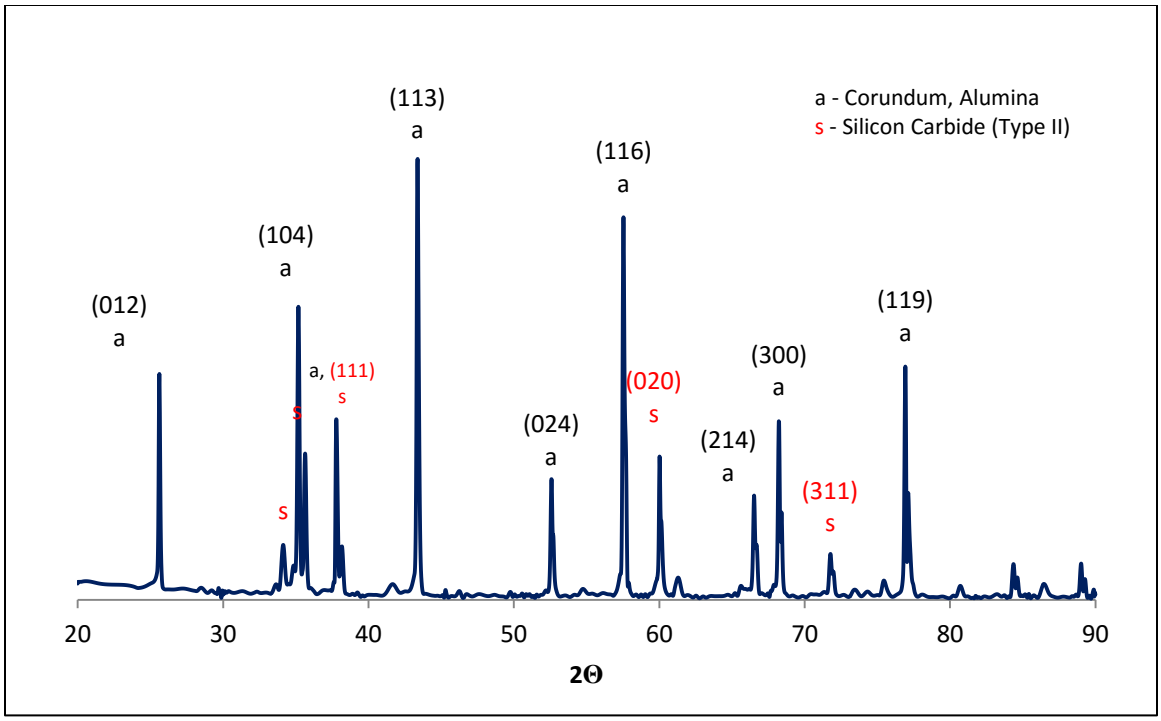


**Figure 4.16** XRD pattern of alumina composite with 20% silicon carbide (Type II)

### 4.2.4 Micro Hardness and Modulus of Elasticity

Hardness is usually considered as one of the most importance characteristic features of a composite as it indicates the ability of a material to resist localized deformation when a known load is applied. In this present work, the microhardness of the developed samples was measured using a load of 500 and 2000gf. The microhardness test was conducted multiple times at multiple locations along the cross-sectional area at the middle interface of the sample and the mean and standard deviation values were calculated and recorded. The test results are presented in table 4.3 below. The results show that the hardness of the two developed composites reduced as compared to the pure sintered alumina sample. This could be attributed with poor interfacial bonding between the matrix and filler

material as seen in the SEM images of figures 4.10 and 4.11. Surface openings could be seen at the interface between the matrix and filler material.

**Table 4.3** Micro - Hardness values of developed materials

| Matrix | Filler Type | Filler Volume Fraction (%) | Location Within Sample | Vickers Micro – Hardness | | | |
|---|---|---|---|---|---|---|---|
| | | | | 500gf | | 2000gf | |
| | | | | Average | Standard Deviation | Average | Standard Deviation |
| Alumina | Silicon Carbide | 0 | Matrix | 1457.26 | 339.32 | 1536.22 | 200.93 |
| | | 20 (31µm, Type I) | Interface | 1003.76 | 190.50 | 1019.69 | 187.02 |
| | | | Filler | 1836.66 | 41.52 | 1895.21 | 41.28 |
| | | 20 (46µm Type II) | Interface | 917.80 | 87.26 | 859.86 | 87.79 |
| | | | Filler | 2203.33 | 394.47 | 2249.75 | 460.11 |

The modulus of elasticity values of the sintered samples were also obtained via micro-indentation experiment. The results are presented in table 4.4 and figure 4.17. The results show that the modulus of elasticity of the two sintered composites reduced as compared to the pure sintered alumina. This could also be attributed with the poor interfacial bond between the matrix and filler material. Still this method is not all satisfactory in determining the modulus of elasticity of composite samples, its more suitable for bulk samples. Observing and comparing the SEM images in figure 4.9 to 4.11 of the developed samples, the images kind of explains the drop in the two property values as more surface openings or porosity between the matrix and filler particles could be seen.

These surface openings might be associated with because the fact that alumina has a lower sintering temperature than silicon carbide.

**Table 4.4** Experimentally measured and estimated effective modulus of elasticity values of developed materials

| Matrix | Filler Type | Filler Volume Fraction (%) | Effective Modulus of Elasticity (MPa) | | $E_{eff}/E_{mat}$ | |
|---|---|---|---|---|---|---|
| | | | Experiment | Estimated | Experiment | Estimated |
| Alumina | Silicon Carbide | 0 | 265.85 | | 1 | |
| | | 20 (31µm, Type I) | 172.59 | 238.12 | 0.64 | 0.89 |
| | | 20 (46µm Type II) | 172.79 | 238.12 | 0.65 | 0.89 |

Table 4.4 and figure 4.17 also presents the numerically estimated effective modulus of elasticity values of the samples. The effective modulus of elasticity value derived from the pure sintered alumina sample was used to re-calculate and re-estimate the effective modulus of elasticity values of the developed composites numerically. The discrepancy between the experimental and numerical values could be attributed to the powder consolidation technique used in developing the composite samples and some certain

assumptions that were made in order to simplify the numerical analysis. Some of the factors and assumptions include;

- Uneven sintering temperature of alumina and silicon carbide which the numerical model does not take into consideration.
- Assumed perfect spherical shape of the filler material.
- Assumed perfect filler distribution within the matrix.

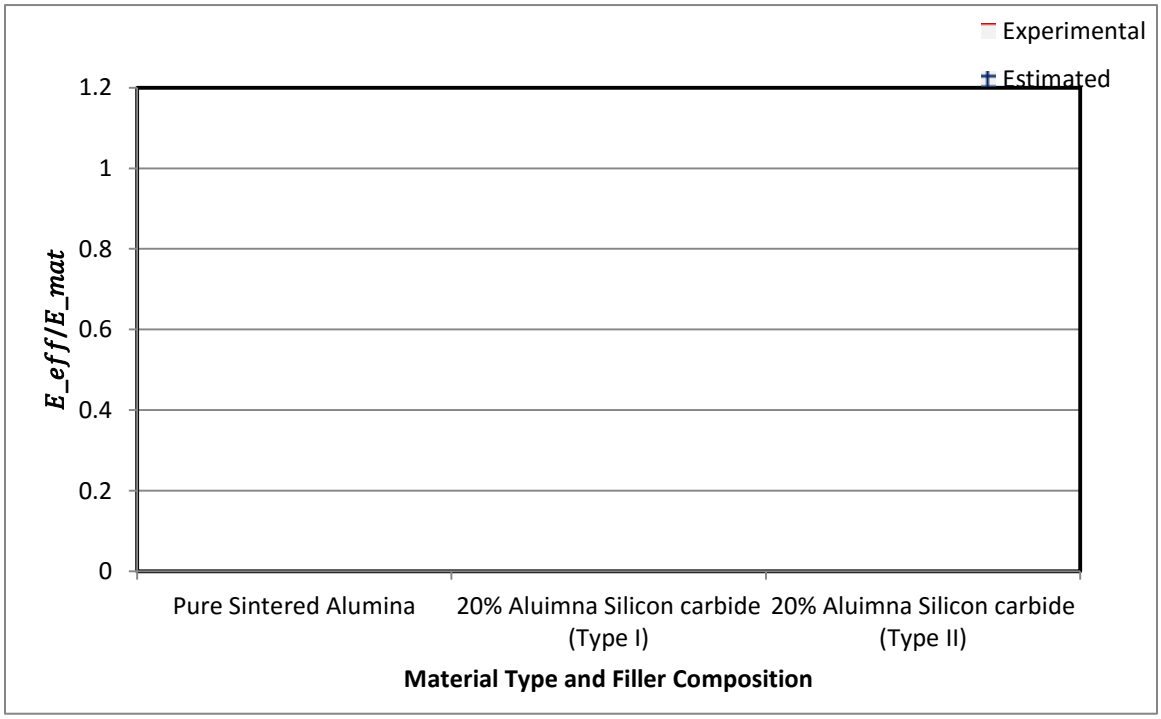


**Figure 4.17** Comparison of the effective modulus of elasticity values of the developed materials

The optical images shown in figures 4.17 to 4.19 were obtained from the micro-hardness tester's optical microscope; it shows the optical images of the samples before and after an

indentation for the three developed samples. Alumina could be seen to appear in a gray/black color under the microscope, and silicon carbide appearing whitish with an even distribution within the alumina matrix.

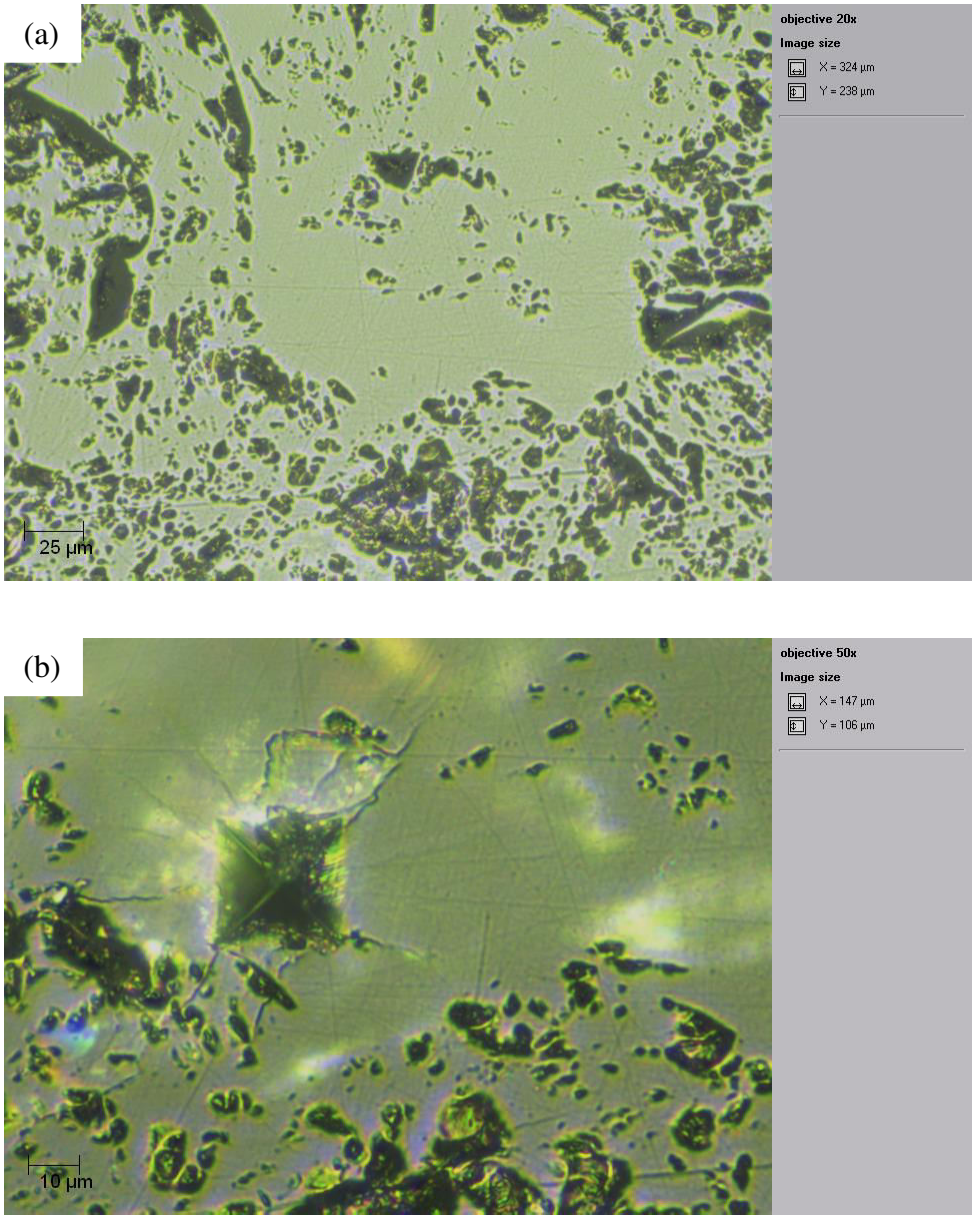


**Figure 4.18** Optical images of pure sintered alumina before and after the indentation

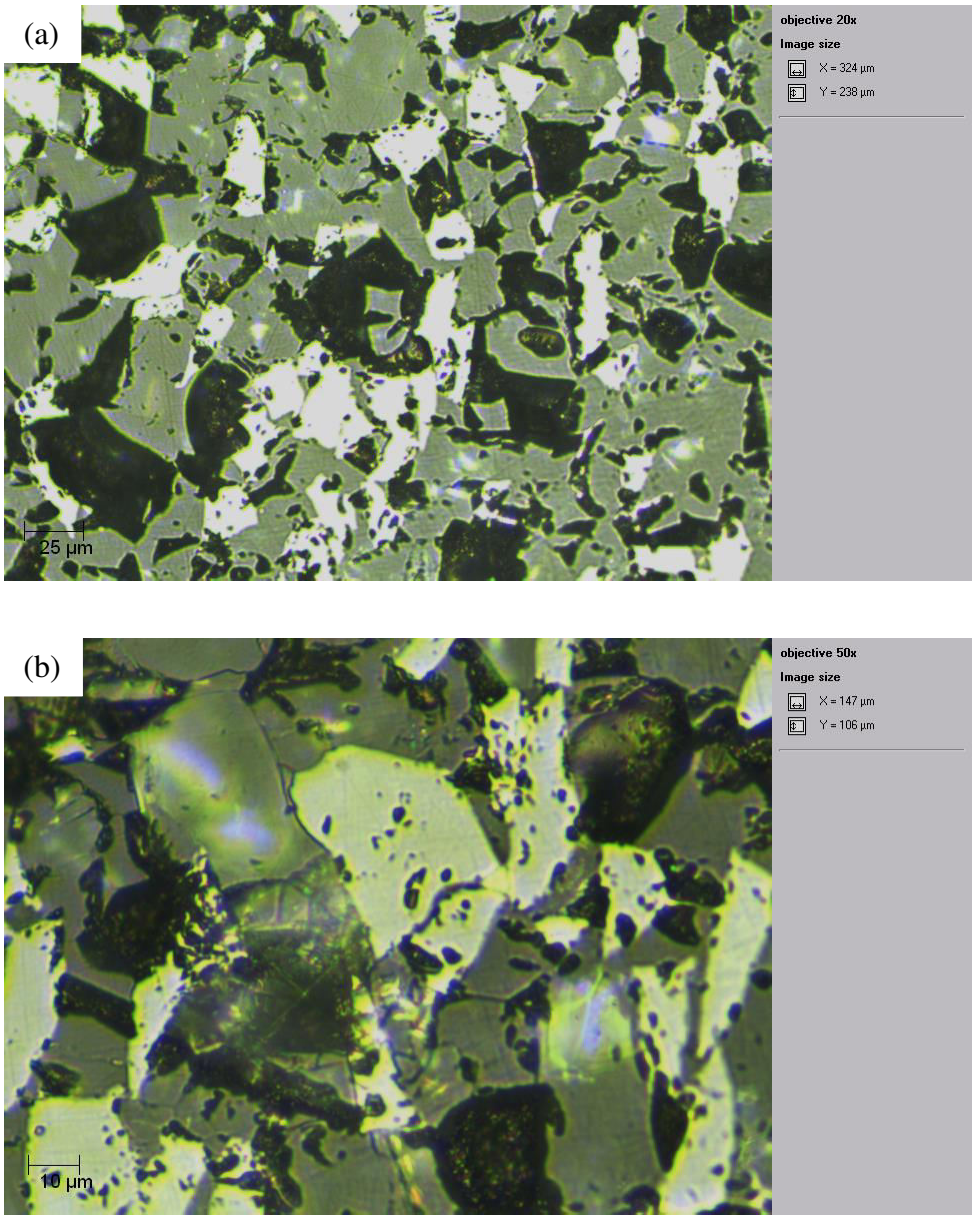


**Figure 4.19** Optical images of alumina composite with 20% silicon carbide (Type I) before and after the indentation

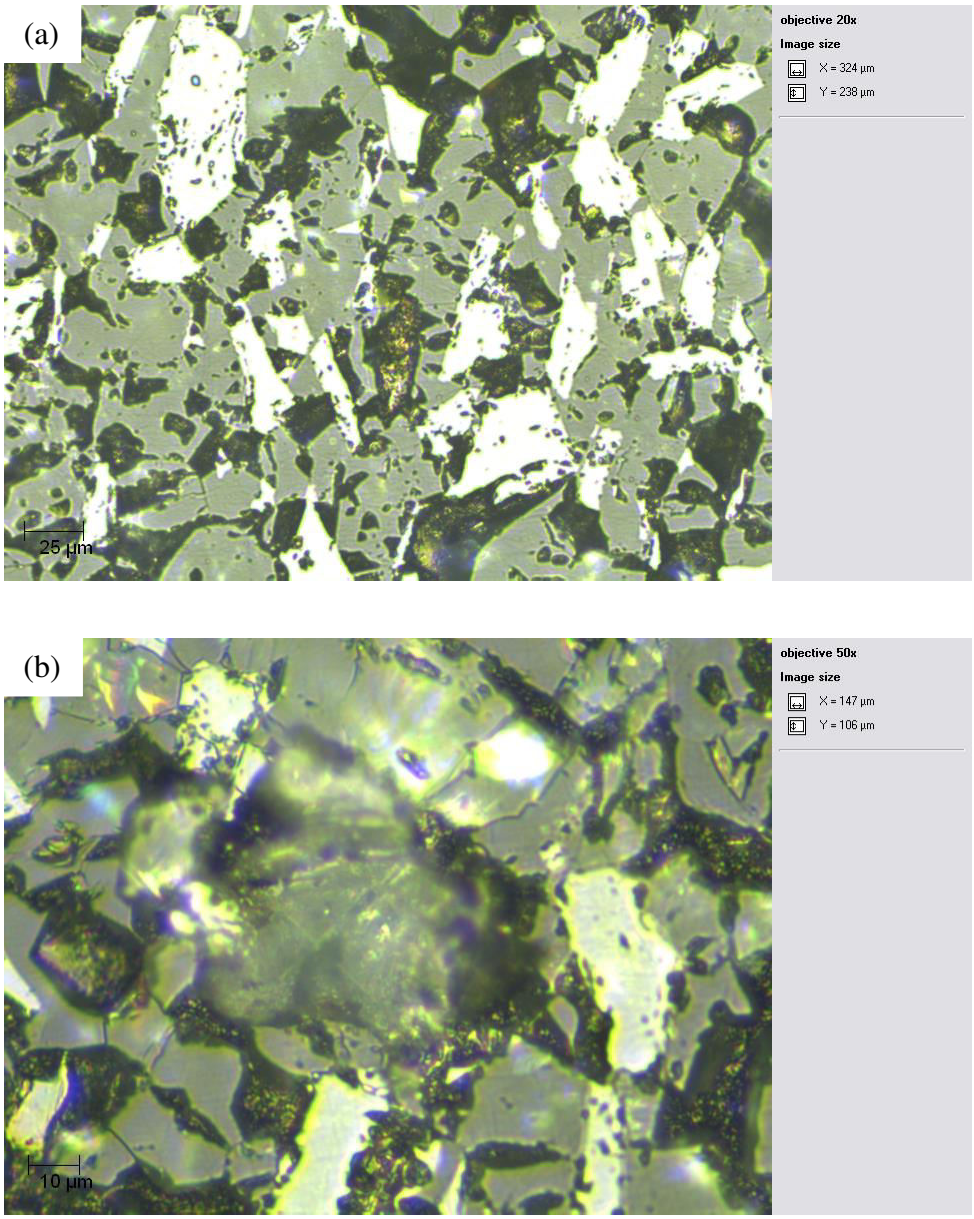


**Figure 4.20** Optical images of alumina composite with 20% silicon carbide (Type II) before and after the indentation

## 4.3 Results and Discussion; Thermal Characteristics

### 4.3.1 Effective Thermal Conductivity

The effective thermal conductivity values of the developed materials were evaluated theoretically and experimentally. Although the theoretical thermal effective values of the composites were evaluated in the previously chapter, the values were re-evaluated here as the thermal conductivity value of $24W/m^2$-K for the pure matrix material (as obtained from literature) used in the previous chapter was very different from the one measured experimentally.

The CTI thermal conductivity analyzer was used to measure the thermal conductivity values of the developed samples (sintered pure alumina and alumina composite samples). The figure 4.20 and table 4.5 below presents the results of the experimental measurements and numerically estimated effective thermal conductivity values. As mentioned earlier, the experimentally measured thermal conductivity value of pure sintered alumina sample was used to re-calculate and estimate the effective thermal conductivities of the sintered composites numerically.

The discrepancy between the experimental and numerical effective thermal conductivity values could be attributed to certain assumptions that were made in order to simplify the numerical analysis, some of the assumptions made include;

- Perfect spherical shape of the filler material,
- Perfect particle sizes distribution of the filler material,
- Perfect filler distribution within the matrix

In addition, the thermal interface resistance between the matrix and the filler inclusion was taken from literature. The interface resistance is highly dependent on the interfacial characteristics and can vary greatly for same material from different sources and with process parameters.

It can be seen that the numerically calculated effective thermal conductivity values of the developed composites are in fairly good agreement with the experimentally measured effective thermal conductivity values. This validates the accuracy of the numerical model used in the current work. The numerical model only slightly overestimates the effective thermal conductivity values of composites, but it still gives a good estimate of the values.

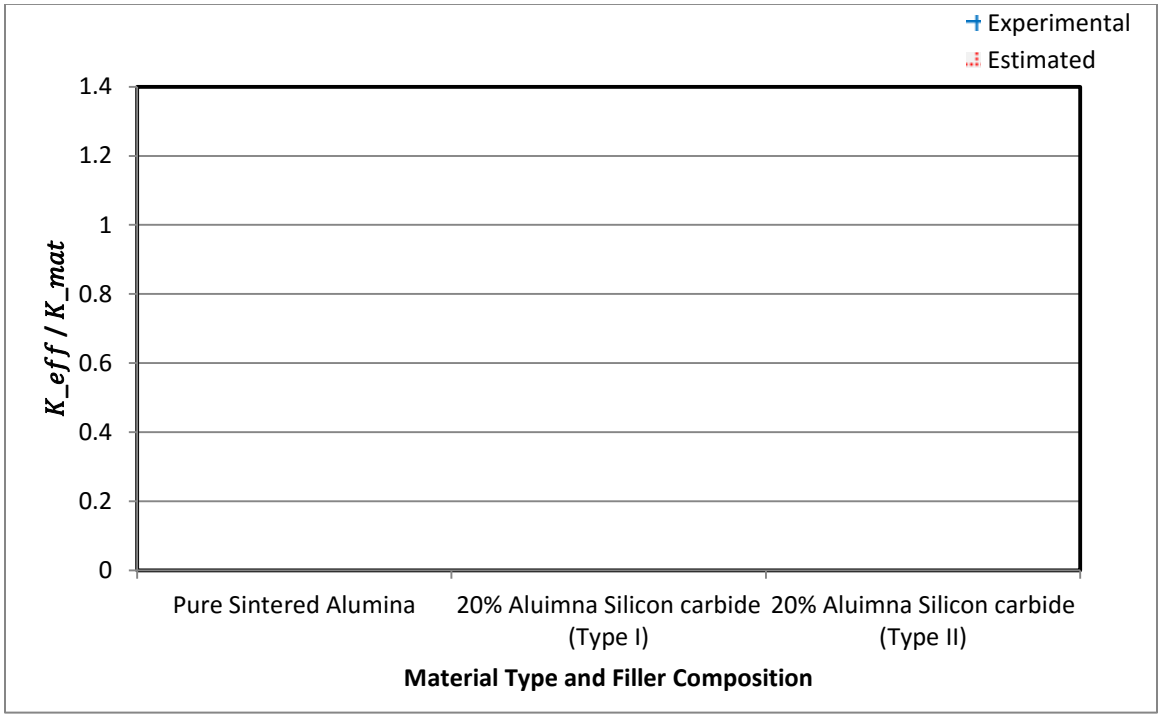


**Figure 4.21** Comparison of the effective thermal conductivity values of the developed materials

**Table 4.5** Experimentally measured and estimated effective thermal conductivity values of developed materials

| Matrix | Filler Type | Filler Volume Fraction (%) | Effective Thermal Conductivity ($W/m^2 K$) | | $K_{eff}/K_{mat}$ | |
|---|---|---|---|---|---|---|
| | | | Experiment | Estimated | Experiment | Estimated |
| Alumina | Silicon Carbide | 0 | 33.03 | | 1 | |
| | | 20 (31µm, Type I) | 38.31 | 42.53 | 1.12 | 1.28 |
| | | 20 (46µm Type II) | 37.03 | 42.67 | 1.16 | 1.29 |

### 4.3.2 Effective Coefficient of Thermal Expansion (CTE)

The Mettle Toledo thermal mechanical analyzer (TMA) was used to evaluate the effective coefficient of thermal expansion values of the developed samples (sintered pure alumina and alumina composite samples).

Figure 4.21 and table 4.6 present the results of the CTE experimental measurements along with the numerically estimated CTE values. The effective coefficient of thermal expansion value derived from the pure sintered alumina sample was also used to re-estimate the effective coefficient of thermal expansion values of the developed composites numerically.

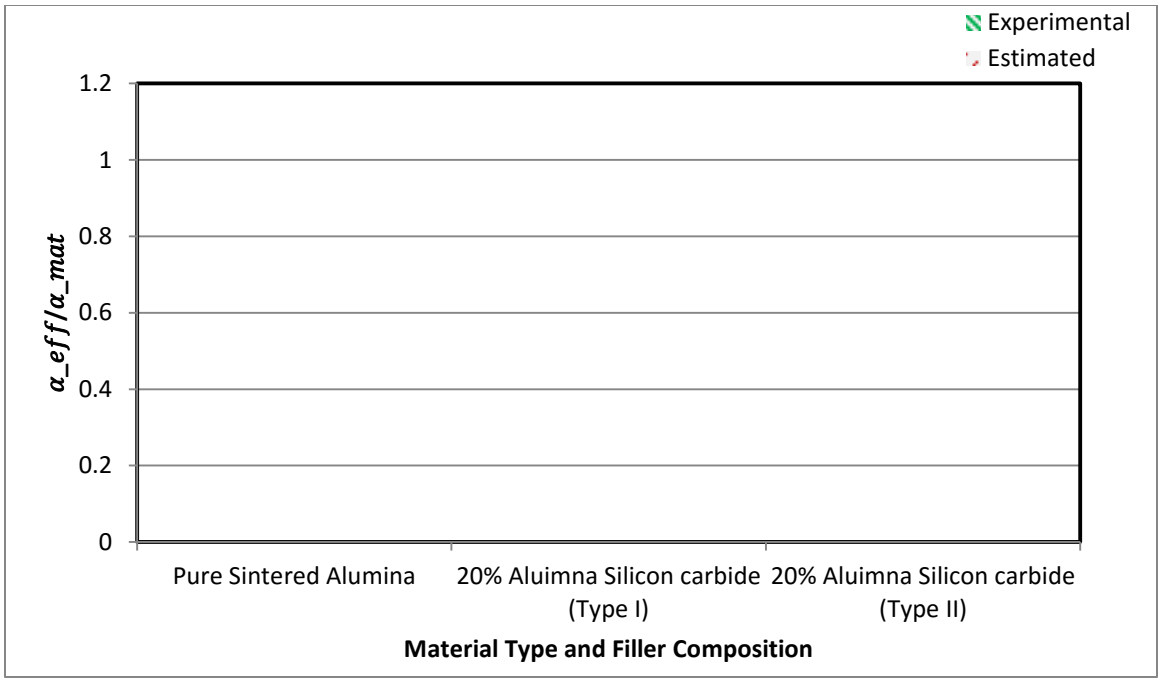


**Figure 4.22** Comparison of the effective coefficient of thermal conductivity values of the developed materials

**Table 4.6** Experimentally measured and estimated effective coefficient of thermal conductivity values of the developed materials

| Matrix | Filler Type | Filler Volume Fraction (%) | Effective Coefficient of Thermal Expansion (µm/m-°C) | | $\alpha_{eff}/\alpha_{mat}$ | |
|---|---|---|---|---|---|---|
| | | | Experiment | Estimated | Experiment | Estimated |
| Alumina | Silicon Carbide | 0 | 5.58 | | 1 | |
| | | 20 (31µm, Type I) | 4.70 | 5.48 | 0.84 | 0.98 |
| | | 20 (46µm Type II) | 4.65 | 5.48 | 0.83 | 0.98 |

## 4.4 Chapter Summary

This chapter has provided:

- The descriptions of matrix and filler material used in developing the material
- The details of the composite development
- The details of the experimental physical, mechanical and thermal property measurements
- The results from physical, mechanical and thermal test carried out on the developed samples
- A means of validating the numerical models used in estimating the effective properties of the composite

The next chapter would present the description of the thermal-structural and fatigue life performance evaluation of the direct bonded copper substrate using finite element method. The chapter would also present the results obtained from the analysis when the newly proposed ceramic is substituted into the substrate.

# CHAPTER 5

# PERFORMANCE EVALUATION OF A DIRECT BONDED COPPER SUBSTRATE

## 5.1 Introduction

In this chapter the performance evaluation of the direct bonded copper substrate with a newly proposed ceramic material for the DBC ceramic has been analyzed. The newly proposed ceramic material, an alumina composite, is to replace alumina as the DBC ceramic. The new ceramic has higher thermal conductivity and lower CTE values as compared to alumina, but it retains the adhesion strength, environmental and economic benefits of alumina.

The performance evaluation of the substrate comprises of two studies, a thermal-structural analysis and a fatigue-life cycle prediction study. These studies were evaluated using finite element analysis (FEA) as the two analyses were idealized as a3-dimensional (3D) steady-state thermal-structural and time-dependent fatigue life-cycle finite element model (FEM). The first study is a steady-state thermal stress analysis, which simulates the flow of heat generated by silicon semiconductors (die) across the substrate. This flow of heat results in increased temperature and high stress gradients. The second study is a fatigue analysis and life-prediction model which simulates the standard thermal cycling test for power electronic substrates at extreme test conditions

## 5.2 Mathematical Models

The mathematical models used in the steady-state thermal-structural performance analysis and the time dependent fatigue life prediction analysis are presented next.

For the thermal analysis, the general energy equation governs the evolution of temperature field as shown in equation (5.1):

$$C_P \boldsymbol{u}.\nabla \mathrm{T} = \nabla.(\mathrm{k}\nabla \mathrm{T}) + \mathrm{Q} \tag{5.1}$$

Where $\rho$ is the density, $C_p$ is the heat capacity, and $k$ is the thermal conductivity of the materials involved. $\nabla T$ and $Q$ are the temperature gradient and heat source, respectively. Thermal insulation is presented by an equation that restricts the movement of heat in any desired direction as shown in equation (5.2):

$$-\boldsymbol{n}.(-\mathrm{k}\nabla \mathrm{T}) = 0 \tag{5.2}$$

Where $\boldsymbol{n}$ is a unit vector that is normal to the boundary.. At the sides of the substrate material, convective heat transfer occur due to the presence or circulation of cooling air. The convective heat flux is defined by:

$$-\boldsymbol{n}.(-\mathrm{k}\nabla \mathrm{T}) = \mathrm{h}_c.(T_C - T) \tag{5.3}$$

Where $h_c$ and $T_c$ are the convective heat transfer coefficient and temperature of the surrounding air, respectively, and $T$ is the initial temperature at any point within the surface of the boundary.

For the steady-state structural analysis, the stress-strain constitutive behavior is given by:

$$-\nabla.\sigma = \mathbf{F}\mathrm{v} \tag{5.4}$$

$$\sigma - \sigma_0 = c:(\epsilon - \epsilon_0 - \epsilon_{Th} - \epsilon_{Pl}) \tag{5.5}$$

Where $\sigma$ is the Cauchy stress, $\boldsymbol{F}v$ is the body load, $\epsilon$ is the total strain value, $\epsilon_{Th}$ is the thermal strain, $\epsilon_{Pl}$ is the effective plastic strain, $\nabla\boldsymbol{u}$ is the displacement gradients, $\sigma_{ys}$ is the material yield stress, $c$ is the elastic stiffness matrix, and $\alpha$ is the CTE. The mathematical expressions for the strains are given by:

$$\epsilon = \frac{1}{2}[(\nabla\boldsymbol{u})^T + \nabla\boldsymbol{u}] \tag{5.6}$$

$$\epsilon_{Th} = \alpha(T - T_{ref}) \tag{5.7}$$

$$\epsilon_{Pl} = \lambda\frac{\partial Q}{\partial\sigma}\,,\quad \dot{F}(\sigma,\sigma_{ys}) \leq 0 \tag{5.8}$$

For the time-dependent structural analysis, the stress-strain constitutive behavior becomes:

$$\rho\frac{\partial^2\boldsymbol{u}}{\partial\mathrm{t}^2} - \nabla.\sigma = \mathbf{F}\mathrm{v} \tag{5.9}$$

$$\sigma = \mathrm{J}^{-1}\mathbf{F}\mathbf{S}\mathbf{F}^T \tag{5.10}$$

Where $\boldsymbol{S}$ is the second Piola-Kirchhoff stress, and:

$$\mathbf{F} = (1 + \nabla\boldsymbol{u}) \tag{5.11}$$

$$\mathrm{J} = \det(\mathbf{F}) \tag{5.12}$$

$$\mathbf{S} - \mathbf{S_0} = c:(\epsilon - \epsilon_0 - \epsilon_{Th} - \epsilon_{Pl}) \tag{5.13}$$

$$\epsilon = \frac{1}{2}[(\nabla \boldsymbol{u})^T + \nabla \boldsymbol{u} + (\nabla \boldsymbol{u})^T \nabla \boldsymbol{u}] \quad (5.14)$$

To eliminate the possibility for rigid-body motion, the bottom of the substrate material is fixed in all directions. Thus a roller-support boundary condition is applied on such boundary as described in equation (5.15) below:

$$\boldsymbol{n}.\boldsymbol{u} = 0 \quad (5.15)$$

The summary of the equations is given by the following:

$$[f_{ThL}] = [K_1][t] \quad (5.16)$$

$$[f] = ([K_2][d]) - [f_{ThF}] \quad (5.18)$$

Where [$f_{ThL}$] is the thermal load which could be a heat source, heat flux, heat conduction, or heat convection. [$K_1$] is a matrix, which is a function of the thermal conductivity of the material and body dimensions, and [$t$] is the temperature distribution, which are unknown. [$f_{ThF}$] can be referred to as the thermal force and it is a function of the temperature distribution [$t$], CTE, and the modulus of elasticity of the material. Where [ f ] is the applied nodal forces which is always zero if there are no external forces acting on the body apart from the thermal load, [$K_2$] is a matrix which is a function of the modulus of elasticity of the material and the dimension of the model, and [$d$] is the nodal displacement which is the unknown.

## 5.3 Thermal-Structural Analysis

The thermal and structural analysis of the substrate was evaluated using FEA. The DBC plays an important role in the product design of power electronics. It provides an interconnection pathway for semiconductor components, which ensures optimum electrical conductivity across the top surface of the substrate. It also enables the quick dissipation of unwanted heat generated by the semiconductor components to the environment. Moreover, it enables and ensures perfect electrical insulation between the semiconductors and the environment. Therefore, it is important to understand the temperature distribution as well as the localized stress distribution across the substrate.

### 5.3.1 Finite Element Modeling

The mathematical models, as defined previously for the thermal-structural steady state condition, was implemented in COMSOL multiphysics. The geometrical model for the DBC substrate comprises of five parts; two copper layers, a ceramic layer in between the two copper layers, the silicon die, and the solder as shown in figure 5.1(a). The copper and ceramic three layer part are made of a 24 mm x 24 mm square tile with uniform thicknesses of 0.3mm and 0.63mm, respectively [12]. The silicon die is also a 12 mm x 12 mm x 0.25mm tile where a solder of 12 mm x 12 mm x 0.05mm is used ideally is to attach the die to the substrate [88].

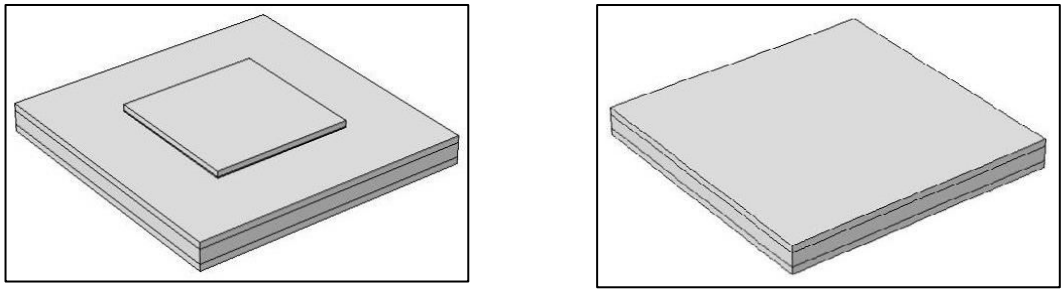

(a) (b)

**Figure 5.1** Geometrical models of the DBC substrate for (a) thermal-structural and (b) fatigue life analysis respectively

The material properties used for the ceramic were material property values determined experimentally. Two types of ceramics were used, pure alumina and a composite of alumina with 20% silicon carbide fillers. Oxygen-free high thermal conductivity (OFHC) copper was the copper type used in the analysis. The material properties of the OFHC copper, silicon die and solder were obtained from an online material property database [33] as shown in table 5.1 below.

With the silicon die in place, heat source of 4167.7 W/cm$^3$ [88], which simulates the heat generated by power electronic components, was applied as a volumetric heat source to the entire geometry of the silicon die as shown in figure 5.2(a). To simulate the real heat transfer conditions, free natural convective heat transfer was applied to the top and side surface areas of the model, excluding the area where the heat flux was applied. The convective heat transfer coefficient of air ($h_c$) is given as 10W/m$^2$-K at 300K [89]. The bottom surface was fixed at a temperature of 300K in order to simulate a heat discharge to the environment or an existing heat sink. Roller boundary conditions were applied to

the bottom of the model, and symmetry conditions were used to model one quarter of the model as shown in figure 5.2 below.

**Table 5.1** Material properties of DBC substrate at room temperature [33]

| Material | Young's Modulus (GPa) | Poisson Ratio | Yield Stress (MPa) | Thermal Conductivity ($W/m^2$-K) | CTE (µm/m-°C) |
|---|---|---|---|---|---|
| Copper | 110 | 0.35 | 210 | 400 | 17 |
| Alumina (Current) | 300 | 0.22 | - | 33.03 | 5.48 |
| Alumina Composite (Proposed) | 200 | 0.22 | - | 38.31 | 4.7 |
| Silicon Die | 170 | 0.28 | - | 130 | 2.6 |
| Solder | 10 | 0.4 | - | 50 | 21 |

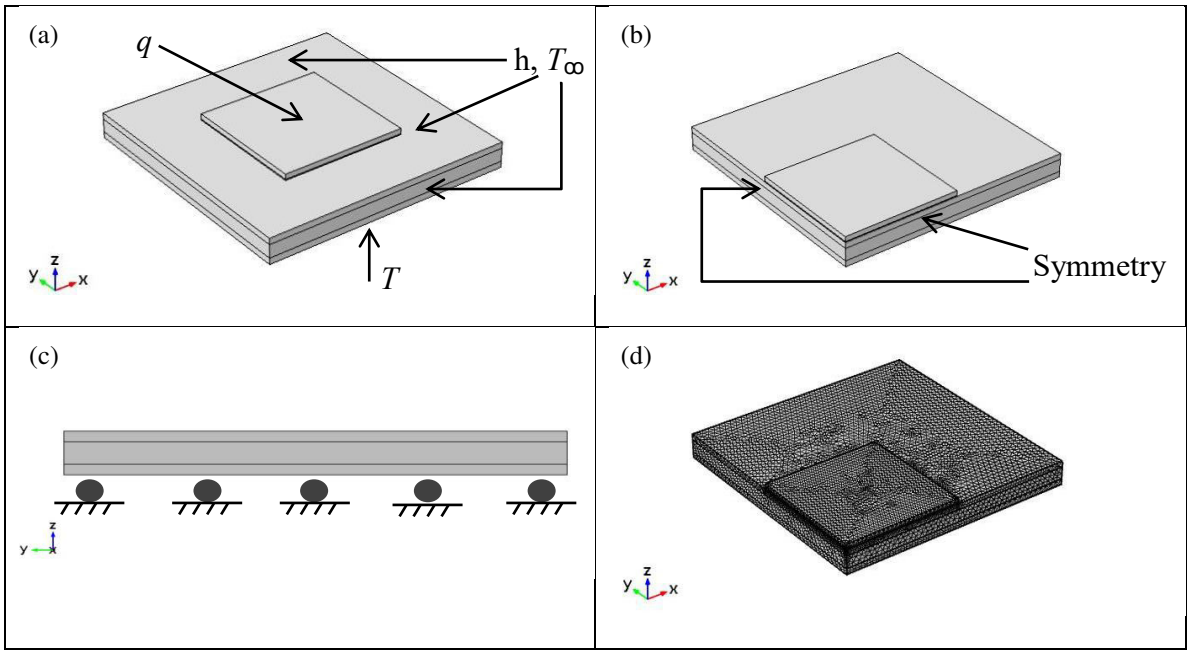


**Figure 5.2** Schematic views of the DBC's geometrical model FE loading and mesh

Meshing using tetrahedral shaped elements was initially performed on the FE model with 6564 elements, and then increased to 42611 after the mesh sensitivity analysis. The mesh was refined at certain critical regions where the maximum von Mises stresses were generated. The mesh convergence test was performed based on the von Mises stress distribution and the nodal displacement of the FE model. The von Mises stress distribution and nodal displacements became constant when the numbers of elements within the model reach 42611 and 21891 respectively. The von Mises stress and nodal displacement values further remained constant when the number of elements within the model was further increased to 168739. Figures 5.2(d) shows the final elemental meshed and figure 5.3 shows the mesh convergence plot. Thus, the mesh with 42611 elements is considered to be computationally effective for the thermal-structural analysis presented in the present study.

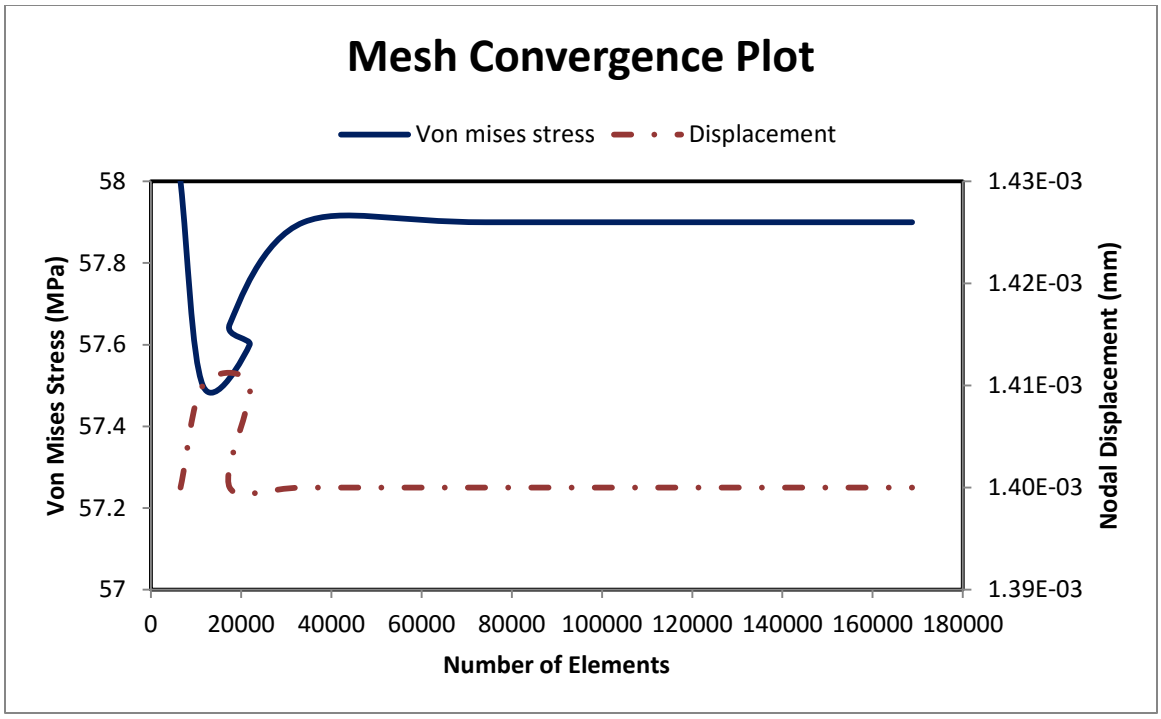


**Figure 5.3** Mesh Convergence

### 5.3.2 Results and Discussion

Results were obtained when the heat source was generated within the silicon die positioned at the top of the substrate. The highest surface temperature was within the silicon die and its region as seen in figure 5.4(a). The temperature difference of 20°C between the highest and lowest temperature range in this model is comparable to 8°C obtained with an aluminum nitride DBC ceramic [88]. The heat flux distribution in figure 5.4(b) shows that most of the heat flux generated is transferred immediately to the bottom of the substrate and just a small quantity of the flux remains at the surface of the substrate. More displacement where seen at the edges than at the center of the substrate (as seen in figure 5.4(c)), but the localized von Mises stresses were generated within the top copper layer directly beneath the silicon die as seen in figure 5.4(d).

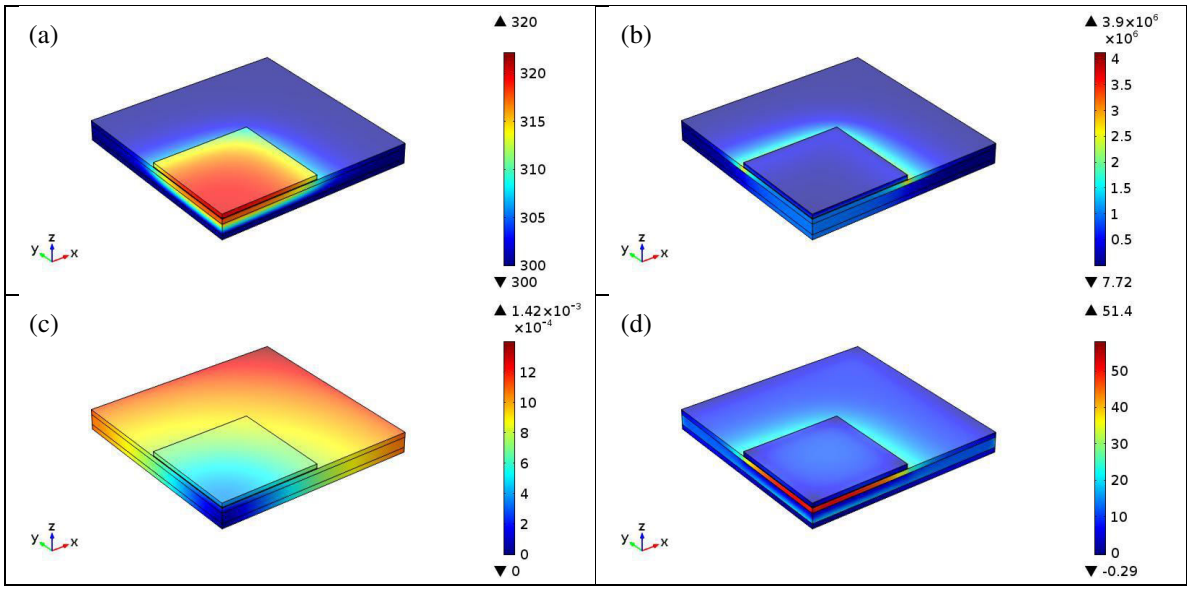


**Figure 5.4** Finite element results showing (a) Temperature distribution (K), (b) Heat flux distribution ($W/m^2$) , (c) Total displacement (m), and (d) Von Mises stress distribution (MPa) of the DBC substrate with alumina composite as DBC ceramic

The stress, strain and temperature variation across the thick of the substrate is to be observed at three locations taken from the center of the substrate as illustrated in figure 5.5(a).

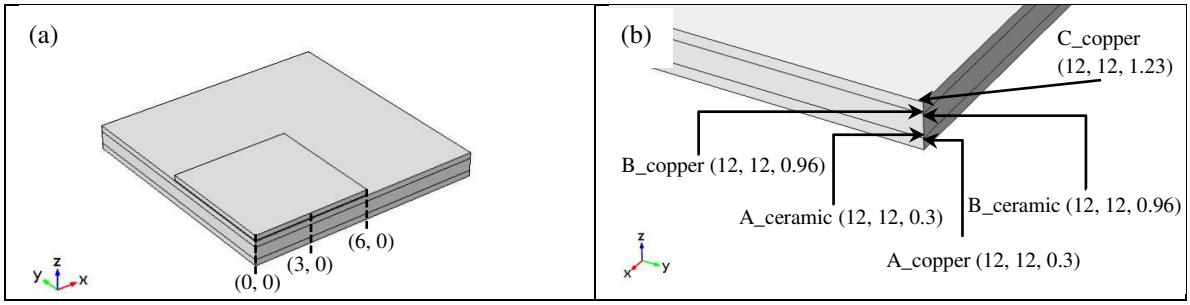


**Figure 5.5** Geometrical model of the FE model showing the locations where so plots were taken across the substrate

The plots in figures 5.6 to 5.8 taken at three different locations from the center of the substrate shows the localized stress, strain, and temperature values as it vary along the thickness of the substrate assembly.

Figure 5.6 to 5.8 compares the stress, strain and temperature distributions within the DBC substrate when alumina ceramic and the newly proposed ceramic (alumina composite) are used as DBC ceramics in the substrate. The stress distribution in the *x* and *y*-directions are identical to each other as seen in Figure 5.6. These stress distribution in the *x* and *y*- directions are higher than the stress distribution in the *z*- direction as seen in Figure 5.6 also, this is because the loading was only in the *z*- direction and constraints within the copper and the ceramic were in the *x*-*y* plane. From the localized stress distribution in both *x* and *y* directions along the thickness of the model, the highest stress values were generated within the base of the ceramic just at the interface with the copper layer at the bottom, where its own stress distribution is zero. The stress values in the *x* and *y* directions within the solder and silicon die are also within the zero range, while the ones within the copper layer at the top surface are compressive. The stress buildup within the ceramic and copper layers at the top reduced when the newly proposed ceramic was introduced into the substrate, while the ones at other regions remained constant. In addition, the stress distribution in the *z*- direction did not change when the newly proposed ceramic was substituted into the substrate.

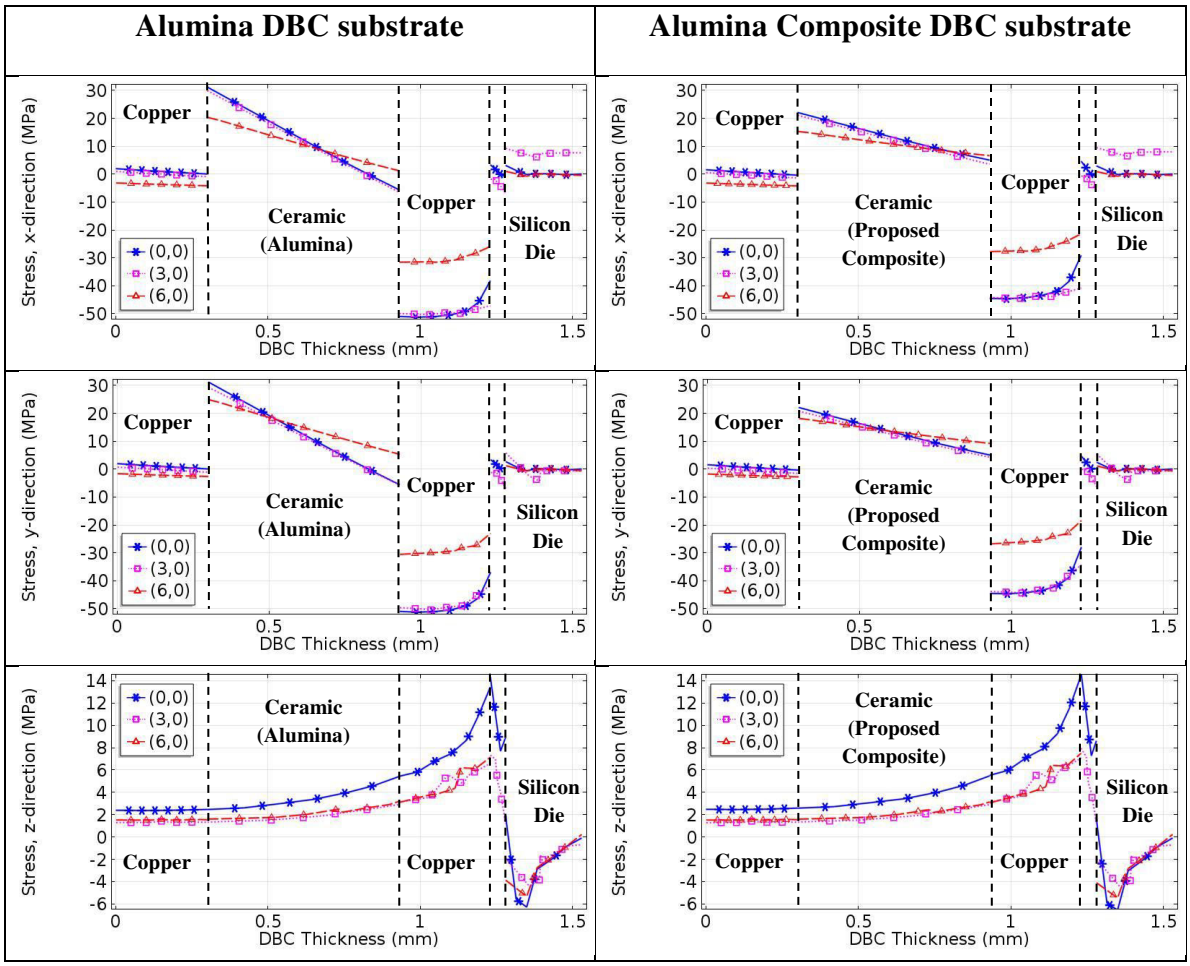


**Figure 5.6** Stress variations in the three directions across the thickness of the substrate

As seen in figure 5.7, the von Mises stress and temperature distributions within the DBC substrate reduced when the newly proposed DBC ceramic was used as the substrate. Although the reduction was not quite high, the little reduction reduces the risk of the substrate and solder fatigue failure.

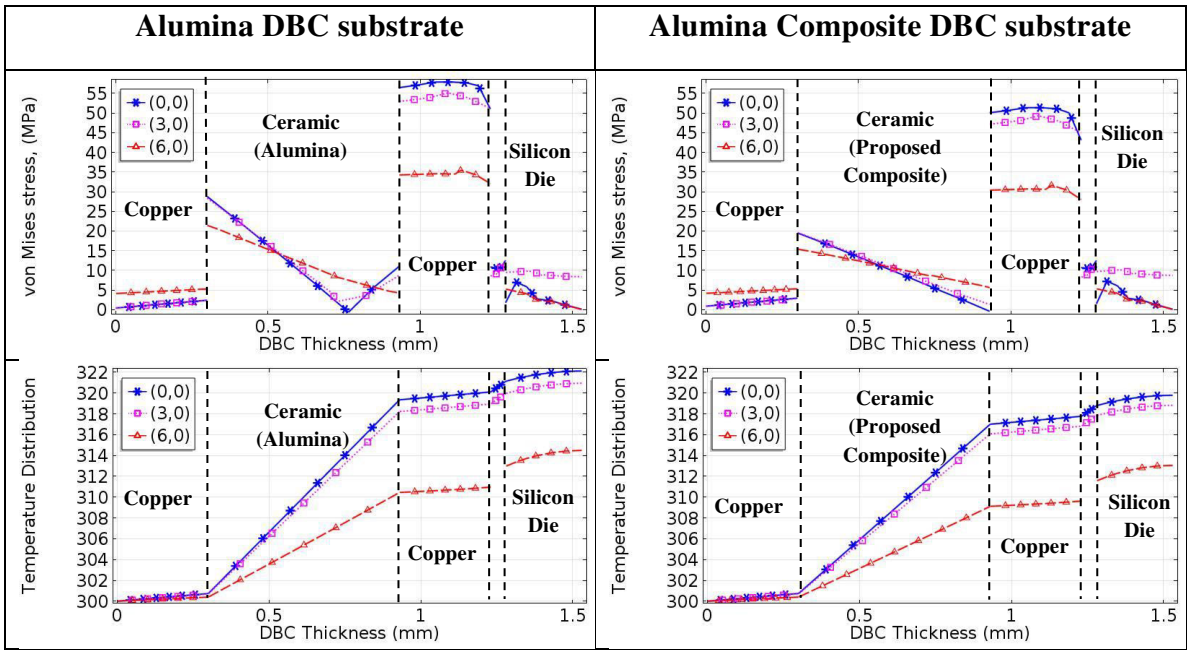


**Figure 5.7** Von mises stress and temperature variation across the thickness of the substrate

The three directional thermal strains along the thickness of the substrate are found to be equal to each other, as shown in figure 5.8, because heat transfer occurs in one direction. Likewise, the CTE and temperature distribution within the model in all three directions are constant due to the use of isotropic material model. Thus, the highest thermal strain was generated within the solder and the top copper layer. Low thermal strain was generated within the ceramic and the copper layer at the bottom of the substrate. The thermal strains within the silicon die were close to zero. The high thermal strain generated within the solder and top surface copper region increases the chances of solder and substrate failure, but as the newly proposed ceramic was substituted into the substrate, these strain values reduced, and hence reducing the chances of the solder and substrate failure.

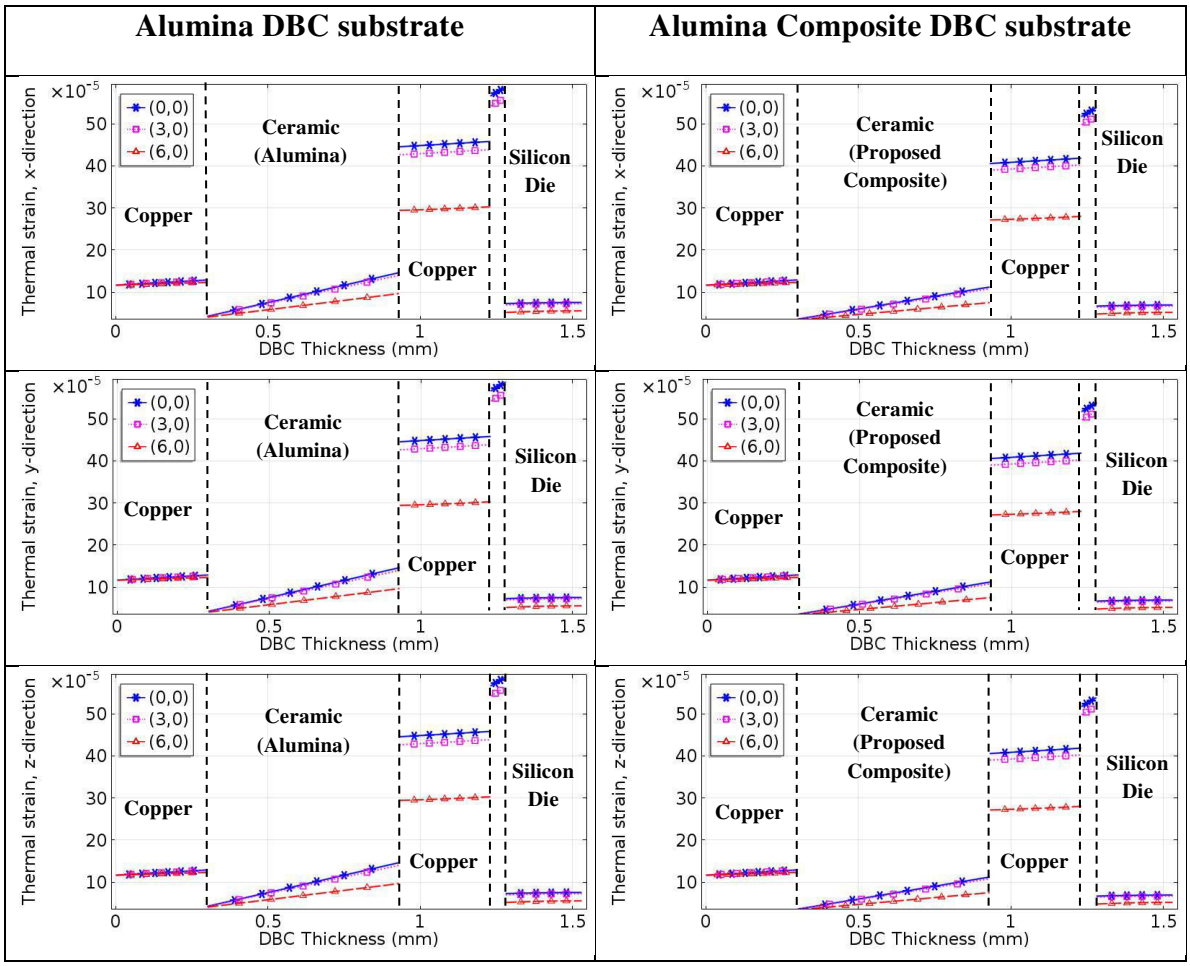


**Figure 5.8** Thermal strain variations in the three directions across the thickness of the substrate

## 5.4 Fatigue Life Prediction

Using FEA, the fatigue life of DBC substrate with the newly proposed ceramic material was evaluated numerically. This fatigue life analysis was based on the Joint Electron Device Engineering Council (JEDEC) testing standards. The fatigue life cycle of the DBC substrate was investigated using the extremely low cycle fatigue (ELCF) life model

for plastic materials, which is a modified version of the Manson-Coffin fatigue model for low cycle fatigue (LCF). Ductile materials, like copper, are susceptible to plastic failure whenever they come under periodic cyclic thermal loads, and based on experimental work in the literature, failure first originates from the copper layers.

In order to describe the cyclic failure mechanism of materials with failure cycles below $10^4$ cycles (LCF), and to predict its fatigue life when cyclic loads are applied to the material, the Manson-Coffin [50] model is used. The Manson-Coffin model is based on the plastic strain amplitude of the material, but in situations where the number of cycles is very small (below 100 cycles, i.e. ELCF), the Manson-Coffin model cannot predict the cyclic life. Therefore, a modified version of the model by Xue's[51] works better for fatigue life predictions for materials with cycles below 100. From various experimental work on the fatigue life cycle prediction of DBC substrates under extreme thermal cyclic loading (-55 to 250 °C) conditions, the fatigue life of DBC substrates has been estimated to be less than 100 cycles, thus Xue's model can be used in predicting the fatigue life cycle of DBC substrates as done in previous research works [49], [90]. In this work, Xue's model for ELCF materials was used in predicting the number of cycles to failure of the DBC substrate. The ELCF prediction equation is given by:

$$N = \frac{1}{2}\frac{e^{\lambda}-1}{e^{\lambda(\varepsilon_d/\varepsilon_f)^c}-1} \tag{5.19}$$

Where $N$ is the fatigue life, $c$ and $\lambda$ are material constants with values of 1.76 and 2.7 for copper, respectively, $\varepsilon_d$ is a function of the principle strains ($\varepsilon_1$, $\varepsilon_2$, $\varepsilon_3$), and $\varepsilon_f$ is the total or effective plastic failure strain.

$$\varepsilon_d = \sqrt{\frac{2}{3}} * \sqrt{{\varepsilon_1}^2 + {\varepsilon_2}^2 + {\varepsilon_3}^2} \quad (5.20)$$

### 5.4.1 Finite Element Modelling

For the fatigue life prediction, the mathematical model defined for the structural time-dependent condition was implemented in COMSOL multi-physics. The geometrical model for the DBC substrate comprises only of three parts; two copper layers and a ceramic layer in between the copper layers as shown in figure 5.1(b).

Based on JEDEC's standard JESD22-A104D, the thermal cycling for evaluating the thermal fatigue life of electronic packaging materials is applied as a constant temperature heat source (i.e. applied as a thermal body load). The thermal cycling effect for this study was designed based on the JEDEC standard (as shown in figure 5.9) within a temperature range of -55 to +150°C. The soak time at the maximum and minimum temperature point was set as 2min, while the ramp rate was taken as 12.5°C/min. The temperature cyclic loading, the roller boundary conditions, and the symmetry conditions were applied as shown in 5.10(a), 5.10 (b), and 5.10 (c), respectively.

The model was meshed using tetrahedral elements. The mesh was refined at certain critical regions where the maximum von Mises stresses were generated. Mesh sensitivity analysis was performed based on the von Mises stress distribution and the nodal displacements of the FE model. Both became constant when using 56365 elements.. Figures 5.10(d) shows the final elemental mesh of the model and figure 5.11 shows the mesh convergence plot.

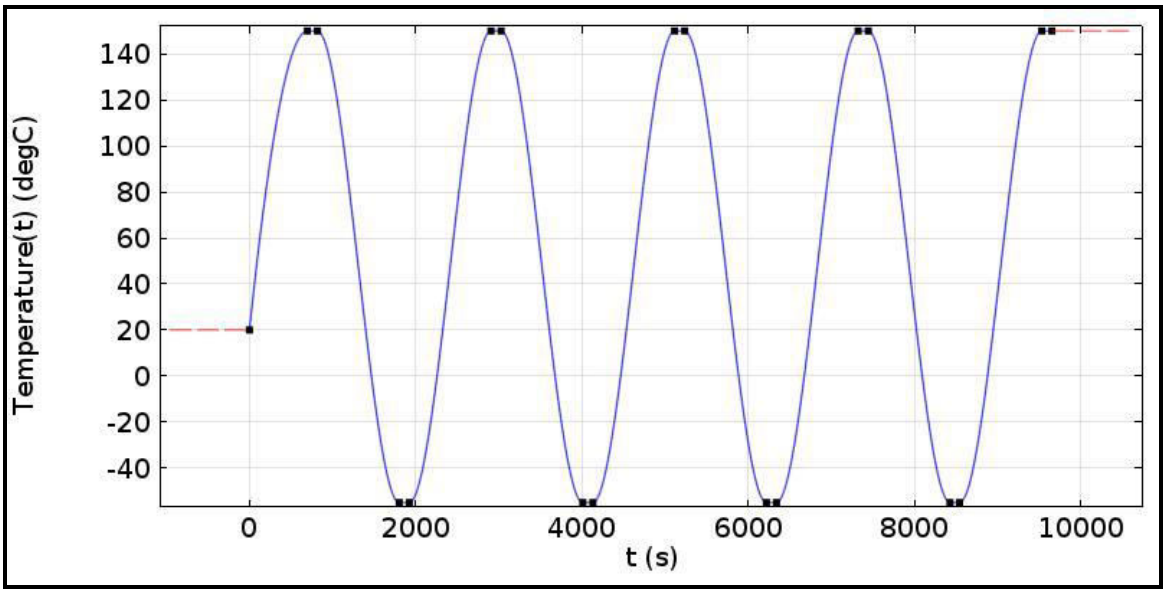


**Figure 5.9** Thermal cyclic load based on JESD22-A104D [91]

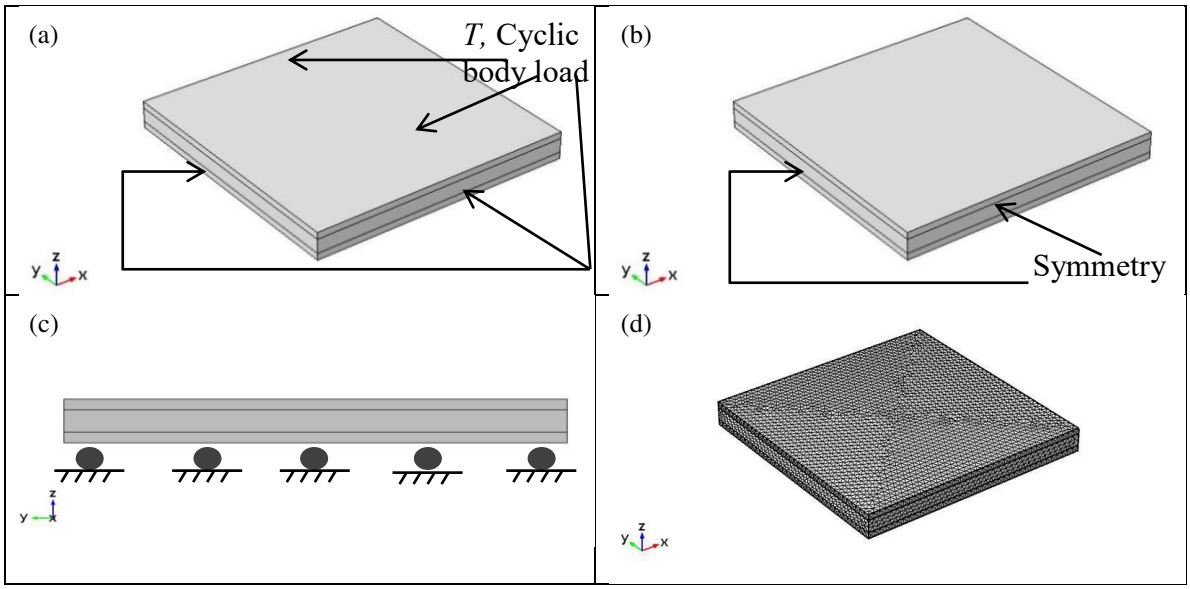


**Figure 5.10** Schematic views of the DBC's geometrical model FE loading and mesh

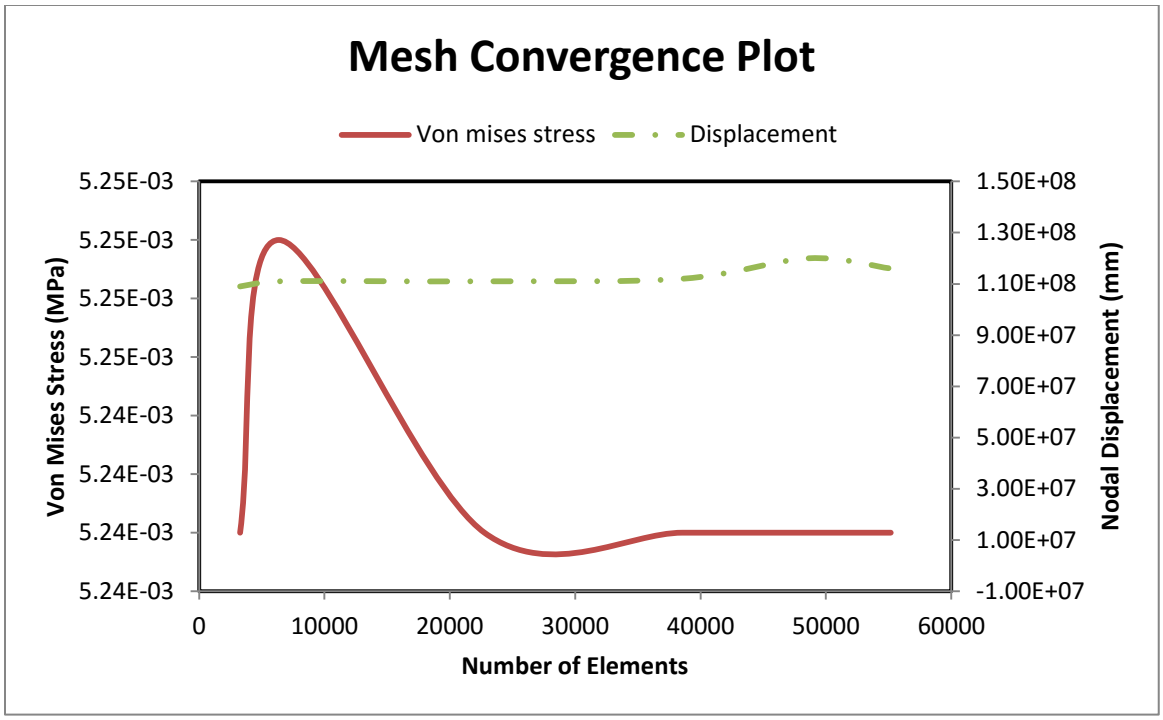


**Figure 5.11** Mesh Convergence

### 5.4.2 Results and Discussion

The results from the structural and thermal cycling analysis consist of a stress-strain spatial distribution obtained at the lower and higher temperatures (-55 and 150°C), and a temporal distribution obtained at certain critical points within the FE model over time. The spatial distributions in figure 5.12 show the stress distribution in the three directions (*x, y* and *z*) at the lowest and highest temperatures, which occur at the peaks and valleys of the thermal cycling. The stress values in the *x* and *y* directions are of the same range in terms of magnitude.

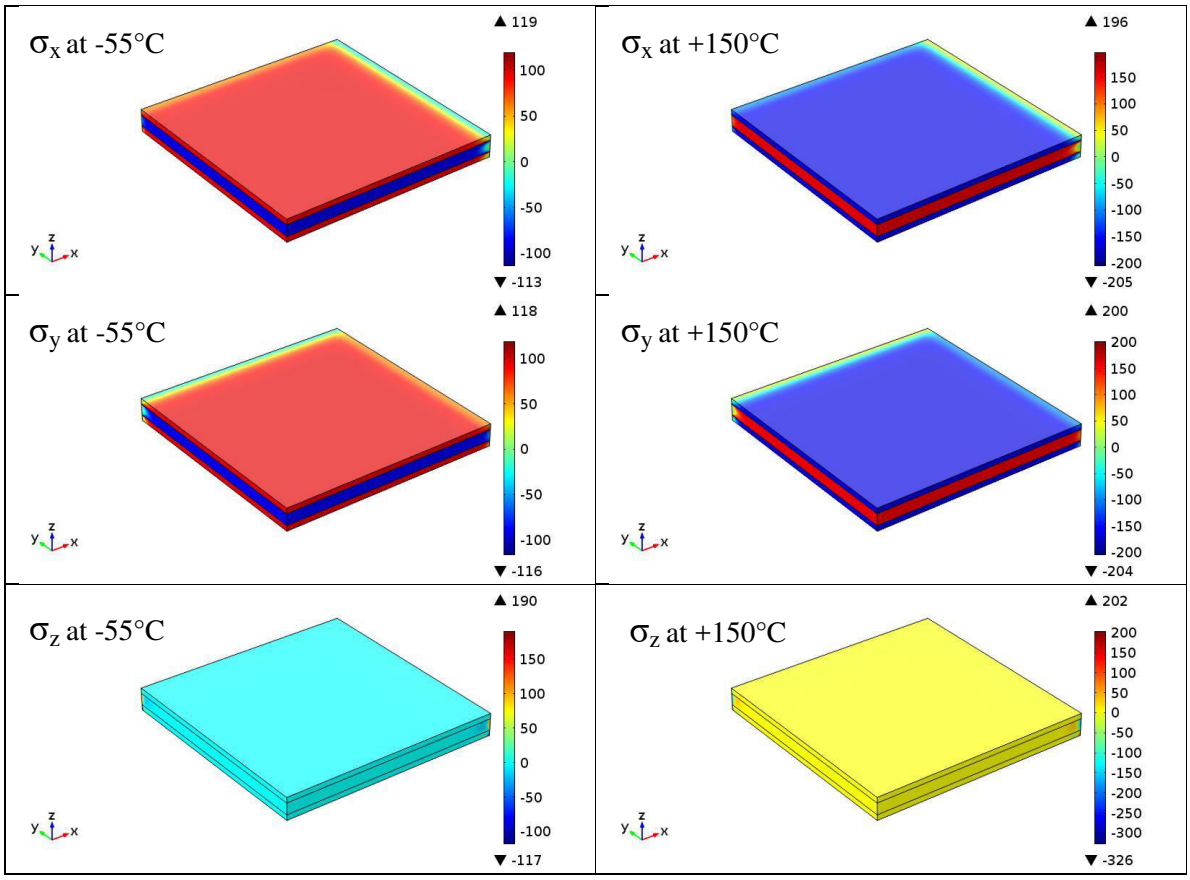


**Figure 5.12** Spatial distribution of stress (MPa) values in all three directions at the maximum and minimum time frames

At the lower temperature range, the maximum stress values in the *x* and *y* directions seem to appear within the copper as shown in figure 5.12. While the maximum stress values appeared within the ceramic at the higher temperature range. The maximum overall stress distribution within the substrate was in the *z*- direction at the higher temperature range. Figure 5.13 shows the strain distribution at maximum and minimum temperatures. The strain values were higher at the edges of the substrate at the copper-ceramic interface when the load was at the highest temperature value. On the other hand, the strain values became very small with some regions having negative values at the lower temperature values.

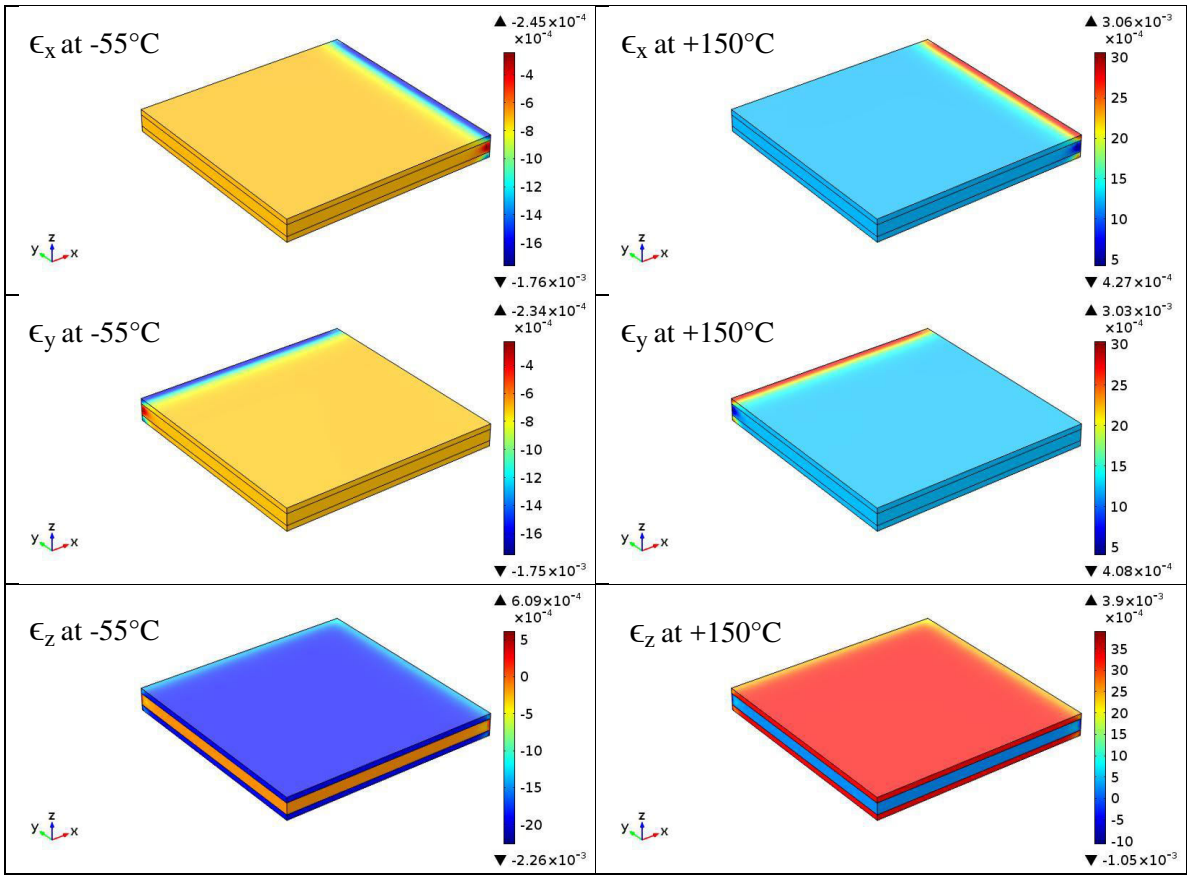


**Figure 5.13** Spatial distribution of total strain values in all three directions at the maximum and minimum time frames

The temporal plots in figures 5.14 to 5.16 were taken at five different locations at the corner of the substrate as shown in figure 5.5(b). The plots show the variation of the stress and strain values with time. The points were selected at the corner edges of the substrate within the copper-ceramic interface as they are more susceptible to failure because maximum stress and strain values have been observed at those regions. This is due to the fact that these points are located at regions that are not constrained in any direction, which in turn confirms the experimental failure modes of DBC substrates at those locations.

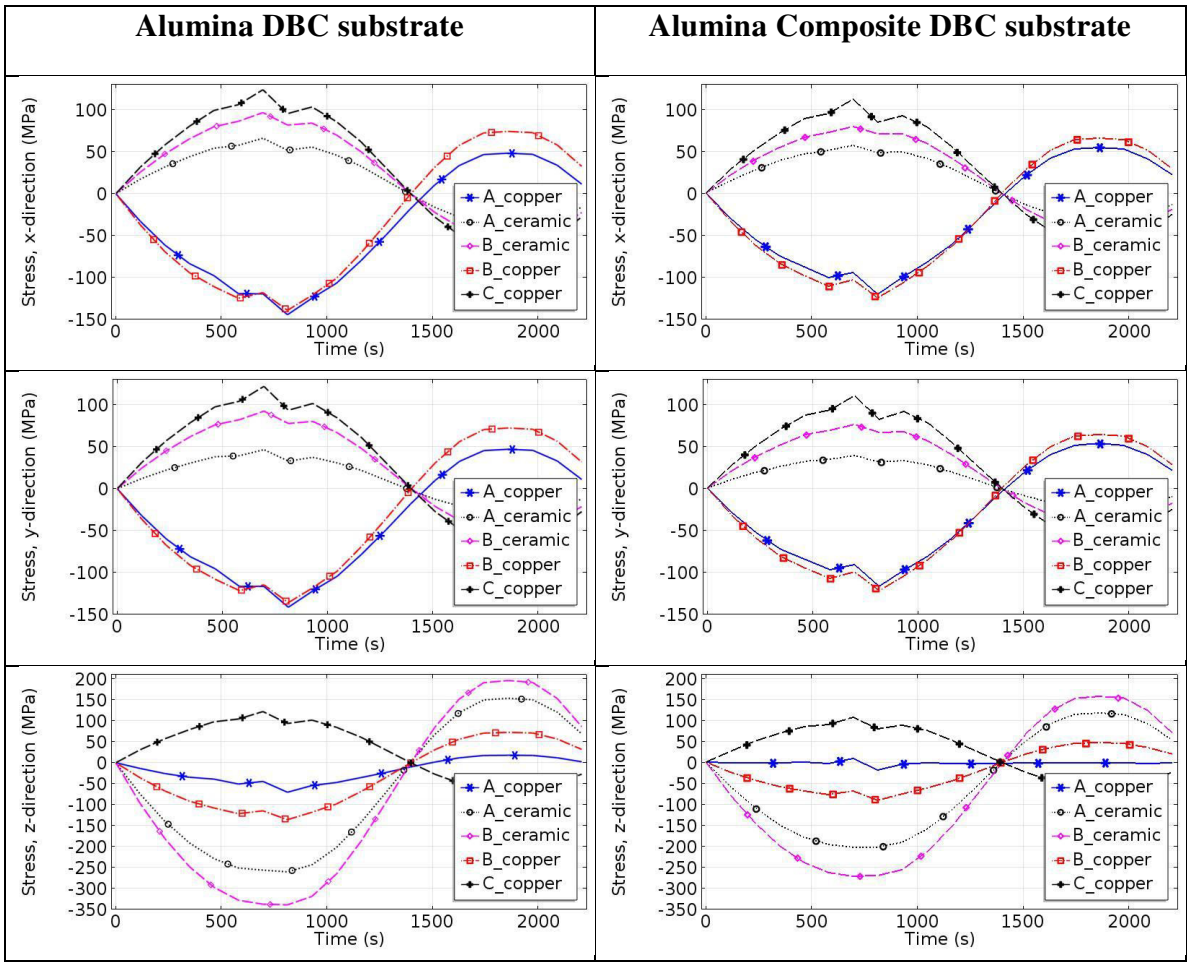


**Figure 5.14** Stress variation with thermal cycling time an points within the substrate

As shown in figures 5.14 to 5.16, stress and strain values were reduced when the newly proposed ceramic was substituted into the substrate, especially the values at the top surface of the substrate which could reduce the risk of substrate and solder failure. The effective plastic strain value was reduced by around 30-40% of the initial value obtained when alumina DBC ceramic was in use.

The results obtained in figures 5.14 and 5.15 (for the temporal plots) are the same as the ones obtained from the spatial plots (shown in figures 5.9 and 5.10). As seen in figures

5.14 and 5.15, stress and strain values reduced a little bit (especially the values at the top surface of the substrate which could reduce the risk of substrate and solder failures) when the newly proposed ceramic was substituted into the substrate except for the effective plastic strain value which reduced by about half of the initial value obtained when alumina DBC ceramic was in use as seen in figures 5.16.

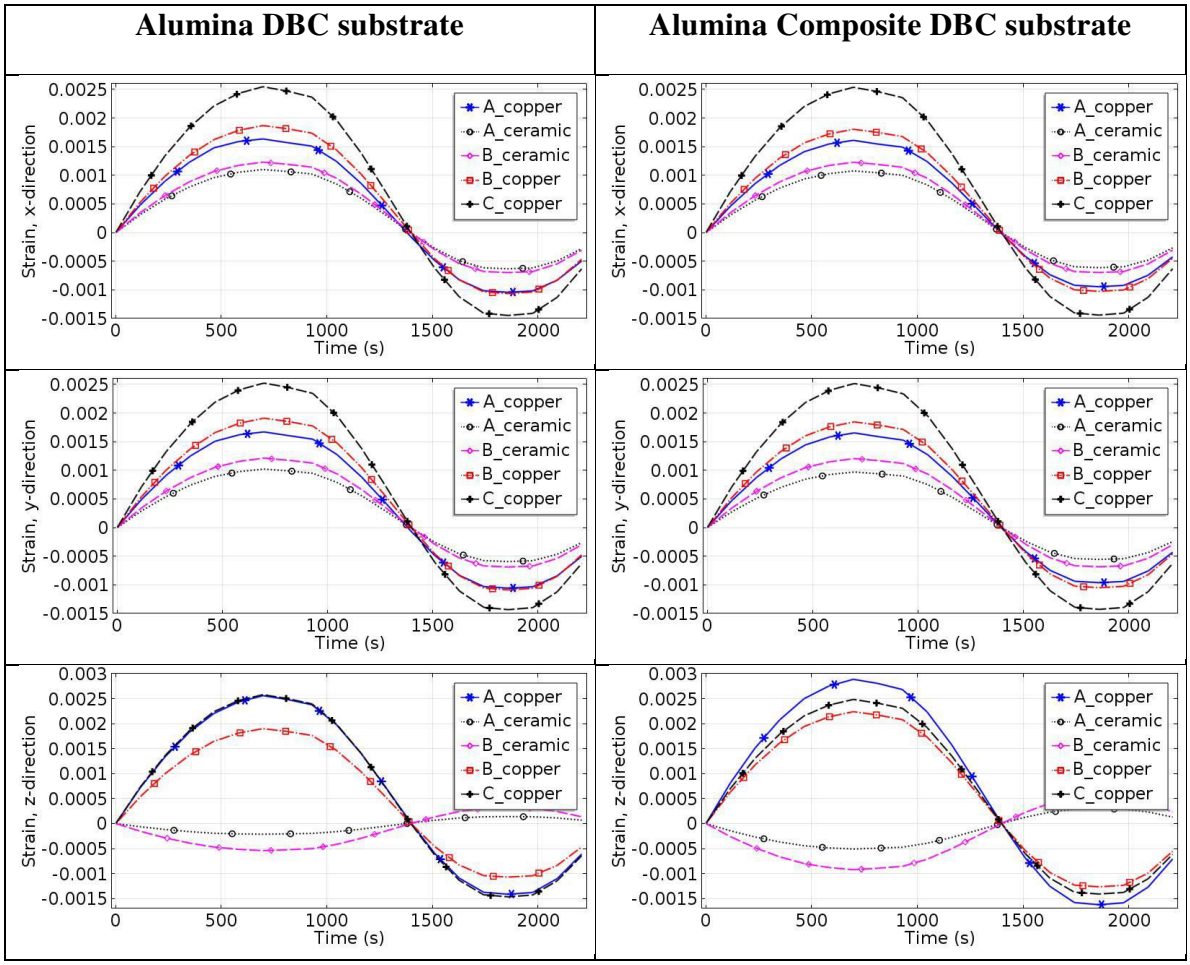


**Figure 5.15** Stress variation with thermal cycling time an points within the substrate

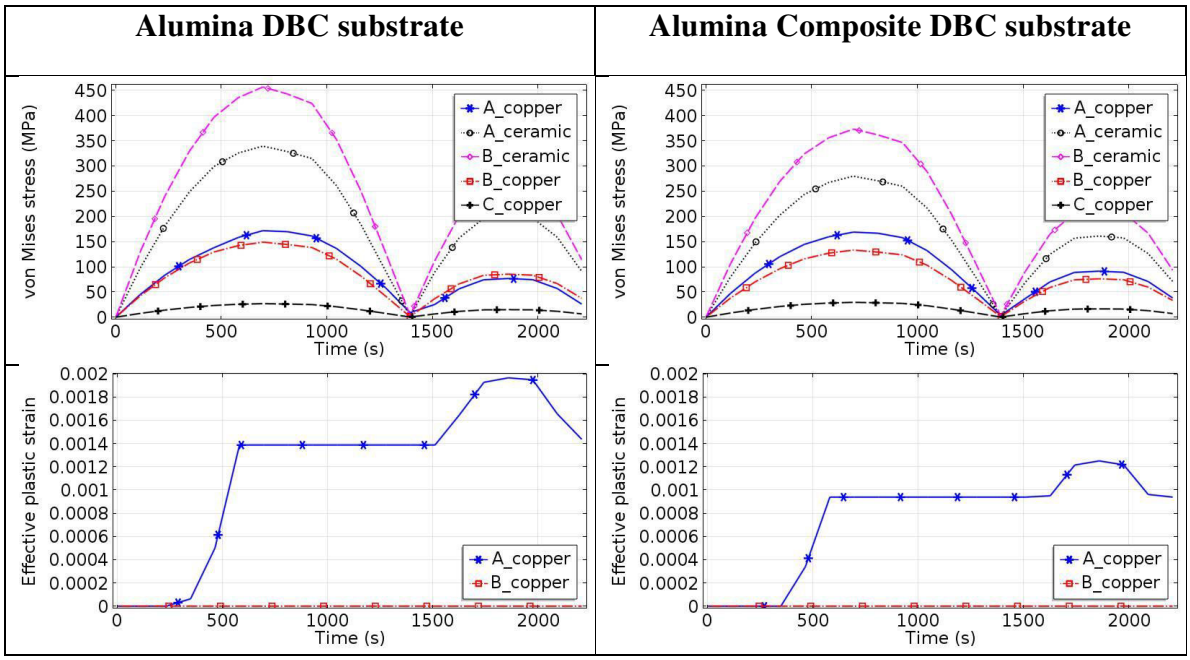


**Figure 5.16** Von mises stress and effective plastic strain variation with thermal cycling time at points within the substrate

For the effective plastic strain variation with time, the corner edges within copper at the two copper-ceramic interfaces was chosen as a likely failure point because copper is more susceptible to failure than the ceramic due to copper having a lower yield point compared to ceramics. The delamination of the copper layer from the ceramic layer later initials cracks in the ceramic.. It could be seen that the plastic strains start at the interface between the ceramic and the lower copper layer as soon as the temperature starts increasing, the value was maintained when the temperature started dropping but started increasing more when the cyclic loading reached the lowest temperature value. Later, the value dropped back to the previously maintained value.

From Xue's [51] model for predicting the fatigue of ELCF materials, the fatigue life of the DBC substrate was estimated.

**Table 5.2** Number of cycles to failure

| | No. of cycles |
|---|---|
| Alumina DBC substrate | 29 |
| Alumina Composite DBC substrate | 63 |

From table 5.2, it could be seen that the number of cycles to failure of the substrate increased by almost a factor of 2 when the DBC ceramic was replaced with the newly proposed ceramic having higher thermal conductivity and lower CTE. This shows that replacing an alumina DBC ceramic with one having higher thermal conductivity and lower CTE could actually improve the fatigue life of the substrate. It is important to note that even with the same loading conditions, the number of cycles to failure for the alumina DBC substrate in table 1 are not comparable because the thickness of the copper and ceramic layers are different.

## 5.5 Model Validation

The finite element model used here was validated with the works of Xu *et.al* [22]. While using the same geometrical and material model, the number of cycles to failure of the substrate was predicted to be 41 cycles and where the predicted value in their work was within a range of 38 to 44 cycles. In this work, the geometrical model of the substrate was taken from the works of Liu [5].

## 5.6 Chapter Summary

This chapter has provided:

- The thermal-structural behavior of a direct bonded copper substrate with a newly proposed DBC ceramic using finite element method
- The fatigue life cycle of a direct bonded copper substrate with a newly proposed DBC ceramic using finite element method
- The fatigue life cycle calculation using the extremely low cycle fatigue model.
- A comparative study between results obtained when the current alumina DBC ceramic and the newly proposed alumina composite DBC ceramic is used in the DBC substrate

The next chapter would present a description conclusion to this work as a whole and adequate recommendation.

# CHAPTER 6

# CONCLUSIONS AND RECOMMENDATIONS

## CONCLUSIONS

The newly proposed ceramic material for applications in power electronic substrates which must possess higher thermal conductivity and lower CTE values as compared to alumina, but while retaining the adhesive strength (between alumina and copper), environmental and economic benefits of alumina was designed, developed and characterized.

The material was designed to be an alumina composite with either of silicon carbide, chromium or diamond as fillers since no other ceramic possess the adhesive strength (between alumina and copper in DBC application), environmental and economic benefits of alumina. Computational models used in predicting the effective properties of particulate composites were used for evaluating and optimizing appropriate filler volume fraction and particle sizes.

Using spark plasma sintering (SPS) three samples were developed, one pure alumina and two alumina composites with 20% silicon carbide (31 and 46µm from two different manufactural) . The developed alumina-silicon carbide composites turned out to have lower density (from 3.91 to 3.81g/cm$^3$), higher thermal conductivity (from 33 to 38W/m$^2$ K) and lower CTE (from 5.58 to 4.7µm/m-°C) values when compared with pure alumina, but the hardness value of the alumina composite materials reduced as compared to the

pure alumina which could be associated with the poor interfacial bond between alumina and silicon carbide. XRD patterns of the samples showed no chemical reactions between the alumina matrix and silicon carbide fillers.

The performance evaluation was conducted using finite element method (FEM) by considering the thermal-structural and fatigue life of the DBC substrate with the newly proposed ceramic material. Normal working and extreme thermal cycling conditions were simulated and analyzed, where the temperature, strain and localized stress distribution within the substrate at a steady state condition was analyzed, and the improved Coffin-Mason law was used in calculating the fatigue life of the substrate under extreme thermal cycling conditions. The newly proposed ceramic (alumina composite) demonstrated more robust properties than alumina as a DBC ceramic in the substrate due to improved thermal-mechanical performance which reduces the risk of substrate and solder failure. Also, the fatigue life cycle of the substrate under transient thermal cycling test (based on JEDEC's standards) improved when the newly proposed and developed ceramic was substituted into the substrate with about 100% increment in the life cycle over an alumina DBC ceramic.

## RECOMMENDATIONS

A means of strengthen the interfacial bond between the alumina matrix and silicon carbide filler materials still needs to be developed, so has to improve the hardness of the material. The sintering temperature of the composite still needs to be optimized since alumina and silicon carbide do not sinter at the same temperatures because silicon carbide has a higher melting point than alumina, as this could be a way of improving the interfacial bond between the matrix and filler material.

An experimental means of determining the electrical conductivity of the developed samples still needs to be explored because the sample is a high electrical insulating material. Also a better nondestructive experimental means of determining the modulus elasticity of small samples needs to be explored as know existing means are destructive in nature.

The ceramic-copper adhesive strength between the newly proposed developed ceramic (alumina composite) and copper needs to be explored and results obtained compared with the adhesive strength between alumina and copper.

# References


[1] P. Guru, “Failure Mechanisms During Power Cycling,” *Design Considerations, Power Design, Thermal Management*, 2013. [Online]. Available: http://www.powerguru.org/failure-mechanisms-during-power-cycling/.

[2] Wikipedia.com, “Wikipedia, Online Encyclopedia.” 2015.

[3] Power-technology.com, “Power Technology, Silicon Power - Power Electronics Systems and Components.” p. 2015.

[4] A. Lindemann and G. Strauch, “Properties of Direct Aluminum Bonded Substrates for Power Semiconductor Components,” *IEEE Trans. Power Electron.* , vol. 22, no. 2, pp. 384–391, 2007.

[5] M. Advanced Thermal Solutions, Inc. Norwood, “Direct Cooling of Power Modules Using Microchannel Structures,” *Power Electronics*, 2010. [Online]. Available: http://powerelectronics.com/thermal-management/direct-cooling-power-modules-using-microchannel-structures.

[6] C. C. Schüler, a. Stuck, N. Beck, H. Keser, and U. Täck, “Direct silver bonding - an alternative for substrates in power semiconductor packaging,” *J. Mater. Sci. Mater. Electron.*, vol. 11, no. 5, pp. 389–396, 2000.

[7] K. Hromadka, J. Stulik, J. Reboun, and A. Hamacek, “DBC Technology for Low Cost Power Electronic Substrate Manufacturing,” in *Procedia Engineering*, 2014, vol. 69, pp. 1180–1183.

[8] Y. S. Sun and J. C. Driscoll, “IEEE Trans.,” *IEEE Trans. Electron Devices*, vol. 23, p. 961, 1976.

[9] J. F. Burgess, C. A. Neugebauer, and G. Flanagan, “.,” *Electrocomp. Sci. Technol*, vol. 2, no. 4, p. 233, 1976.

[10] J. Schulz-Harder, “Advantages and new development of direct bonded copper substrates,” *Microelectron. Reliab.*, vol. 43, no. 3, pp. 359–365, 2003.

[11] G. Dong, X. Chen, X. Zhang, K. D. T. Ngo, and G.-Q. Lu, “Thermal fatigue behaviour of Al<DN>2</DN>O<DN>3</DN>-DBC substrates under high temperature cyclic loading,” *Solder. Surf. Mt. Technol.*, vol. 22, no. November 2009, pp. 43–48, 2010.

[12] Y. Liu, *Power Electronic Packaging: Design, Assembly Process, Reliability and Modeling*. 2012.

[13] Y. . Mei, G.-Q. . Lu, X. . Chen, C. . Gang, S. . Luo, and D. . Ibitayo, “Investigation of post-etch copper residue on direct bonded copper (DBC) substrates,” *J. Electron. Mater.*, vol. 40, no. 10, pp. 2119–2125, 2011.

[14] L. . Li, Z. Zhang, and L. . Zhao, “Strength and toughness of ZrO2-based ceramics at cryogenic temperatures,” *Cryogenics (Guildf).*, vol. 34, p. 469, 1994.

[15] Z. Xie, W. Xue, H. Chen, and Y. Huang, “Mechanical and thermal properties of 99% and 92% alumina at cryogenic temperatures,” *Ceram. Int.*, vol. 37, no. 7, pp. 2165–2168, 2011.

[16] N. Suzuki, T. Uchida, and K. Suzuki, “Test method and strength characteristics of alumina ceramics at cryogenic temperatures,” *Cryogenics (Guildf).*, vol. 38, no. 4, pp. 363–366, 1998.

[17] M. Scheffler and P. Colombo, *Cellular Ceramics—Structure, Manufacturing, Properties and Applications*. Weinheim: Wiley–VCH, 2005.

[18] R. W. Rice, *Porosity of Ceramics*. New York: Marcel Dekker, 1998.

[19] Z. Živcová, E. Gregorová, W. Pabst, D. S. Smith, A. Michot, and C. Poulier, “Thermal conductivity of porous alumina ceramics prepared using starch as a pore-forming agent,” *J. Eur. Ceram. Soc.*, vol. 29, no. 3, pp. 347–353, 2009.

[20] S. Wada, B. Piempermpoon, and P. N. Nakorn, “Thermal Conductivity of Al2O3 Ceramics : The Inconsistency between Measured Value and Calculated Value Based on Analytical Models for a Composite การน ำความร อนของอะล ู ม ิ นาเซราม ิ ก : ความไม สอดคล องก ับระหว าง ค ากาารน ำความร อนท ี่,” *J. Sci. Res. Chulalongkorn Univ.*, vol. 30, no. 1, pp. 109–120, 2005.

[21] T. Nemoto, S. Sasaki, and Y. Hakuraku, “Thermal conductivity of alumina and silicon carbide ceramics at low temperatures,” *Cryogenics (Guildf).*, vol. 25, no. 9, pp. 531–532, 1985.

[22] R. Barea, M. Belmonte, M. I. Osendi, and P. Miranzo, “Thermal conductivity of Al2O3/SiC platelet composites,” *J. Eur. Ceram. Soc.*, vol. 23, no. 11, pp. 1773–1778, 2003.

[23] B. Nait-Ali, K. Haberko, H. Vesteghem, J. Absi, and D. S. Smith, “Preparation and thermal conductivity characterisation of highly porous ceramics. Comparison between experimental results, analytical calculations and numerical simulations,” *J. Eur. Ceram. Soc.*, vol. 27, no. 2–3, pp. 1345–1350, 2007.

[24] C. Poulier, D. S. Smith, and J. Absi, “Thermal conductivity of pressed powder compacts: tin oxide and alumina,” *J. Eur. Ceram. Soc.*, vol. 27, no. 2–3, pp. 475–478, 2007.

[25] J. Osorio-Ramos, E. Refugio-Garcia, E. Terres-Rojas, J. A. Miranda-Hernadez, and Rodríguez-garcía, “Alumina-Based Composites Reinforced With Ductile Particles,” vol. 2, no. 6, pp. 60–64, 2014.

[26] K. Ahmad, W. Pan, and H. Wu, “High performance alumina based graphene nanocomposites with novel electrical and dielectric properties,” *RSC Adv.*, vol. 5,

no. 42, pp. 33607–33614, 2015.

[27] C. Val and N. Humbert, “Alumina with a Thermal Conductivity Close to Beryllia,” *Microelectron. Int.*, vol. 1, no. 2, pp. 45–50, 1983.

[28] J. M. Clemens and Lasance, “The thermal conductivity of aluminum oxide,” vol. 7. pp. 6–7, 1999.

[29] F. a Al-Sanabani, A. a Madfa, and N. H. Al-qudaimi, “Alumina ceramic for dental applications : A review article,” vol. 1, no. 1, pp. 26–34, 2014.

[30] W. Werdeckear and A. F., “I EEE: Trans.,” *I EEE Trans. Cornponent Hybrids Manuf Technol., CHMT*, vol. 7, no. 4, p. 399, 1984.

[31] R. Brown, “Thin film substrates,” in *L.I. Maisseal nd R.Glang (eds.),H andbook of Thin fibn Technology*, McGraw-Hill, 1989.

[32] N. Iwase, K. Anzai, K. Shinozaki, O. Hirao, and Y. Sugiura, “Thick Film and Direct Bond Copper Forming Technologies for Aluminum Nitride Substrate,” *IEEE Trans. Components, Hybrids, Manuf. Technol.*, vol. 8, no. 2, pp. 253–258, 1985.

[33] Matweb.com, “MatWeb, Material property data.” 2015.

[34] T. O. Mason, “Electronic substrate and package ceramic,” *Britannica*, 2015. [Online]. Available: http://global.britannica.com/technology/electronic-substrate-ceramics.

[35] A. I. Y. Tok, F. Y. C. Boey, and K. a. Khor, “Tape casting of high dielectric ceramic composite substrates for microelectronics application,” *J. Mater. Process. Technol.*, vol. 89–90, pp. 508–512, 1999.

[36] H. He, R. Fu, D. Wang, X. Song, and M. Jing, “A new method for preparation of direct bonding copper substrate on Al2O3,” *Mater. Lett.*, vol. 61, no. 19–20, pp. 4131–4133, 2007.

[37] J. Schulz-Harder and K. Exel, “Recent developments of direct bonded copper (DBC) substrates for power modules,” *Fifth Int. Conf. onElectronic Packag. Technol. Proceedings, 2003. ICEPT2003.*, 2003.

[38] J. Schulz-Harder, “DBC substrates as a base for power MCM’s,” *Proc. 3rd Electron. Packag. Technol. Conf. (EPTC 2000) (Cat. No.00EX456)*, pp. 315–320, 2000.

[39] A. Dehmel, J. Schulz-Harder, A. Roth, and I. Baumeister, “Direct copper bonded ceramic substrates for use with power LEDS,” *Proc. Electron. Packag. Technol. Conf. EPTC*, vol. 00, pp. 3–8, 2007.

[40] J. Park, K. C. C. Corporation, A. Roth, and K. C. C. E. Gmbh, “Improved thermal cycling reliability of ZTA DBC substrates by manipulating metallization

properties," pp. 25–27, 2014.

[41] M. Entezarian and R. a L. Drew, "Direct bonding of copper to aluminum nitride," *Mater. Sci. Eng. A*, vol. 212, no. 2, pp. 206–212, 1996.

[42] Y. Yoshino, "Role of Oxygen in Bonding Copper to Alumina," *J. Am. Ceram. Soc.*, vol. 72, pp. 1322–1327, 1989.

[43] J. Lutz, T. Herrmann, M. Feller, R. Bayerer, T. Licht, and A. R., "Power Cycling Induced Failure Mechanisms in the Viewpoint of Rough Temperature Environment," in *6th International Conference on Integration of Power Electronics Systems*, 2008, pp. 224–237.

[44] Y. Wei and J. W. Hutchinson, "Nonlinear Delamination Mechanics for Thin Films," *J. Mech. Phys. Solids*, vol. 45, pp. 1137–1159, 1997.

[45] S. Pietranico, S. Pommier, S. Lefebvre, Z. Khatir, and S. Bontemps, "Microelectronics Reliability Characterisation of power modules ceramic substrates for reliability aspects," *Microelectron. Reliab.*, vol. 49, no. 9–11, pp. 1260–1266, 2009.

[46] S. Pietranico, S. Pommier, S. Lefebvre, and S. Pattofatto, "Thermal fatigue and failure of electronic power device substrates," *Int. J. Fatigue*, vol. 31, no. 11–12, pp. 1911–1920, 2009.

[47] V. Smet, F. Forest, J. Huselstein, F. Richardeau, Z. Khatir, S. Lefebvre, and M. Berkani, "Ageing and failure modes of IGBT modules in high temperature power cycling," *IEEE Trans. Ind. Electron.*, vol. 58, no. 10, pp. 4931–4941, 2011.

[48] P. McCluskey, "Reliability of power electronics under thermal loading," in *7th International Conference on Integrated Power Electronics Systems*, 2012, pp. 1–8.

[49] L. Xu, M. Wang, Y. Zhou, Z. Qian, and S. Liu, "An optimal structural design to improve the reliability of Al2O3–DBC substrates under thermal cycling," *Microelectron. Reliab.*, 2015.

[50] K. Shimada, J. Komotori, and M. Shimizu, "The Applicability of the Manson–Coffin Law and Miner's Law to Extremely Low Cycle Fatigue," *Trans Jpn Soc Mech Eng*, vol. 53, no. 491, pp. 1178–85, 1987.

[51] L. Xue, "A Unified Expression for Low Cycle Fatigue and Extremely Low Cycle Fatigue and Its Implication for Monotonic Loading," *Int. J. Fatigue*, vol. 30, pp. 1691–8, 2008.

[52] S. Torquato and H. Haslach, *Random Heterogeneous Materials: Microstructure and Macroscopic Properties*, vol. 55, no. 4. New York: Springer, 2002.

[53] K. Z. Markov, *Elementary micromechanics of heterogeneous media. In Heterogeneous Media—Micromechanics Modeling Methods and Simulations*. Boston: Birkhäuser.

[54] W. Pabst and E. Gregorová, “Cross-Property Relations between Elastic and Thermal Properties of Porous Ceramics,” *Adv. Sci. Technol.*, vol. 45, pp. 107–112, 2006.

[55] W. Pabst and E. Gregorová, “A cross-property relation between the tensile modulus and the thermal conductivity of porous materials,” *Ceram. Int.*, vol. 33, no. 1, pp. 9–12, 2007.

[56] W. Pabst, E. Gregorová, and G. Tichá, “Effective properties of suspensions, composites and porous materials,” *J. Eur. Ceram. Soc.*, vol. 27, no. 2–3, pp. 479–482, 2007.

[57] E. Gregorová, W. Pabst, Z. Sofer, O. Jankovský, and J. Matějíček, “Porous alumina and zirconia ceramics with tailored thermal conductivity,” *6th Eur. Therm. Sci. Conf. Eurotherm 2012*, vol. 395, no. 1, 2012.

[58] K. Ahmad, P. Wei, and C. Wan, “Thermal conductivities of alumina-based multiwall carbon nanotube ceramic composites,” *J. Mater. Sci.*, vol. 49, no. 17, pp. 6048–6055, 2014.

[59] S. Itoh, Y. Hirata, T. Shimonosono, and S. Sameshima, “Theoretical and experimental analyses of thermal conductivity of the alumina-mullite system,” *J. Eur. Ceram. Soc.*, vol. 35, no. 2, pp. 605–612, 2015.

[60] D. M. Liu and W. H. Tuan, “Microstructure and thermal conduction properties of Al2O3/Ag composites,” *Acta Mater.*, vol. 44, no. 2, pp. 813–818, 1996.

[61] D. M. Liu and C. T. Fu, “Heat conduction of composites and its dependence on the microstructure of Al2O3-Cr3 C2 composite,” *Acta Metall. Mater.*, vol. 43, no. 3, pp. 1001–1006, 1995.

[62] D.-M. Liu, W. H. Tuan, and C.-C. Chiu, “Thermal diffusivity, heat capacity and thermal conductivity in Al2O3/Ni composite,” *Mater. Sci. Eng. B*, vol. 31, no. 3, pp. 287–291, 1995.

[63] P. Bansal, K. N. Lee, and a Miller, “Thermal Conductivity of Ceramic Barrier and Environmental Barrier Coating Materials Thermal,” no. September, 2001.

[64] F. F. Egorov and Y. M. Goryachev, “Thermal conductivity of composite powder materials based on zirconium nitride alumina, and molybdenum,” pp. 354–357.

[65] S. Bakshi, i K. Balan, and A. Agarwal, “Thermal conductivity of plasma-sprayed aluminum oxide—multiwalled carbon nanotube composites,” *J Am Ceram Soc*, vol. 91, pp. 942–947, 2008.

[66] G.-D. Z. andAmiya K. Mukherjee, “Carbon Nanotube Reinforced Alumina-Based Ceramics with Novel Mechanical, Electrical, and Thermal Properties,” *Int. J. Appl. Ceram. Technol.*, vol. 1, no. 2, 2005.

[67] L. Kumari, T. Zhang, G. H. Du, W. Z. Li, Q. W. Wang, a. Datye, and K. H. Wu,

"Thermal properties of CNT-Alumina nanocomposites," *Compos. Sci. Technol.*, vol. 68, no. 9, pp. 2178–2183, 2008.

[68] O. Hanzel, J. Sedláček, E. Hadzimová, and P. Šajgalík, "Thermal properties of alumina-MWCNTs composites," *J. Eur. Ceram. Soc.*, vol. 35, no. 5, pp. 1559–1567, 2015.

[69] D. E. Aldrich and Z. Fan, "Microstructural characterisation of interpenetrating nickel/alumina composites," *Mater. Charact.*, vol. 47, no. 3–4, pp. 167–173, 2001.

[70] L. F. Johnson, D. P. H. Hasselman, and J. F. Rhodes, *Effect of VS-SiC reinforcement on the thermal diffusivity/conductivity of an alumina matrix composite. In Whisker and Fiber-toughened Ceramics*. Metals Park, OH: ASM International, 1988.

[71] P. H. Mc Cluskey, R. K. Willians, R. S. Graves, and T. T.N., "Thermal diffusivity/conductivity of alumina-silicon carbide composites," *J. Am. Ceram. Soc*, vol. 73, no. 2, pp. 461–464, 1990.

[72] L. Fabbri, E. Scafe, and G. Dinelli, "Thermal and elastic properties of alumina-silicon carbide whisker composites," *J. Eur. Ceram. Soc*, vol. 14, no. 5, pp. 441–446, 1994.

[73] N. P. Bansal and D. Zhu, "Thermal conductivity of zirconia-alumina composites," *Ceram. Int.*, vol. 31, no. 7, pp. 911–916, 2005.

[74] W. Zhou, S. Qi, C. Tu, H. Zhao, C. Wang, and J. Kou, "Effect of the particle size of Al2O3 on the properties of filled heat-conductive silicone rubber," *J. Appl. Polym. Sci.*, vol. 104, no. 2, pp. 1312–1318, Apr. 2007.

[75] S. Zhang, "The effects of particle size and content on the thermal conductivity and mechanical properties of Al2O3/high density polyethylene (HDPE) composites," *Express Polym. Lett.*, vol. 5, no. 7, pp. 581–590, 2011.

[76] J. Maxwell, *Electricity and magnetism*. Oxford: Clarendon Press Oxford, 1873.

[77] L. Rayleigh, "Philos," *Mag*, vol. 34, no. 481, 1892.

[78] G. Hadley, "Thermal conductivity of packed metal powders," *Int J Heat Mass Transf.*, vol. 29, no. 6, pp. 909–920, 1986.

[79] M. Cunningham and K. Peddicord, "Heat conduction in spheres packed in an infinite regular cubical array," *Int J Heat Mass Transf.*, vol. 24, no. 7, pp. 1081–1088, 1981.

[80] D. P. H. Hasselman and L. F. Johnson, "No Titl," *J. Compos. Mater*, vol. 21, no. 508, 1987.

[81] M. Wang and N. Pan, "Predictions of effective physical properties of complex multiphase materials," *Mater. Sci. Eng. R Reports*, vol. 63, no. 1, pp. 1–30, 2008.

[82] “NSTIP (The National Science, Technology and Innovation Plan) Project Report.” 2016.

[83] A. S. Composites, M. I. K. Collin, and D. J. Rowcliffe, “Influence of Thermal Conductivity and Fracture Toughness on the Thermal Shock Resistance of,” vol. 40, pp. 1334–1340, 2001.

[84] C. W. Nan, R. Birringer, D. R. Clarke, and H. Gleiter, “Effective thermal conductivity of particulate composites with interfacial thermal resistance,” *J. Appl. Phys.*, vol. 81, no. 10, pp. 6692–6699, 1997.

[85] Y. Benveniste and G. J. Dvorak, “On a Correspondence Between Mechanical and Thermal Effects in Two-Phase Composites,” *Micromechanics and Inhomogeneity*, no. 1986, pp. 65–81, 1990.

[86] I. Doghri and A. Ouaar, “Homogenization of two-phase elasto-plastic composite materials and structures study of tangent operators, cyclic plasticity and numerical algorithms,” *Int. J. Solids Struct.*, vol. 40, no. 7, pp. 1681–1712, 2003.

[87] R. Pal, “On the Electrical Conductivity of Particulate Composites,” *J. Compos. Mater.*, vol. 41, no. 20, pp. 2499–2511, 2007.

[88] C. Van Godbold, V. A. Sankaran, and J. L. Hudgins, “Thermal analysis of high-power modules,” *IEEE Trans. Power Electron.*, vol. 12, no. 1, pp. 3–11, 1997.

[89] Engineeringtoolbox.com, “The Engineering Tool Box; Resources, Tools and Basic Information for Engineering and Design of Technical Applications.” 2016.

[90] L. Xu, Y. Zhou, and S. Liu, “DBC substrate in Si- and SiC-based power electronics modules: Design, fabrication and failure analysis,” *2013 IEEE 63rd Electron. Components Technol. Conf.*, vol. 1, no. 2, pp. 1341–1345, 2013.

[91] JEDEC Solid State Technology Association, “JEDEC Standard JESD22-A104D, Temperature Cycling,” *Jedec.Org*, no. May 2005, p. 11, 2009.

# Vitae

**Name** : LEMBOYE KAREEM TAIWO

**Nationality** : NIGERAIN

**Date of Birth** : 07/11/1987

**Email** : lemboye_karim@yahoo.com

**Address** : 2, Shodimu Street Ikotun, Lagos, Nigeria

**Academic Background** :

M.sc Mechanical Engineering, King Fahd University of Petroleum and Minerals, Saudi Arabia (2016)

B.sc Mechanical Engineering, Olabisi Onabanjo University, Ago-Iwoye (2012)

Senior Secondary School Leaving Certificate, Latmos Comprehensive College, Ikotun, Lagos (2004)

First School Leaving Certificate, Christ Academy Nursery & Pry School, Ikotun, Lagos (1998)

**Publication(s)** :

**K. T. Lemboye**, A. T. Layeni, K. Oduntan, M. A. Akintunde, and O. A. Dahunsi, "Developing a Two Stage Cascade Compressor Arrangement for Ice Block Production" *Journal of Machinery Manufacturing and Automation,* vol. 4, no. 2, pp. 10-16, 2015.